Ultra-high Speed Optical Imaging of Ultrasound-activated Microbubbles in Mesenteric Microvessels

Hong Chen

A dissertation
submitted in partial fulfillment of the
requirements for the degree of

Doctor of Philosophy

University of Washington

2011

Program Authorized to Offer Degree:
Department of Bioengineering

University of Washington
Graduate School

This is to certify that I have examined this copy of a doctoral dissertation by

Hong Chen

and have found it is complete and satisfactory in all respects,
and that any and all revisions required by the final
examining committee have been made.

Co-chair of the Supervisory Committee:

____
Lawrence A. Crum

____
Matt O'Donnell

Reading Committee:

____
Thomas J. Matula

____
Andrew A. Brayman

____
Lawrence A. Crum

Date: ________________________________

In presenting this dissertation in partial fulfillment of the requirements for a doctoral degree at the University of Washington, I agree that the Library shall make its copies freely available for inspection. I further agree that extensive copying of this dissertation is allowable only for scholarly purposes, consistent with "fair use" as prescribed in the U.S. Copyright Law. Requests for copying or reproduction of this dissertation may be referred to ProQuest Information and Learning, 300 North Zeeb Road, Ann Arbo, MI 48106-1346,1-800-521-0600, to whom the author has granted "the right to reproduce and sell (a) copies of the manuscript in microform and/or (b) printed copies of the manuscript made from microform."

Signature________________________________

Date____________________________________

University of Washington

Abstract

Ultra-high Speed Optical Imaging of Ultrasound-activated Microbubbles in Mesenteric Microvessels

Hong Chen

Chair of the Supervisory Committee
Professor Lawrence A. Crum
Department of Bioengineering

Ultrasound contrast agent microbubbles have gained widespread applications in diagnostic and therapeutic ultrasound. Animal studies of bioeffects induced by ultrasound-activated microbubbles have demonstrated that microbubbles can cause microvessel damage. Much scientific attention has been attracted to such microvascular bioeffects, not only because of the related safety concerns, but also because of the potential useful applications of microbubbles in the intravascular delivery of drugs and genetic materials into target tissues. A significant challenge in using microbubbles in medical ultrasound is the lack of knowledge about how the microbubbles behave in blood vessels when exposed to ultrasound and how their interactions with ultrasound cause vascular damage. Although extensive studies were performed in the past to study the

dynamics of microbubbles, most of those studies were performed *in vitro* and did not directly address the clinical environment in which microbubbles are injected into blood vessels.

In this thesis work, a synchronized optical-acoustic system was set up for ultra-high speed imaging of insonated microbubbles in microvessels. The recorded images revealed the formation of microjets penetrating the microbubbles, as well as vessel distention (motion outward against the surrounding tissue) and vessel invagination (motion inward toward the lumen) caused by the expansion and collapse of the microbubbles, respectively. Contrary to current paradigms which propose that microbubbles damage vessels either by distending them or by forming liquid jets impinging on them, microbubbles translation and jetting were in the direction away from the nearest vessel wall; furthermore, invagination typically exceeded distention in arterioles and venules. Vessel invagination was found to be associated with vascular damage. These studies suggest that vessel invagination may be a newly discovered potential mechanism for vascular damage by ultrasound-activated microbubbles. The dynamics of bubble-vessel interactions are coupled intimately with the viscoelastic properties of the microvessels. To probe these properties, a method based on the relaxation times of the invaginated microvessels was used to estimate the relaxation time constants of the microvessels. It was found that the time constants were on microsecond time scales, which provided insight into the unique and unknown viscoelastic properties of the microvessels.

TABLE OF CONTENTS

Page

List of Figures iv

List of Tables vi

Chapter 1 Introduction 1

- 1.1 Motivation 1
- 1.2 Background 3
  - 1.2.1 Ultrasound Contrast Agent Microbubbles 3
  - 1.2.2 Microvessel Structure and Function 6
  - 1.2.3 Microbubble Induced Microvascular Bioeffects 8
  - 1.2.4 Ultra-high Speed Photomicrography 11
- 1.3 Scope of This Thesis 12

Chapter 2 Ultra-high Speed Photomicrography of Microbubble Interaction with Microvessels: Methods and Limitations 15

- 2.1 Introduction 15
- 2.2 Animal Tissue Preparation Methods 17
- 2.3 Ultra-high Speed Photomicrography 21
  - 2.3.1 Optical System 22
  - 2.3.2 Acoustic System 23
  - 2.3.3 Ultra-high Speed Imaging Procedure 26
  - 2.3.4 Image Analysis Methods 27
- 2.4 Limitations 30
  - 2.4.1 Limitations of the Animal Model 30
  - 2.4.2 Limitations of the Imaging Technique 34
- 2.5 Summary 35

Chapter 3 Observations of Translation and Jetting of Ultrasound-activated Microbubbles in Microvessels 36

- 3.1 Introduction 36

3.2 Methods 39
3.2.1 Animal Tissue Preparation 39
3.2.2 Ultra-high Speed Imaging 39
3.2.3 Image Analysis 39
3.3 Results 40
3.3.1 Microbubble Translation 40
3.3.2 Microjetting 48
3.4 Discussion 50
3.5 Summary 54

Chapter 4 Blood Vessel Deformation on Microsecond Time Scales by Ultrasound Cavitation 55
4.1 Introduction 55
4.2 Methods 56
4.2.1 Animal Tissue Preparation 56
4.2.2 Ultra-high Speed Imaging 56
4.2.3 Image Analysis 56
4.3 Results 57
4.4 Discussion 63
4.5 Summary 64

Chapter 5 Correlation of Microbubble Cavitation Induced Microvessel Deformation and Vascular Bioeffects 65
5.1 Introduction 65
5.2 Methods 68
5.2.1 Animal Tissue Preparation 68
5.2.2 Ultra-high Speed Imaging 68
5.2.3 Image Analysis 70
5.2.4 Vascular Bioeffects Assessment 70
5.3 Results 74
5.3.1 Relatively Large Microvessels 74

5.3.2 Relatively Small Microvessels 84
5.4 Discussion 88
5.4.1 Damage of Large Microvessels 88
5.4.2 Damage of Small Microvessels 89
5.5 Summary 91

Chapter 6 Relaxation of Microvessels Deformed by Microbubbles................................ 93
6.1 Introduction 93
6.2 Methods...95
6.2.1 Animal Tissue Preparation 95
6.2.2 Ultra-high Speed Imaging 96
6.2.3 Image Analysis 97
6.2.4 Estimation of the Relaxation Time Constants 98
6.3 Results 99
6.4 Discussion 107
6.4.1 Scales of the Relaxation Time Constants 107
6.4.2 Implications of the Findings 109
6.4.3 Limitations of This Work 110
6.5 Summary 112

Chapter 7 Principle Conclusions and Future Directions.. 113
7.1 Principle Conclusions...113
7.2 Future Directions..117
7.2.1 Optimization of the Ultra-high Speed Imaging System 117
7.2.2 Estimation of Vessel Wall and Surrounding Tissue Displacements .. 120
7.2.3 Ultra-high Speed Imaging of Targeted Microbubbles....................... 122
7.2.4 Ultra-high Speed Imaging of Microbubbles in a Shockwave Field ... 124
7.2.5 Ultra-high Speed Imaging of Microbubbles *in vivo* 127
7.2.6 Modeling of Microbubble Interaction with Microvessels 129

Bibliography 131

LIST OF FIGURES

Figure Number Page

1.1 Microscopic image and schematic illustration of microbubbles....................... 4
1.2 Example of a microbubble oscillation in an ultrasound field 5
1.3 Microvessel structure.. 8
1.4 Proposed mechanisms for vascular damage by microbubbles........................ 10
2.1 Comparison of rat mesentery (left) and cecum (right) tissues. 18
2.2 Illustration of the prepared tissue sample 20
2.3 Microscopic view of microvessels in the rat mesentery 20
2.4 Picture of the experimental system with the main components marked out... 21
2.5 Schematic illustration of the experimental setup. 21
2.6 Representative pressure waveforms 25
2.7 Illustration of the system timing.. 27
2.8 Illustration of several measured quantities 29
2.9 Model for a spherical microbubble in a vessel 30
2.10 The effectiveness of the mesentery tissue in viscous dissipation 33
3.1 High-speed image sequences of microbubble translation in microvessels..... 42
3.2 Displacements of the microbubble center and vessel wall 43
3.3 Maximum microbubble translation distance with respect to 46
3.4 Microbubble translation in a relatively small microvessel.. 47
3.5 Microjets formed in microvessels... 50
3.6 Vascular rupture involving a liquid jet. 54
4.1 Characteristics of observed bubble-vessel interactions 58
4.2 Image sequences to illustrate types of vessel invagination............................ 59
4.3 Measurements of radial displacements of the vessel wall 60
4.4 Dynamic responses of an arteriole to a microbubble..................................... 61
4.5 Comparison of maximum vessel invagination and distention.. 62
5.1 Illustration of system timing. 69
5.2 Illustration of the image registration method.. 72

5.3 Microbubble interaction with a large microvessel. 76
5.4 Histology results associated with the recorded image sequence 77
5.5 Image sequence demonstrating invagination-dominated response................. 79
5.6 TEM results associated with the image sequence shown in Figure 5.5.......... 80
5.7 Vascular bioeffects found in an arteriole of 70 µm in diameter 83
5.8 Image sequence of a microbubble interaction with a capillary....................... 86
5.9 Rupture of a small microvessel by a cluster of microbubbles, ... 87
6.1 Illustration of the system timing. 97
6.2 Schematic representation of a Voigt model. 98
6.3 Invagination and recovery of the microvessels.. 100
6.4 Vessel wall displacements as a function of time. 101
6.5 Summary of the measured correlation coefficient and time constants 103
6.6 Relaxation time constants estimated for microvessels................................. 103
6.7 Effect of syringe pump speed on vessel diameter and time constants.......... 106
7.1 Comparison of pressure waveforms with transducer at different locations.. 118
7.2 Tissue displacement estimation 121
7.3 Dynamics of adherent microbubbles in microvessels................................. 124
7.4 Comparison of an ultrasound pulse and a shockwave pulse......................... 126
7.5 Cavitation bubble dynamics under the insonation of a shockwav pulse 126
7.6 Mesentery artery cannulation for the injection of microbubbles................. 128
7.7 Image of a microbubble in a microvessel *in vivo*. 129
7.8 Simulated results of a gas bubble positioned between two plates. 130

LIST OF TABLES

Table Number Page

2.1 Ultra-high speed camera specifications 23
2.2 Specifications of the ultrasound transducer 24
7.1 Parameters of microscope objectives... 120

ACKNOWLEDGEMENTS

I would like to thank my supervisory committee: Drs. Lawrence Crum, Thomas Matula, Andrew Brayman, Michael Bailey, Matthew O'Donnell and Alberto Aliseda. Especially, I would like to thank Dr. Lawrence Crum for his father-like mentorship. I would also like to thank Drs. Thomas Matula and Andrew Brayman, who are great mentors and wonderful people to work with. I am also grateful to Dr. Michael Bailey for his support. Moreover, I would like to thank Drs. Wayne Kreider and Yak-Nam Wang for generously giving their time and advices as I learn to do research. I also want to appreciate Frank Starr for his assistant with the animal studies; Brian MacConaghy and Fran Olson for their assistant with the design and machining of mechanical parts used in my experiment; Drs. John Kucewicz and Barbrina Dunmire for their assistant in image processing; Drs. Joo Ha Hwang, Oleg Sapozhnikov, Vera Khokhlova and Francesco Curra for their insightful discussions. Further thank goes to Dr. Andrew Evan in Indiana University School of Medicine for assistant in preparing and interpreting the histology and TEM results. Last but not least, I want to thank all of the fantastic people in the Center for Industrial and Medical Ultrasound (CIMU) that I have been fortunate enough to work with over the years.

DEDICATION

To my daughter who was born at the time I was preparing this thesis.
To my husband who has always been there to support me to pursue my dreams.
To my parents who love me more than themselves and have sacrificed so much for me.

Chapter 1

Introduction

1.1 Motivation

Typical ultrasound contrast agents (UCAs) are micron-sized gas bubbles stabilized by various coatings (Dindyal & Kyriakides, 2011; Goldberg *et al.*, 1994; Ophir & Parker, 1989). They have gained widespread applications in clinical diagnostic ultrasound to enhance contrast of cardiographic or radiologic features (Cosgrove & Harvey, 2009; Kaul, 2008; Villanueva & Wagner, 2008). Many new applications of UCAs are now under investigation, among which molecular imaging and drug/gene delivery using microbubbles have shown great potential (Dayton & Rychak, 2007; Gessner & Dayton, 2010; Klibanov, 2007; Pichon *et al.*, 2008). The medical significance and potential benefits from the use of microbubbles are clear. However, in 2007 the US Food and Drug Administration (FDA) issued a 'black box' warning for UCAs based on reports of deaths and serious cardiopulmonary reactions in the clinical cardiac examination (Main *et al.*, 2009) (A black box warning is the highest level warning required by the FDA to indicate that the agent may cause serious adverse effects). This warning was revised after a review of efficacy data in 2008, but safety concerns of UCAs still exist (Aggeli *et al.*, 2009; Main *et al.*, 2009; ter Haar, 2009; Van Camp *et al.*, 2007).

In animal studies examining the potential bioeffects of ultrasound-activated microbubbles, the most common finding was microvessel damage (Ay *et al.*, 2001; Miller

& Quddus, 2000; Van Camp *et al.*, 2007). Microvessel damage, such as capillary ruptures, erythrocyte extravasation, and endothelial cell damage, has been observed in many animal tissues; *e.g.*, brain, ear, liver, heart, kidney, intestine and mesentery (Miller *et al.*, 2008). Although the potential harmful bioeffects are uncertain in clinical settings, the potential risks of these damaging effects need to be taken into consideration. Conversely, these bioeffects to microvessels have been explored to enhance vascular permeability to facilitate drug/gene delivery through the vessel wall for gene therapy and localized cancer drug delivery (Dindyal & Kyriakides, 2011; Evan *et al.*, 2001; Ferrara, 2008). To use microbubbles safely and effectively, it is essential to understand the mechanisms by which microbubbles induce microvascular damage.

Acoustical measurements have already provided useful information about microbubble behavior in blood vessels (Hwang *et al.*, 2006; King *et al.*, 2010; Rota *et al.*, 2006; Sassaroli & Hynynen, 2006; Tu *et al.*, 2006); however, direct evidence can be acquired only by optical techniques. To capture the transient dynamics of microbubbles during ultrasound exposure, ultra-high speed photomicrography techniques are required. In previous studies, these techniques were used mainly for *in vitro* experiments in which synthetic materials, such as transparent tubes or gels, were used to mimic blood vessels (Caskey *et al.*, 2006; Caskey, Qin, & Ferrara, 2009; Chomas *et al.*, 2000; de Jong *et al.*, 2000; Postema *et al.*, 2004; Zhong *et al.*, 2001). However, the tubes and gels used in these studies did not have the same mechanical properties as those of the blood vessels.

When this thesis work was first undertaken, there was only one published work on the observations of the transient microbubble dynamics in actual vessels (Caskey *et al.*, 2007). In that pioneering work, streak imaging and strobe imaging were used, which could not fully capture the transient dynamics of microbubbles and vessels due to the limitations of these two imaging techniques. Streak imaging, which continuously records an event over time through a slit, is a one dimensional imaging technique. The strobe imaging method records microbubble dynamics by composing images obtained repetitively using a time-delayed, single-shot method. It is not a real-time imaging method, and is restricted to repeatable events. Therefore, techniques needed to be developed to fully capture the microbubble dynamics in actual microvessels for a better understanding of how microbubbles damage microvessels.

1.2 Background

1.2.1 Ultrasound Contrast Agent Microbubbles

The typical UCA is composed of a suspension of microbubbles which are coated with a phospholipid, albumin or polymer shell (Figure 1.1). It was reported in 1968 that a transient cloud of echoes in the aortic root was noticed during echocardiography each time saline was injected in the supravalvular position (Gramiak & Shah, 1968). Later, it was found that the active agent was free air bubbles entrained in the saline solution during the injection process (Cosgrove & Harvey, 2009). More than 20 years later, Albunex®, the first generation ultrasound contrast agent with an air core coated by albumin, was approved by the US FDA for clinical use (Crouse *et al.*, 1993; Feinstein *et al.*, 1990).

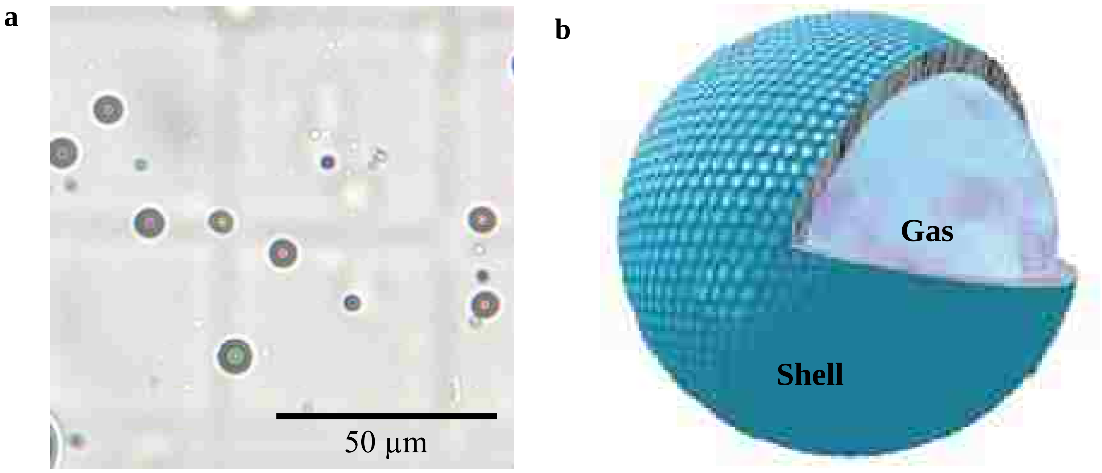

Figure 1.1 (a) Optical microscopic image of microbubbles. (b) Schematic illustration of a microbubble consisting of a gas core coated by a shell.

Compared with free air bubbles, the coating helped to control the size distribution and increased stability. The second-generation agents, which are in use now, have greatly improved stability, achieved by changing the air core to a perfluoropropane gas core with relatively low diffusion coefficient and low solubility in blood (Miller & Nanda, 2004). Two agents are available in the United States: Optison®, which has a protein shell and a size distribution with most diameters in the range of 3.0–4.5 µm, and Definity® which has a lipid shell and a size distribution with most diameters in the range of 1.1–3.3 µm. The small sizes of the microbubbles are required to allow them to pass through the pulmonary capillary beds and thus enable enhanced diagnostic ultrasound visualization of the left heart.

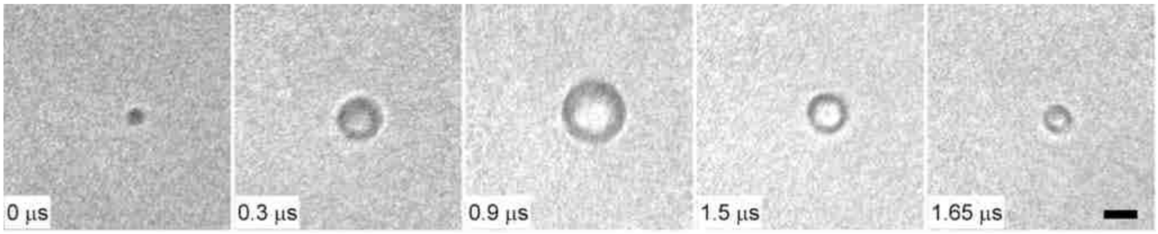

Figure 1.2 Example of a microbubble oscillation in an ultrasound field. A 1 MHz ultrasound pulse was used to drive the microbubble to oscillate. The time stamps are shown on the left corner of all frames. The time when the ultrasound pulse just arrived at the microbubble was set to zero. The scale bar represents 10 µm.

In clinical applications, microbubbles are injected into the circulation to enhance the echogenicity of blood in diagnostic ultrasound imaging. They reflect ultrasound efficiently due to the large acoustic impedance mismatch between the gas inside the microbubble and the blood. Moreover, they undergo volumetric oscillation when exposed to ultrasound, as illustrated by Figure 1.2. The oscillation can generate non-linear backscattered acoustic signals which can be used to further enhance the contrast between the microbubbles and the surrounding tissue (Calliada *et al.*, 1998; Stride & Coussios, 2010). Based on these special characteristics of microbubbles, imaging methods specific for microbubble detection have been developed, such as harmonic power Doppler imaging, pulse-inversion or phase inversion imaging, and amplitude or power modulation imaging (Qin *et al.*, 2009).

In the United States, microbubbles are approved to be used in patients with suboptimal echocardiograms to opacify the left ventricular chamber and to improve the delineation of the left ventricular endocardial border. Contrast-enhanced echocardiography can provide a clear delineation of the endocardial wall and improve evaluation of the blood perfusion in the heart, which leads to substantial improvements in diagnostic accuracy (Platts & Fraser, 2011; Schutt *et al.*, 2003; Soliman *et al.*, 2010). In many other countries, their clinical applications have been expanded to other fields, such as quantification of myocardial blood flow, assessment of renal perfusion, monitoring tumor vascularity and detection of focal liver lesions (Cosgrove & Harvey, 2009; Piscaglia *et al.*, 2010; Pysz *et al.*, 2011; Schneider *et al.*, 2011).

Recently, microbubbles have been demonstrated to have great potential in ultrasound-assisted drug and gene delivery (Carson *et al.*, 2011; Kaul, 2004; Klibanov, 2007) and in molecular imaging, using targeted microbubbles (Gessner & Dayton, 2010; Hernot & Klibanov, 2008; Voigt, 2009). For drug and gene delivery therapies, microbubbles can be loaded with pharmaceutical agents such as chemotherapeutic drugs or large genetic materials, monitored during perfusion using diagnostic ultrasound, and then forced to release the carried materials at the targeted location by higher power ultrasound. In molecular imaging, microbubbles are conjugated with site-specific targeting ligands that allow binding of the microbubbles to disease markers expressed on the endothelium of blood vessels. They have been explored for screening, diagnosing, and monitoring diseases at the molecular level.

1.2.2 Microvessel Structure and Function

Microvessels can be defined as vessels with inner diameters, d, smaller than 250 μm (Lee, 2000). They can be divided into three groups: arterioles (250 μm > d $\geq$ 8 μm), capillaries (d < 8 μm) and venules (250 μm > d ≥ 8 μm) (Lee, 2000). The microcirculation, which involves each of these types of microvessel, is where the exchange of gases, fluids, nutrients and metabolic waste products happens, although most exchange occurs at the capillary level. Figure 1.3a displays the microvascular network in a rat mesentery and Figure 1.3b is a schematic representation of the mesentery bed to show the structure and relation of arterioles, capillaries and venules.

Arterioles have only one or two layers of smooth muscle cells in the tunica media, and metarterioles have discontinuous layer of smooth muscles. Arterioles and muscular sphincters at the arteriolar-capillary junctions control the diameters of the vessel and thus regulate flow into the capillary bed. Capillaries are the smallest diameter vessels. Capillary walls consist of two principal layers: endothelium and basement membrane. Some walls consist exclusively of a single layer of endothelium. The thin walls of capillaries allow the diffusion of oxygen and nutrients out of the capillaries, while allowing carbon dioxide and wastes into the capillaries. Venules are thin-walled vessels which drain the capillary beds. There are three classes of venules: (1) post capillary venules, which are capillary-like venules; (2) collecting venules, which are surrounded by a complete layer of pericytes, and (3) muscular venules, where pericytes are replaced by one or two layers of smooth muscle cells.

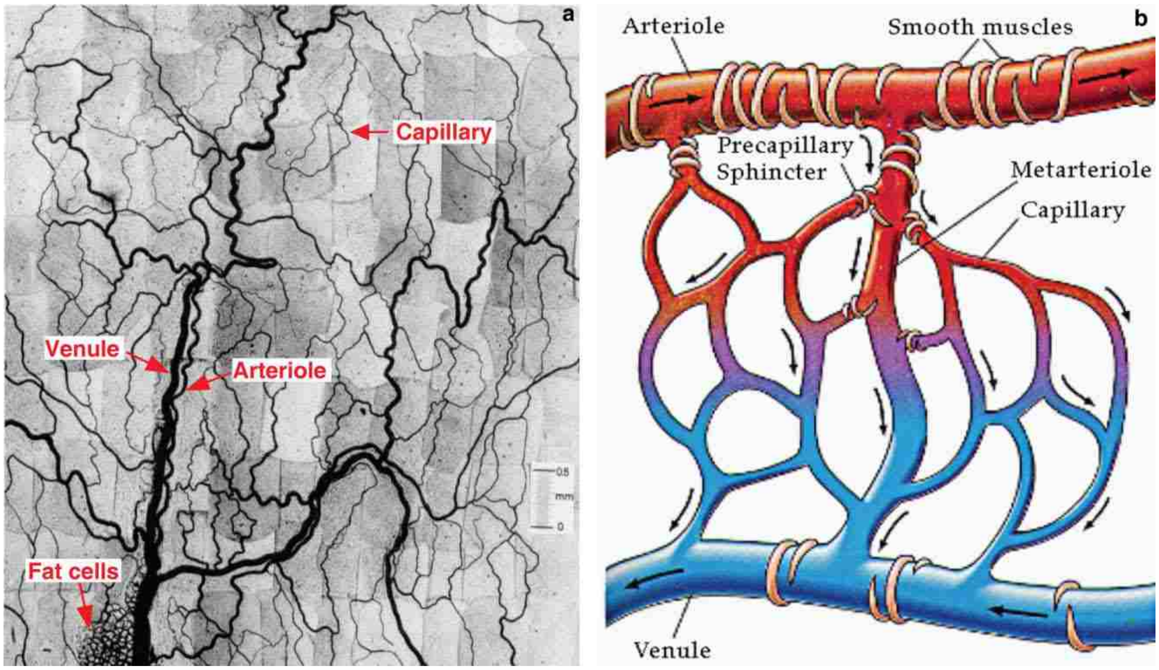

Figure 1.3 Microvessel structure. (a) A micrograph of rat mesentery microvascular network with examples of venules, capillaries and arterioles pointed out (adapted from Pries *et al.* (Pries *et al.*, 1986)). (b) A schematic representation of the mesentery bed.

1.2.3 Microbubble Induced Microvascular Bioeffects

The oscillation of microbubbles in an ultrasound field is a form of acoustic cavitation, which contributes to their applications in both ultrasound diagnoses and therapies. Thus when exposed to acoustic fields, the administration of microbubbles into the circulation introduces cavitation nuclei to the body, which induces a potential for bioeffects. In a review by Miller *et al.* (Miller *et al.*, 2008), it was concluded that microbubble destruction can induce bioeffects, such as microvascular leakage, petechiae, and inflammatory cell infiltration, in small animals at diagnostic ultrasound levels. The first direct *in vivo* observation of microbubble destruction inducing microvessel rupture at diagnostic pressure levels was reported by Skyba *et al.* (Skyba *et al.*, 1998). In that study, rupture of microvessels occurred immediately at the location of microbubble destruction with extravasation of red blood cells into the interstitial space as a consequence. Vascular damage at pressure levels higher than used in diagnostic ultrasound was also reported. Vessel wall damage, hemorrhage and necrosis have been reported in rabbit brains when microbubbles were injected into the brain and insonated by focused ultrasound of frequency 1.5 MHz and peak negative pressures larger than 6.3 MPa (Hynynen *et al.*, 2003). Hemorrhage and petechiae were also found in mouse intestine following injection of microbubbles and exposure to shock waves with peak negative pressure 5.2 MPa (Miller & Gies, 1999).

Studies of bubble-induced damage to nearby materials (*e.g.* ship propellers) date back almost a century (Rayleigh, 1917). For a bubble collapsing near a rigid boundary, a liquid jet can form that penetrates through the bubble and is directed toward the boundary. Such jets have long been considered a potential source of damage to nearby surfaces (Benjamin & Ellis, 1966). A picture of the liquid jet photographed by Dr. Lawrence A. Crum is shown in Figure 1.4a. Although bubbles have been observed to form jets directed away from viscoelastic surfaces under certain conditions (Brujan *et al.*, 2001b), a study using cells mounted on a rigid substrate suggested that cell membranes may be disrupted by the impingement of liquid jets directed at cells (Prentice *et al.*, 2005). It has been suggested recently that liquid jet impact is also one mechanism by which microbubbles damage vessels (Kodama & Tomita, 2000). Another mechanism proposed by Zhong *et al.*

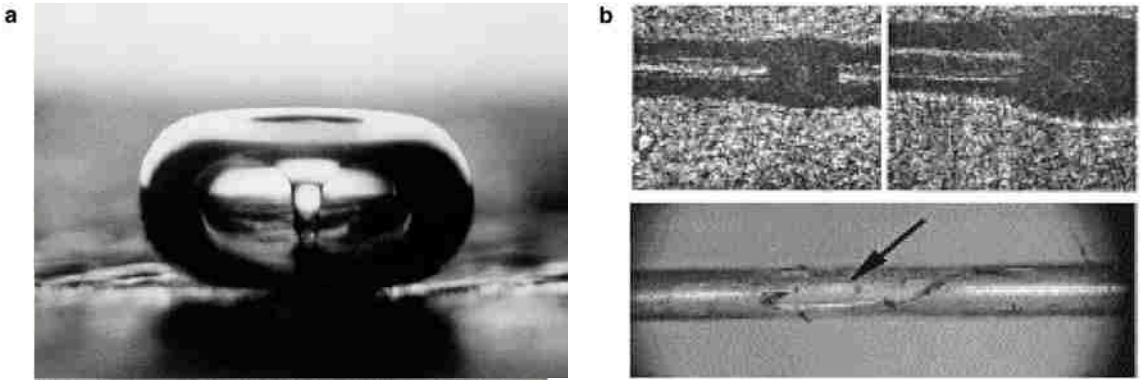

Figure 1.4 Proposed mechanisms for vascular damage by ultrasound-activated microbubbles. (a) A liquid jet penetrates through a bubble during its collapse, and impacts the adjacent solid boundary at the bottom (Crum, 1982). (b) The upper two sequential image frames show a microbubble expanding in a tube at two time points. Dilation of the tube increases when the bubble expands larger. The tube dilation leads to its rupture as shown in the lower panel with the rupture site pointed out by an arrow (Zhong, *et al.*, 2001b).

(Zhong *et al.*, 2001) is that vessel dilation by the large expansion of the microbubbles can rupture vessels, which is based on their observation of microbubble dynamics in a 200-µm hollow fiber in shock wave lithotripsy (Figure 1.4b). However, the exact mechanisms remain unknown, as few studies have addressed the issue of how ultrasound-activated microbubbles interact with actual blood vessels. Note that there are other proposed mechanisms for microbubble induced vascular bioeffects, such as the shear stress induced by the oscillating microbubbles on the nearby vessel wall (Miller *et al.*, 2008). Here we focus on mechanisms that rely on the direct interactions of the microbubbles and the vessels.

1.2.4 Ultra-high Speed Photomicrography

The most direct way to study microbubble dynamics is to visualize them, which requires techniques of high temporal and spatial resolution. To resolve the dynamics of microbubbles activated by megahertz ultrasound, frame rates of at least several millions of frames per second are required for the imaging techniques. Moreover, to see the micron size bubbles clearly, a microscope is needed. One technique that meets all these requirements is ultra-high speed photomicrography.

High-speed photography is defined as "photography involving the recording of events that occur too fast to be perceived by the human eye or recorded by conventional photographic techniques" (Krehl *et al.*, 1999). Ultra-high speed photography is a relative term and its definition evolves as the technology improves. It is considered that high speed photography means imaging with exposure times in the microsecond range and ultra-high speed photography means imaging with nanosecond exposure times. High-speed photomicrography is a special technique devoted to the visualization and registration of fast moving objects on a microscopic scale (Krehl *et al.*, 1999).

Several ultra-high speed photomicrography techniques have been applied in the studies of microbubble dynamics. First, ultra-high speed shutter-controlled cameras have been used to achieve real-time ultra-high speed imaging. One type of the camera, such as Imacon 200 (DRS Hadland, Cupertino, CA, USA), uses a beam splitter to divide an image over several recording devices achieving a maximum recording speed of 200 million frames per second. The maximum total number of frames available is currently 16.

Another type of camera, the Brandaris-128 camera developed by a group at the Netherlands (Chin *et al.*, 2003), uses a rotating mirror sweeping the image over numerous recording devices reaching a maximum frame rate of 25 million frames per second and a total frame number of 128. Second, stroboscopy using very short duration (nanosecond duration time) laser pulses for illumination has also been used (Caskey *et al.*, 2007). This laser-based method records microbubble dynamics by composing images obtained repetitively using a time-delayed, single-shot method. A sequence of snapshot pictures is composed together to show the temporal evolution of an event. This technique is not a real-time imaging method and it is restricted to repeatable events. Third, streak photography has also been used. It is an imaging technique that continuously records an event over time through a slit (Chomas *et al.*, 2000). This technique can achieve higher temporal resolution than the previous two techniques, but it is a one dimensional imaging technique. Comparing the above three techniques, the ultra-high speed camera that can continuously record a sufficient number of two dimensional frames from one event is the "crown of all recording methods" for microbubble dynamics studies (Chomas *et al.*, 2000).

1.3 Scope of This Thesis

The objective of this work was to understand how microbubbles behave in microvessels upon insonation and how their interactions cause vascular bioeffects. The main hypothesis was that the interactions of microbubbles with nearby microvessels can damage the microvessels. The key approach was to use ultra-high speed photomicrography to acquire direct evidence of microbubbles interacting with microvessels in *ex vivo* animal tissue.

In Chapter 2, an experimental system and animal model preparation methods will be described. Briefly, the experimental system was a synchronized optical-acoustic system used for the ultra-high speed imaging of the microbubbles. Techniques for preparing the *ex vivo* animal tissue for clearly visualizing the injected microbubbles in microvessels were developed. In addition, the limitations of the experimental methods were analyzed. The methods described in Chapter 2 were used in all of the subsequent studies discussed in Chapters 3–6.

In Chapter 3, the dynamics of ultrasound-activated microbubbles in the microvessels are presented, focusing on the translation and jetting behavior of the microbubbles. Contrary to a priori hypothesis that collapsing microbubbles would jet toward the tissue, it was observed that microbubbles translated and jetted *away* from the nearest vessel wall. These observations appear to be characteristic of a strong coupling between ultrasound-driven microbubbles and compliant microvessels.

In Chapter 4, the dynamics of the microvessels excited by the nearby ultrasound-activated microbubbles are discussed. Microbubble expansion and collapse caused vessel distention (movement of the vessel wall toward the surrounding tissue) and invagination (movement of the vessel wall toward the lumen), respectively. Moreover, in most cases involving either venules or arterioles, the extent of vessel invagination was generally greater than the corresponding extent of vessel distention.

In Chapter 5, association of vessel deformation and vascular damage is discussed. Vessel deformation was recorded by ultra-high speed photomicrography, and the directly associated vascular damage was demonstrated by either histology or TEM analyses, or by the extravasation of microbubbles. Potential mechanisms for vascular damage by the microbubbles are proposed based on these studies.

In Chapter 6, a new microbubble-based method to assess the viscoelastic properties of the microvessels is described. The relaxation time courses of the deformed microvessels induced by the ultrasound-activated microbubbles were recorded. The relaxation time constant, an indicative of the time-dependent viscoelastic properties of the tissues, was derived based on a Voigt model.

In Chapter 7, this thesis work is summarized and future directions are discussed.

Chapter 2

Ultra-high Speed Photomicrography of Microbubble Interaction with Microvessels: Methods and Limitations

2.1 Introduction

Ultra-high speed photomicrography has been used in investigating microbubble transient dynamics for more than a decade (Bouakaz *et al.*, 2005; Caskey *et al.*, 2006; Caskey, Qin, Dayton, *et al.*, 2009; Chomas *et al.*, 2000; de Jong *et al.*, 2000; Garbin *et al.*, 2007; Kuribayashi & Natori, 1999; Marmottant *et al.*, 2006; Postema *et al.*, 2004; Zheng *et al.*, 2007). In most of these studies, small tubes (*e.g.* cellulose or acrylic tubes) with diameters much larger than those of the microbubbles were used as vessel phantoms to simulate microbubbles in an unbounded environment, such as in the blood pool or large blood vessels. At the same time, modeling efforts were underway which focused on simulating microbubble oscillation in an infinite fluid using various modified Rayleigh-Plesset equations (Allen *et al.*, 2002; Church, 1995; de Jong *et al.*, 1994; Doinikov & Bouakaz, 2011; Leighton, 1994; Marmottant *et al.*, 2005; Morgan *et al.*, 2000; Qin *et al.*, 2009).

Recently, the great potential of microbubbles in new applications, such as drug/gene delivery and molecular imaging, has attracted growing interest in investigating the boundary effects to microbubble dynamics, as microbubbles must be in proximity to the vascular endothelium to be effective in these applications. To bring microbubbles close to the boundary, different techniques have been used, such as adhering microbubbles to the tube walls using targeted microbubbles (Zhao *et al.*, 2005), manipulating microbubbles to be close to rigid plates using optical tweezers (Garbin *et al.*, 2007; Prentice *et al.*, 2005), or using small tubes with diameters comparable to microbubble sizes (Caskey *et al.*, 2006; Zheng *et al.*, 2007). These *in vitro* studies found that the close proximity of the microbubbles to the boundary resulted in: (1) asymmetric microbubble oscillation with reduced amplitudes, (2) shifted resonance frequencies, and (3) the formation of microjets. At the same time, the focus of microbubble modeling steered from modeling microbubbles in the free field to the constrained condition of the intravascular environment. In these models, the vessels were simplified to be a rigid or a compliant tube or two parallel plates (Gao *et al.*, 2009; Hu *et al.*, 2005; Miao *et al.*, 2008; Ory *et al.*, 2000; Qin *et al.*, 2006; Ye & Bull, 2006; Yuan *et al.*, 1999). These models, focusing on the oscillatory behavior of the microbubbles, predicted that the characteristics of microbubble oscillation within a small vessel will depend on the vessel and microbubble diameters and on the mechanical properties of the vessel with connective tissue (Qin *et al.*, 2009). The major limitation of the previous experimental and modeling work is that the vessel phantoms and simplified models cannot match the viscoelastic properties of actual blood vessels. Observations of microbubble dynamics in actual vessels connected with surrounding tissue have been reported only once (Caskey *et al.*, 2007). In that pioneering work, streak and strobe imaging were used, which did not fully capture the transient dynamics of microbubbles and microvessels.

In this chapter, a synchronized optical-acoustic system for ultra-high speed imaging of microbubble dynamics in actual microvessels was set up, and techniques for administration of microbubbles into the microvessels of *ex vivo* animal tissue were developed. They were used in this thesis work to study microbubble and microvessel dynamics under the exposure of single ultrasound pulses.

2.2 Animal Tissue Preparation Methods

The protocol used for animal experiments was approved by the Institutional Animal Care and Use Committee at the University of Washington. The rat mesentery was selected as the tissue model. It is composed of a membranous tissue, which contains thin and transparent regions, allowing easy observations of its microvasculature under light microscopy. In a previous study of direct observations of microbubbles in microvessels performed by Caskey *et al.*, rat cecum was used as the tissue model (Caskey *et al.*, 2007). A comparison of rat mesentery and cecum tissues is shown in Figure 2.1. The mesentery tissue has better optical transparency than the cecum, although the cecum has richer vascular network than mesentery.

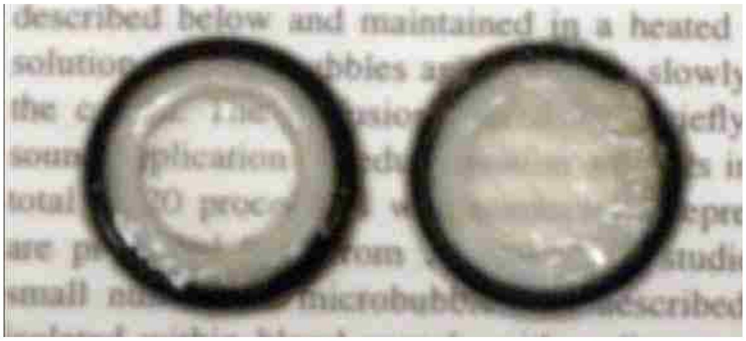

Figure 2.1 Comparison of rat mesentery (left) and cecum (right) tissues. Tissue samples were captured by holders with O-rings and put on a piece of paper. Mesentery tissue has better optical transparency that the cecum.

Fischer 344 rats (~200 g body weight, male) were used. To prepare each tissue sample, a rat first was anesthetized with ketamine and xylazine. Then, the mesentery and intestine were exteriorized through an abdominal midline incision. The exposed tissue was covered with gauze pads moistened with saline solution at 37°C in order to prevent tissue dehydration. The superior mesenteric artery (SMA) was then cannulated using a 24-gauge angiocatheter. Cannulation was followed immediately by injection of heparinized saline through the catheter to flush out the blood from the mesentery vessels. Next, the portal vein was cannulated by a 20-gauge angiocatheter to serve as an outflow orifice. Its mesentery with intestine was excised after visible blood was no longer present in the outflow.

A segment of the mesentery with a rich vascular network, as determined by light microscopic examination, was selected as the region of interest (ROI). While perfusion was maintained through the SMA cannula, one feeding artery and one draining vein of the

ROI were cannulated using two polyethylene tubes with 0.6 mm outer diameter (PE 10; VWR International, San Francisco, CA, USA), and the appropriate vessel branches leading to other regions were ligated by suture. Commercial ultrasound contrast agent microbubbles (Definity®) diluted in saline to a concentration between 0.03 to 0.1% by volume were perfused into the ROI through one of the tubes using a syringe pump. The ROI was held in place by first gently spreading and then sandwiching it firmly at the edges by two plates with a 3.5 cm radius semicircular hole, as illustrated by Figure 2.2. The two D-shaped plates effectively clamped the margin of the tissue to restrain the injected microbubbles within the ROI. Care was taken not to stretch the tissue more than appeared to be the case *in situ* while applying the clamping devices. Green India ink (Dr. Ph. Martin's Bombay India Inks; Blick Art Materials, Galesburg, IL, USA) diluted by saline to a volume concentration less than 3% was mixed with the microbubbles before injection. The ink was used to increase the visual contrast of the vessels relative to the surrounding tissue, and also to indicate blood vessel leakage. An image of the microvascular in the rat mesentery was shown in Figure 2.3.

Tissue preparation was completed within one hour and data were collected within the following three hours. Tissue viability was assessed in limited experiments using propidium iodide, a fluorescent indicator of cell death. A progressive decrease in cell viability with time was observed. However, the correlation between cell viability and tissue’s mechanical properties is unknown. We presume that minimal changes in the mechanical properties occurred during the short time after animal sacrifice.

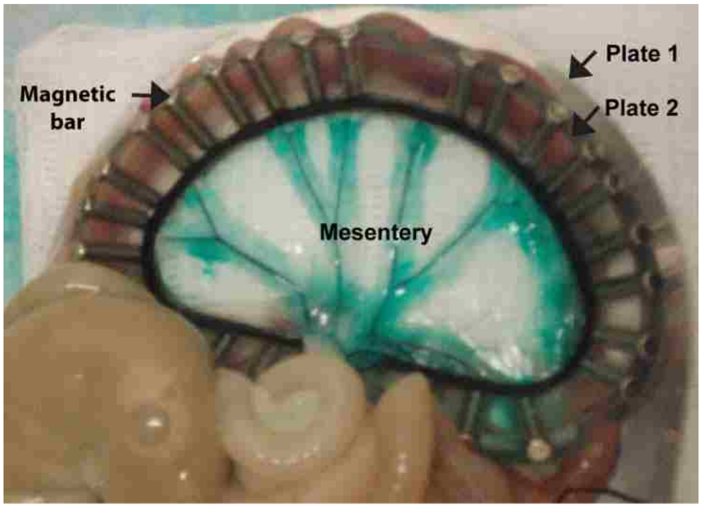

Figure 2.2 Illustration of the prepared tissue sample. The rat mesentery is composed of a membranous tissue divided into several 'mesenteric windows' by fatty frames containing large branches of mesenteric arteries and veins, shown with green dye. These windows are transparent, allowing for direct observation of their microvasculature by light microscopy. A selected mesenteric region is sandwiched between two D-shaped plates (plates 1 and 2) to provide support. The two plates were hold together by magnetic bars.

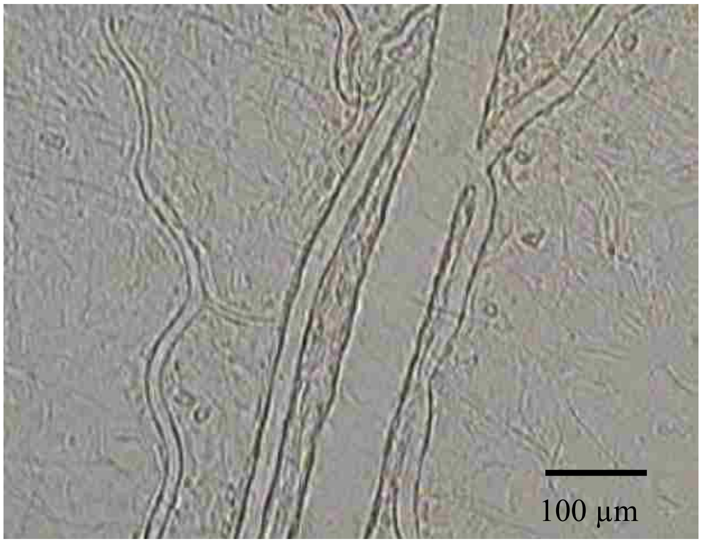

Figure 2.3 Microscopic view of microvessels in the rat mesentery after the blood was replaced by saline.

2.3 Ultra-high Speed Photomicrography

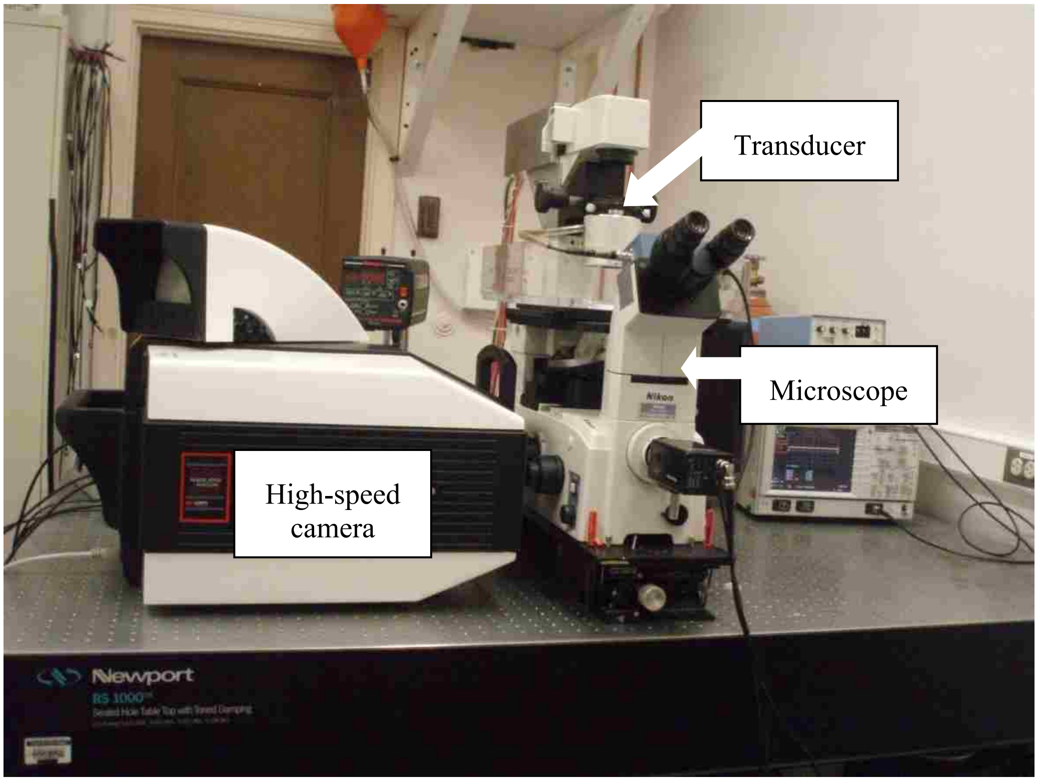

Figure 2.4 Picture of the experimental system with the main components marked out.

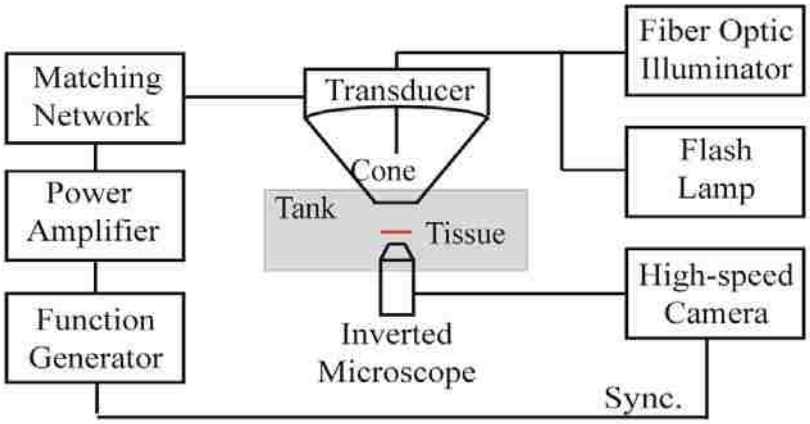

Figure 2.5 Schematic illustration of the experimental setup.

A synchronized optical-acoustic system was set up (Figures 2.4 and 2.5) for the ultra-high speed imaging.

2.3.1 Optical System

The specifications of the ultra-high speed camera (Imacon 200; DRS Hadland, Cupertino, CA, USA) are listed in Table 2.1. This camera was coupled to one side port of an inverted microscope (TE2000-U; Nikon Inc., Melville, NY, USA). A Panasonic color video camera (GP-KR222) capable of capturing 30 frames per second was connected to another side port of the microscope. Dynamic recording using the ultra-high speed shutter-controlled camera and continuous monitoring of the tissue sample with the video camera were in the same optical setup and switched by simply changing the optical output path of the microscope. The microscope was connected to a 40× water-immersion objective (nominal numerical aperture 0.8; nominal working distance 3.5 mm; nominal depth of field 0.43 μm). In addition, a 10× water-immersion objective was also connected to the microscope to help in finding microvessels on the mesentery, as it has a larger field of view than the 40× objectives. The inverted microscope provided a large working space above the microscope stage. An acrylic tank (L×W×H: 355×265×90 mm) filled with phosphate buffered saline solution was located on the stage. The water tank had an opening at its bottom. A latex glove was used to seal this opening using the side near the wrist and to couple the objective with the water tank using one finger of the glove with the finger tip cut away. The illumination was provided by a Y-shaped optical fiber with one of its two arms coupled to a halogen lamp (Model 41500-50; Cole-Parmer Instrument Co.,

Table 2.1 Ultra-high speed camera specifications

Items	Specifications
Camera type	MCP/CCD
Company, model	Hadland, Imacon 200
Maximum frame frequency	200,000,000 fps
Minimum exposure time	5 ns
Resolution power: H×V (pixels)	1200×980
Maximum number of frames	14

Vernon Hills, Illinois, USA) for long-term video recording with a standard CCD camera, and the other coupled to a high-intensity Xenon flash lamp (IMS 300; IMC, Burbank, CA, USA) for the ultra-high speed imaging. The flash lamp provided a high intensity point source of ~25 μs duration at 300 Joules nominal power (Joules is energy. intensity is power/unit area), with a rise time of typically 7 μs.

2.3.2 Acoustic System

A high-intensity focused ultrasound (HIFU) transducer (H102; Sonic Concepts, Bothell, WA, USA) of a center frequency of 1 MHz, a geometrical focal length of 63 mm and an f-number of about 1 was held by a fixture directly above the microscope objective. The full width half maximum dimensions (FWHM) of the focal region were 1.8 mm × 11.5 mm in the radial and axial directions of the sound field, respectively. The transducer has a hole in

Table 2.2 Specifications of the ultrasound transducer

Items	Specifications
Center frequency	1.1 MHz
Active diameter	64 mm outer diameter 22 mm inner diameter
Geometric focus	63 mm
F-number	0.98
Bandwidth (-3dB)	±250 KHz around the fundamental
Focal width (FWHM)	1.33 mm
Focal depth (FWHM)	13.5 mm

its center which was designed for incorporating a diagnostic ultrasound probe. Here, the optical fiber coupled to the two lamps was inserted through this hole to provide illumination for the microscopic imaging. The transducer was driven by a single cycle sinusoidal electrical pulse produced by a function generator (33120A; Hewlett Packard, Palo Alto, CA, USA) and amplified by a power amplifier (ENI A150; ENI, Rochester, NY, USA).

A fiber-optic probe hydrophone (FOPH 2000; RP Acoustics, Leutenbach, Germany) was used to align the transducer to be co-focused with the microscope objective and then to calibrate the acoustic system. The FOPH was first positioned at the center of the microscope's field of view, and the position of the transducer was then adjusted until

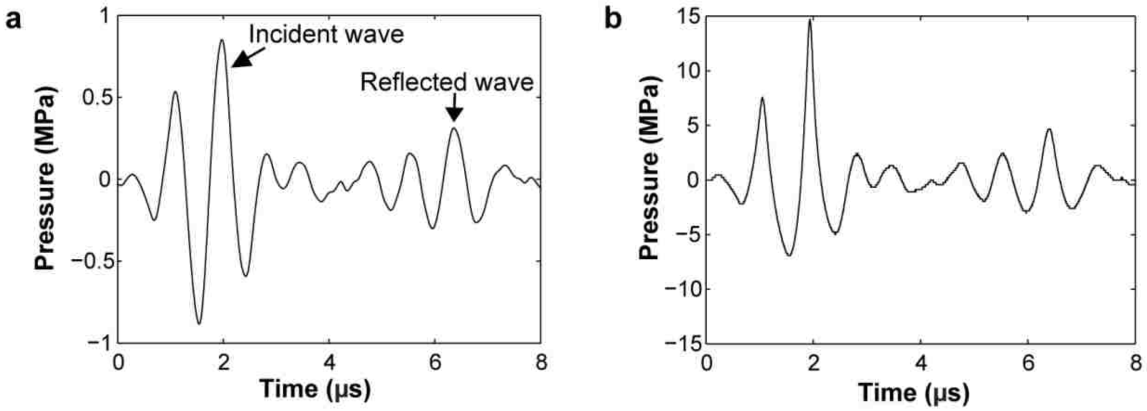

Figure 2.6 Representative pressure waveforms. The FOPH was used to measure the pressure at the focus of the transducer at (a) relatively low pressure [PNP = 0.8 MPa] or (b) relative high pressure [PNP = 6.4 MPa]. The nonlinear acoustic propagation effect is pronouncedly shown in b.

the pressure measured by the FOPH was maximal. In this way, the transducer and the objective were co-focused. Examples of the measured waveform at this focus are displayed in Figure 2.6. Each acoustic pulse initially reached the hydrophone at 0 μs. Because of the transducer ringing effect, the single cycle excitation pulse typically produced an acoustic pulse width of about 2 μs, thereby the incident acoustic pulse was about 2 cycles long. After this pulse traveled to the objective, it was reflected back to the hydrophone, thus both the incident wave and reflected wave were recorded (Figure 2.6). The time delay of the reflected wave was about 4.3 μs. The ultrasound pulses used in this study had peak negative pressures (PNP) ranging from 0.8 MPa to 7.2 MPa.

2.3.3 Ultra-high Speed Imaging Procedure

The prepared tissue sample was put into the water tank and aligned to the co-focal plane of the microscope objective and the transducer. Then the injection of microbubbles started. When microbubbles were found in the field of view of the microscope, the function generator was triggered manually to send out a pulse to drive the transducer. Meanwhile, the SYNC signal from the function generator was used to trigger the ultra-high speed camera. After the camera was triggered, it first sent out a pulse to trigger the flash lamp, and then sequentially captured 14 high-speed image frames. The delay between the trigger signal of the flash lamp to the first frame of the high-speed image sequence was set to be the rise time of the flash lamp. The delay of the first frame was set to the time of flight of the ultrasound pulse from the transducer to the tissue. Therefore the first frame was captured when the ultrasound pulse just arrived at the tissue sample. A total of 14 frames (Figure 2.7) were captured following each trigger event.

Real-time observation of microbubble oscillation requires the exposure time of each frame on the order of nanoseconds. In this study, the exposure time for each frame was 50 ns, if not otherwise specified. The inter-frame time was typically 300 ns to record the dynamics of microbubbles under the exposure of only the incident pulse. Under this condition, the entire recording time of the ultra-high speed camera was about 4 µs, which was shorter than the time necessary for the reflected acoustic wave to arrive back to the tissue sample. As such, the presence of the 40× objective did not affect the observed bubble-vessel interactions.

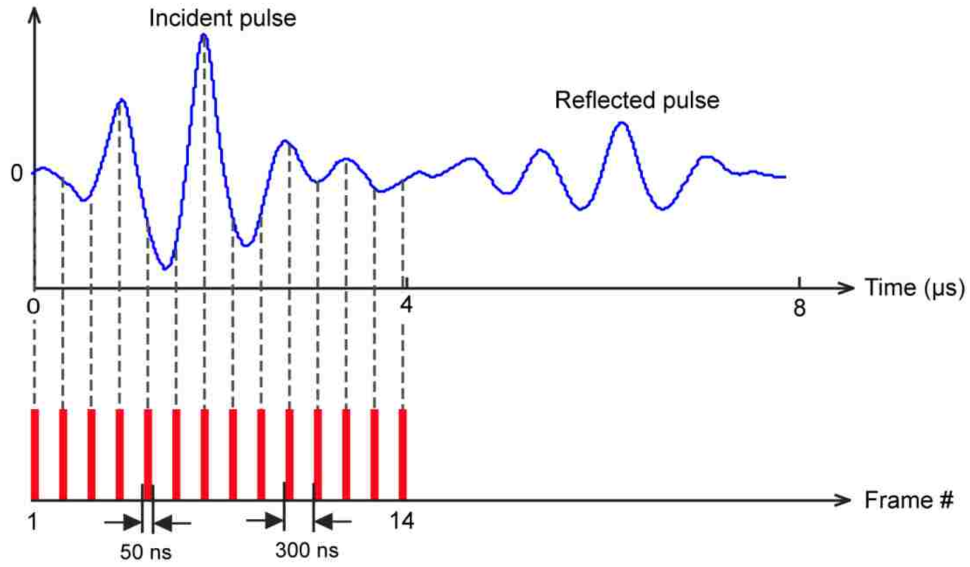

Figure 2.7 Illustration of the system timing. The upper panel represents the incident ultrasound wave. The lower panel shows the timing for the ultra-high speed imaging.

2.3.4 Image Analysis Methods

The image analysis methods applied to all the image sequences are introduced as follows. In Chapters 3–6, specific measurements associated with the study reported in each chapter are introduced there. To perform measurements from the selected image sequences, images were calibrated against a stage micrometer with 10 µm per division. Using ImageJ software (ImageJ 1.41o; National Institutes of Health, Bethesda, MD, USA), the scale of the high-speed images was determined to be 6.3 pixels/µm for the 40× objective. The resulting scaling was used in concert with a custom Matlab program (Mathworks Inc., Sherborn, MA, USA) that allowed the marking of characteristic points and the measurement of corresponding distances. All measurements were repeated by interactively marking each selected image sequence three separate times. Averages of the resulting measurements are presented here. Limited by user variability, the clarity of the image, and frame-to-frame distortion characteristic of the camera, the measurement uncertainty was estimated to range from 1–3 μm.

To analyze the interactions between microbubbles and microvessels, the following measurements were acquired from each image sequence: the initial vessel diameter D, the initial bubble-vessel distance L, the maximum equivalent microbubble radius $R_{\max}$. In the frame captured before vessel wall motion was observed, the initial vessel diameter D was measured along a line passing through the pixel coordinates of the center of the microbubble when it first appeared, perpendicular to the vessel axis (Figure 2.8a). The microbubble center was defined by the intersection of two lines drawn by the user to define the maximum lengths of the microbubble along the axial and radial directions of the microvessel. The initial bubble-vessel distance L was then measured as the distance from the initial location of the microbubble center to the initial position of the nearest vessel wall (Figure 2.8a). Note that the image plane was adjusted to pass approximately through the midplane of the vessel, and the nearest vessel wall was defined as the vessel wall closest to the microbubble in the image plane (this distance was not necessarily the shortest bubble-vessel distance in 3-D space). Such an assumption is required by the present technique because only events within a very shallow image plane (focal depth ~0.4 μm) were observable. The equivalent microbubble radius was quantified as follows. First, the maximum lengths of the microbubble along axial and radial directions of the

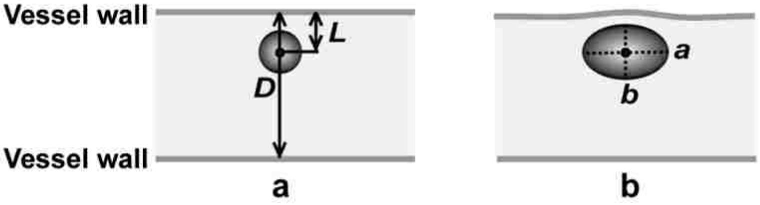

Figure 2.8 Illustration of several measured quantities from each selected image sequence. (a) The initial vessel diameter D and bubble-vessel distance L were measured before vessel wall motion was observed. (b) At the maximum expansion state of the microbubble, the equivalent microbubble radius $R_{\max}$ was calculated using a and b, which are the maximum half-lengths of the microbubble along the axial and radial directions of the microvessel, respectively.

microvessel were measured, and their half-lengths were denoted a and b, respectively (Figure 2.8b). Second, the volume of the microbubble was estimated as $(4/3)\pi ab^2$ by assuming the microbubble was a prolate spheroid with equatorial radius b. Last, an equivalent radius was calculated as the radius of a spherical microbubble with the same volume. The maximum of the measured equivalent radius in each sequence was denoted as $R_{\max}$. The assumption that the microbubbles were prolate spheroids was made in consideration of the cylindrical geometry of the vessel and the observation that many of the microbubbles were close to an elliptical shape in 2-D. Besides the assumption of a prolate spheroid, note that some additional uncertainty is inherent in the measurement of R_{max}, because the bubble is not always exactly centered in the image plane, for which the focal depth was much smaller than the maximum bubble size.

2.4 Limitations

2.4.1 Limitations of the Animal Model

2.4.1.1 Tissue Thickness

The rat mesentery is so thin that it is almost transparent. To evaluate how the limited thickness of the tissue surrounding the vessel might have affected observations, we compared the viscous dissipation in the surrounding tissue with limited thickness to unbounded thickness. Viscous dissipation was chosen for analyses because viscosity of the surrounding tissue may play a significant role in bubble-vessel interactions (Freund, 2008). For geometrical simplicity, we assume a spherical microbubble in a concentric spherical vessel surrounded by spherical viscoelastic tissue, as illustrated schematically in Figure 2.9. The radius of the spherical vessel is V_R and the half thickness of the surrounding tissue is T.

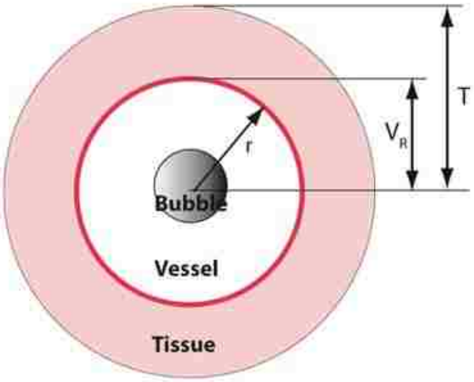

Figure 2.9 Model for a spherical microbubble in a concentric spherical vessel surrounded by spherical viscoelastic tissue.

Assuming that the medium (liquid inside the vessel, vessel wall and the surrounding tissue) is incompressible and maintains the same density, the particle radial velocity is:

$$u(r,t) = \dot{R}\left(\frac{R}{r}\right)^2 , \qquad 2.1$$

where u is the radial velocity, r is the radial coordinate, R is the radius of the oscillating microbubble, and overdot means the time derivative. For spherically symmetric fluid motion, the rate of viscous energy dissipation per unit volume in an incompressible fluid can be expressed as:

$$\phi = 2\mu_t e_{ij} e_{ij} = 2\mu_t\left[\left(\frac{\partial u}{\partial r}\right)^2 + 2\left(\frac{u}{r}\right)^2\right] = 12\mu_t \frac{\dot{R}^2 R^4}{r^6}, \qquad 2.2$$

where e_{ij} is viscous tensor and μ_t is the viscosity of the tissue (Kundu & Cohen, 2002). By integrating ϕ over one cycle (τ) of the bubble oscillation and over the whole spherical volume of the tissue, we get the total viscous energy dissipation (E) in the tissue. Assuming the tissue extended from V_R to infinity to simulate the unbounded tissue case, the total viscous energy dissipation in the surrounding tissue in the unbounded case, E_∞ is:

$$E_\infty = \int_{V_R}^{\infty}\int_0^{\tau} 2\pi r \phi\, dr\, dt = \mu_t \frac{1}{V_R^{\,3}}\int_0^{\tau} 16\pi \dot{R}^2 R^4 dt \,. \qquad 2.3$$

Total viscous energy dissipation that is not captured by the mesentery with a limited thickness 2T is the part dissipated within the volume from T to infinity. This energy E_T is:

$$E_T = \int_T^{\infty} \int_0^{\tau} 2\pi r \phi dr dt = \mu_t \frac{1}{T^3} \int_0^{\tau} 16\pi \dot{R}^2 R^4 dt \quad 2.4$$

The fraction of the energy dissipated in the surrounding tissue of a mesentery sample can then be calculated using $E_\infty - E_T$. The effectiveness of the mesentery tissue in viscous dissipation, γ, defined by the viscous energy dissipated in the surrounding tissue divided by the 'maximal' amount of viscous dissipation E_∞ is:

$$\gamma = \frac{E_\infty - E_T}{E_\infty} = 1 - (\frac{V_R}{T})^3 . \quad 2.5$$

The thicknesses of several mesentery tissue samples were measured based on histology sections. For each of these samples, the thickness was about 1.7 times the diameter of the target vessel within the sample. For T / V_R = 1.7 (*i.e.*, V_R / T = 0.58), about 80% of a 'maximal' amount of viscous dissipation would be captured by the mesentery tissue (Figure 2.10). This result suggests that the mesentery tissues are thick enough to serve as an effective model for vessels surrounded more extensively by viscous tissue.

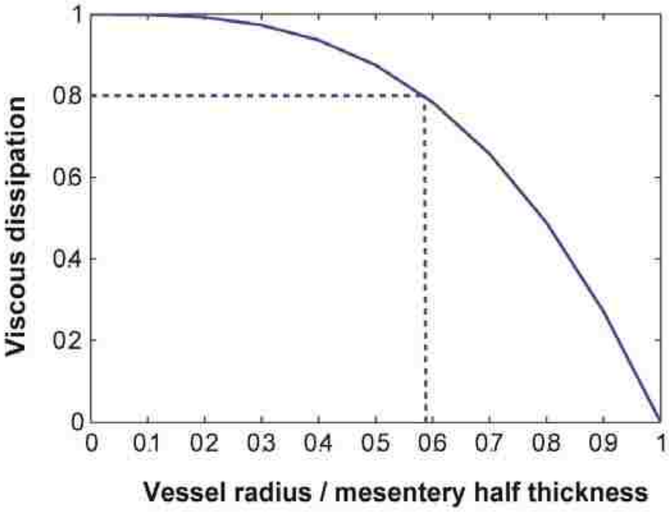

Figure 2.10 The effectiveness of the mesentery tissue in viscous dissipation with respect to the ratio of vessel radius to mesentery half thickness. When this ratio is 0.58, the viscous dissipation is about 80%.

2.4.1.2 Tissue Preparation

The blood in the microvessels was replaced by saline containing a very low concentration of green India ink. The viscosity of blood is about 3–4 times larger than saline. However, at the pressure levels used in this study, the microbubble collapsed inertially as demonstrated by the high-speed images shown in this study. The dynamics of the microbubbles are controlled by the inertial of the surrounding liquid rather than the viscosity, so the presence of blood would have had minimal impact on the observed qualitative behaviors. However, in the *in vivo* setting, the microbubbles are surrounded by red-blood cells (RBCs). The presence of RBCs close to microbubbles may change the microbubble dynamics, thereby influencing the interaction of the microbubbles with the microvessels. Therefore, to what extent that the present findings can be generalized to a clinical setting is not known; however, they provided some insight into our understanding of the fundamental physics of how microbubbles induce damage to microvessels.

Microvessels are highly reactive; the surgical procedure, introduction of the cannulas, and any manipulation of the tissue can potentially rupture the microvessels. One phenomenon that was observed commonly was that microvessels in the mesentery can 'disappear' within the network of connective tissue fibers. Similar vessel 'disappearance' phenomena were reported as early as 1971 (Gaehtgen & Uekerman, 1971). The possible explanation is that the rupture of some microvessels happened, and as a result, there was no flow in these vessels. Without flow, they could not be discriminated from the surrounding tissue due to the thin wall of the microvessels. The rupture of the microvessels accompanied by potential blockage of smaller ones, especially capillaries, by coagulated red blood cells, made it hard to set up a closed loop perfusion system. Collectively, these conditions 'conspire' such that the possibility of observing microbubbles in capillaries is low.

In addition, the experiment was performed at room temperature, but not at body temperature (around 37 ^{o}C). At higher temperature, the microbubbles may expand to larger diameters and have a decreased stability (Mulvana *et al.*, 2010).

2.4.2 Limitations of the Imaging Technique

There are two major limitations of the high-speed imaging technique.

2.4.2.1 Ultra-high Speed Camera

The ultra-high speed camera used in this study is a powerful tool, but it can only capture 14 frames at each trigger event, which is not enough for the study of long duration event. Furthermore, the spatial resolution of the imaging system was on the order of 500 nm. When microbubble sizes were small, especially when they were undergoing collapse, it was difficult to identify them in the images.

2.4.2.2 Reflection of Ultrasound from the Objective

Given the arrangement of the tissue samples relative to the microscope objective, the relatively long working distance of the microscope objective allowed high-speed images to be captured before the acoustic reflections from the objective reached the tissue sample. However, for larger microbubbles which oscillate for longer periods of time, the reflected wave will confound microbubble dynamics observations to some extent by influencing bubble behaviors.

2.5 Summary

An ultra-high speed photomicrography system was set up for the observation of microbubble dynamics in actual microvessels in real time, and techniques for administration microbubbles into the microvessels of *ex vivo* animal tissue were developed. They were used in the studies presented in the following chapters for understanding the coupled behaviors of microbubbles and microvessels that are important to the applications of microbubbles in ultrasound diagnoses and therapies.

Chapter 3

Observations of Translation and Jetting of Ultrasound-activated Microbubbles in Microvessels[1]

3.1 Introduction

The success of microbubbles in the clinics has spurred their development for new applications in both diagnostic and therapeutic ultrasound, including molecular imaging and drug and gene delivery therapies (Cosgrove & Harvey, 2009; Pichon *et al.*, 2008; Stride & Coussios, 2010; Villanueva & Wagner, 2008). In molecular imaging, microbubbles are conjugated with site-specific targeting ligands that allow binding of the microbubbles to disease markers expressed on the endothelium of blood vessels. They have been explored for screening, diagnosing, and monitoring diseases at the molecular level (Pysz *et al.*, 2010). For drug and gene delivery therapies, microbubbles can be loaded with pharmaceutical agents such as chemotherapeutic drugs and large genetic materials, monitored during perfusion using diagnostic ultrasound, and then forced to release the carried materials at the targeted location by higher power ultrasound. Moreover, interactions between ultrasound-activated microbubbles and the vessel wall can increase the permeability of the endothelium, thus enhancing the delivery of

---

[1] Based on: Chen, H., Brayman, A. A., Kreider, W., Bailey, M. R., & Matula, T. J. (Under revision). Observations of translation and jetting of ultrasound-activated microbubble in mesenteric microvessels. *Ultrasound in Medicine & Biology*.

pharmaceutical agents through the vessel wall (Ferrara, 2008; Skyba *et al.*, 1998). In both applications, the proximity of microbubbles to the endothelium is important. This close proximity can lead to mechanical interactions between microbubbles and vessels during exposure to ultrasound.

It has long been known that mechanical interactions between a cavitation bubble and a nearby boundary can induce bubble translation and jetting, where the direction of bubble translation and jetting depends on the properties of the boundary. A bubble oscillating near a rigid flat surface translates toward the surface and can form a liquid jet, directed toward the surface (Benjamin & Ellis, 1966; Johnsen & Colonius, 2009; Plesset & Chapman, 1971). The water hammer pressure associated with the impact of the liquid jet can damage hard surfaces (Blake & Gibson, 1987; Johnsen & Colonius, 2009; Philipp & Lauterborn, 1998). A bubble oscillating near a pressure-release boundary (*e.g.*, an air-water interface) moves away from the boundary during collapse and can form a liquid jet directed away from the boundary (Chahine, 1977; Robinson *et al.*, 2001). Near a compliant flat boundary, such as viscoelastic gel, the direction of bubble translation and jetting can be toward or away from the boundary, depending on the mechanical properties of the boundary, bubble size and distance from the boundary (Brujan *et al.*, 2001a, 2001b; Fong *et al.*, 2006; Gibson & Blake, 1982; Kodama & Tomita, 2000; Ohl *et al.*, 2009; Shima *et al.*, 1989). However, many of these previous studies focused on freely collapsing, millimeter-sized bubbles that are much larger than the microbubbles used in diagnostic and therapeutic ultrasound. Moreover, the flat boundaries used in these studies differ from actual blood vessels in mechanical properties and geometries.

Relatively little is known about microbubble translation and jetting behavior within microvessels, principally because of the technical difficulty of observing the dynamics of microbubbles in microvessels driven acoustically at megahertz frequencies. It has been shown experimentally that the acoustic radiation force on microbubbles in a 50 μm diameter arteriole could drive the microbubbles to translate along the transducer's acoustic axis (Dayton *et al.*, 1999). Microjet formation in a 200 μm diameter cellulose tube has been recorded (Postema *et al.*, 2004), demonstrating that liquid jets can be formed by encapsulated microbubbles in tubes. Although the recorded image did not show the direction of the microjet relative to the tube wall, the authors suggested that in clinical applications microjets may direct toward and impinge on the endothelial wall. The first observation of single-microbubble dynamics in actual microvessels was reported by Caskey *et al.* (Caskey *et al.*, 2007). They observed ultrasound-activated microbubbles in microvessels of *ex vivo* rat cecum, recording microbubble translation toward the vessel wall and a toroidal bubble morphology consistent with the formation of a microjet. The stroboscopic technique by which these images were acquired produced one image per ultrasound pulse; by repeated sampling over many pulses at different phases, the full dynamics of the microbubble could only be inferred. The limitation of this technique, as mentioned earlier, is that it is applicable only to repeatable events. Nevertheless, Caskey *et al.* suggest that microbubbles translate and form microjets directed toward vessel walls, and that microjet impact on vessel walls is a mechanism for microbubble-enhanced vascular permeability and/or vascular damage.

To investigate explicitly the transient interactions between microbubbles and microvessels, the interactions between individual microbubbles and microvessels were studied here. *Ex vivo* rat mesenteries were insonated by single ultrasound pulses and image sequences were captured using the ultra-high speed photomicrography system introduced in Chapter 2. In this chapter, the direction and magnitude of translation and jetting of the microbubbles are the endpoints of principle interest.

3.2 Methods

3.2.1 Animal Tissue Preparation

The same animal preparation protocol as described in Section 2.2 was used here.

3.2.2 Ultra-high Speed Imaging

The same ultra-high speed photomicography technique as described in Section 2.3 was used here.

3.2.3 Image Analysis

The three quantities: (1) the initial vessel diameter D, (2) the initial bubble-vessel distance L, and (3) the maximum equivalent microbubble radius $R_{\max}$ were measured as described in Section 2.4. To quantify the translational displacements of microbubbles, the centers of the microbubbles were first identified and then the radial displacements of the bubble centers relative to their initial positions were calculated.

Note that in all the image sequences, the direction of ultrasound propagation was orthogonal to the image plane (*i.e.*, into the plane of the page or screen). Consequently, the primary acoustic radiation force (or the primary Bjerknes force) was orthogonal to the observation plane. Since the microbubbles remained visible in the image plane after insonation, the effect of the radiation force on microbubble translation in or out of the image plane could not be discerned.

3.3 Results

3.3.1 Microbubble Translation

In total, 80 high-speed image sequences were selected for analyzing microbubble translation. Each selected sequence was required to satisfy two criteria. First, the recorded interaction involved a microvessel and a single microbubble, or, if additional microbubbles were visible in the microvessel, the microbubble of interest had a maximum radius at least twice that of other microbubbles, or remained separated from other microbubbles by at least two maximum bubble radii. Second, the 2-cycle ultrasound pulses drove microbubbles to oscillate; to ensure consistent comparisons of microbubble translation distances, only image sequences that recorded microbubbles undergoing at least two inertial growth and collapse events within the initial 4 μs were selected.

To aid in the presentation of results, the measured quantities D, L, and $R_{\max}$ were used to calculate two dimensionless parameters: the relative size of the microvessel, as identified by the ratio of the initial vessel diameter to the maximum microbubble diameter ($D/2R_{\max}$); and the relative proximity of the microbubble to the nearest vessel wall, as represented by the dimensionless standoff distance ($L/R_{\max}$). Note that bubble-vessel distances changed during each image sequence due to movements of both the microbubble center and the vessel wall. The standoff distance was defined using the initial bubble-vessel distance L to be consistent with a conventional definition of bubble standoff distance in related work (Brujan *et al.*, 2001b; Shima *et al.*, 1989).

Figure 3.1 presents three image sequences showing microbubble translation in microvessels. Corresponding measurements of bubble translation and vessel displacement are plotted for each sequence in Figure 3.2. These image sequences were selected to include microbubbles at different standoff distances ($L/R_{\max}$) ranging from ~ 0.2–1.1.

At the largest standoff distance, Figure 3.1a shows the dynamics of a microbubble with $L/R_{\max}$ = 2.4 (in the image plane, the upper vessel wall is nearest). In this case, the microbubble was relatively far from the vessel wall; the vessel wall and the microbubble center moved slightly during microbubble oscillation. The final net translational distance of the microbubble was ~5 μm, and the maximum displacement of the vessel wall was ~3 μm (Figure 3.2a)

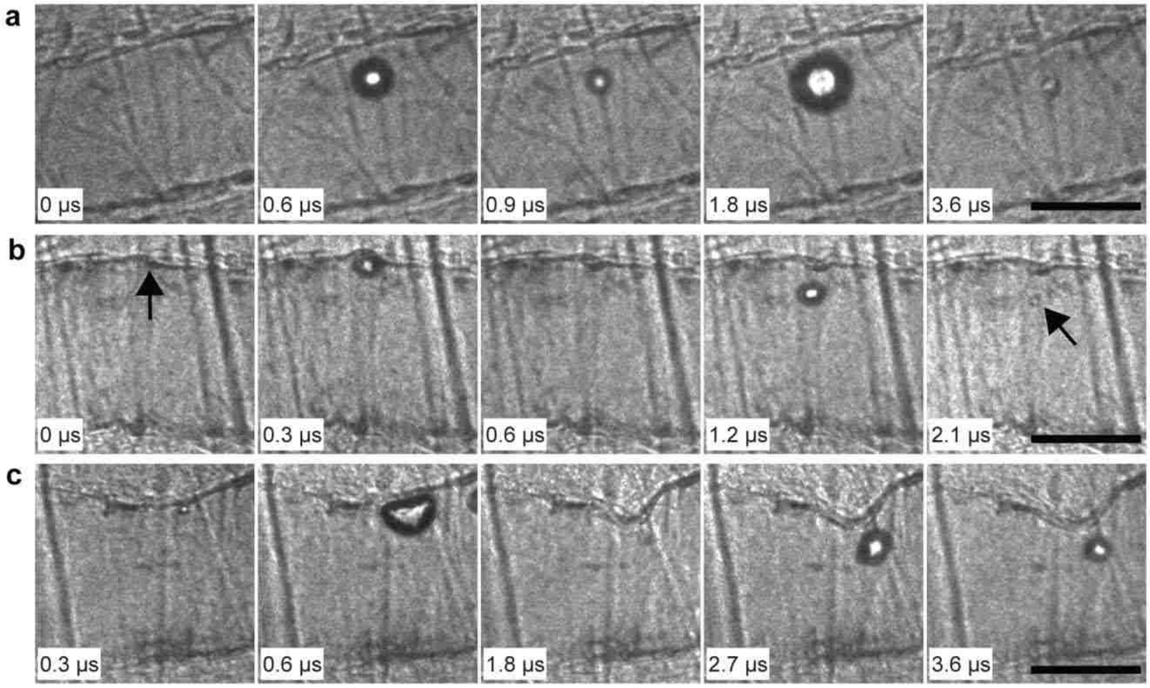

Figure 3.1 Selected high-speed image sequences that show microbubble translation in microvessels. A time stamp for each frame is located at the bottom left corner, and the scale bar on the bottom right of each sequence represents 50 μm. (a) D = 68 μm, $D/2R_{\max}$ = 2.4, $L/R_{\max}$ = 1.1 and PNP = 1.5 MPa. (b) D = 78 μm, $D/2R_{\max}$ = 5.2, $L/R_{\max}$ = 0.5 and PNP = 1.5 MPa. The arrow in the first frame indicates the initial location of the vessel wall that moved during microbubble oscillation. The arrow in the last frame points to the microbubble. (c) D = 73 μm, $D/2R_{\max}$ = 3.7, $L/R_{\max}$ = 0.2 and PNP = 4 MPa.

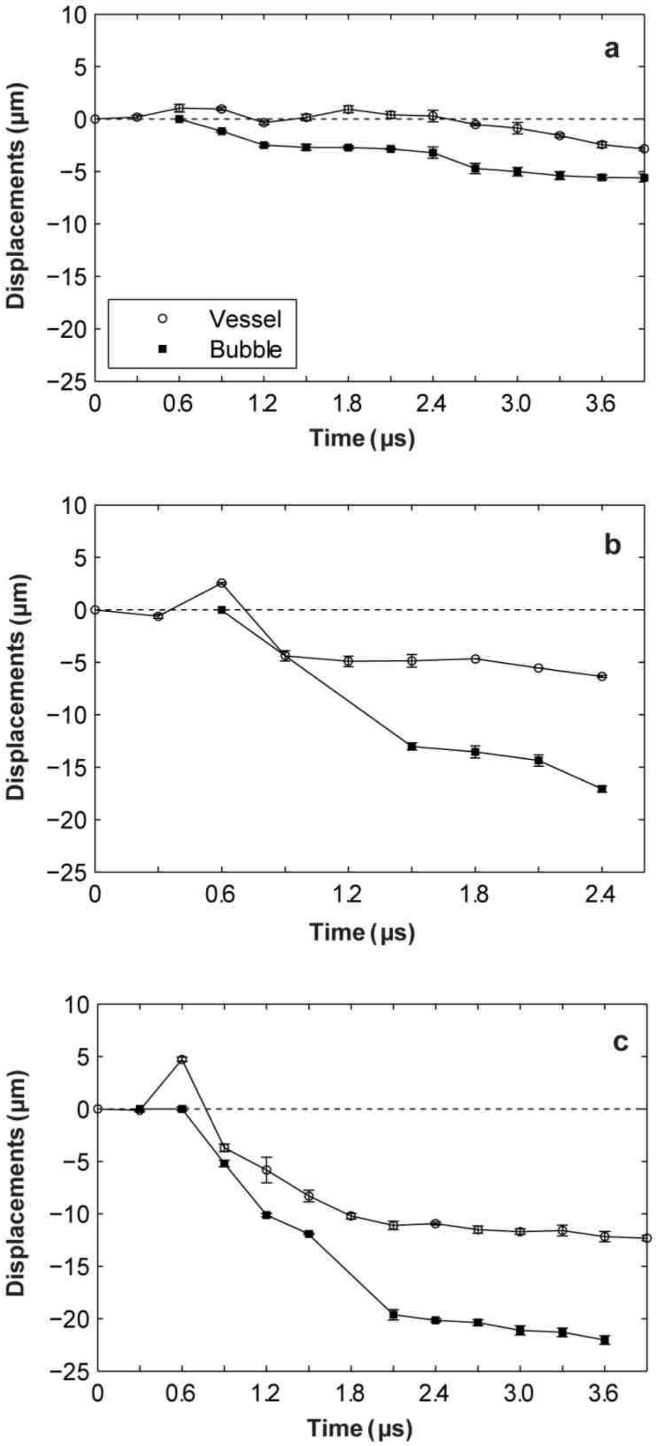

Figure 3.2 Displacements of the microbubble center and vessel wall for cases (a), (b) or (c) shown in Figure 3.1 respectively. The error bars are standard errors of the measurements.

Figure 3.1b shows the translation of a microbubble at a smaller standoff $L/R_{\max}$ = 1.1. At 0.6 µs, the microbubble had expanded against the upper wall, resulting in localized distention of the vessel. The subsequent collapse of the microbubble at 0.9 µs (the microbubble is not visible in the image) led to local invagination of the upper vessel wall, which remained invaginated in all subsequent frames (see Figure 3.2b for quantification of vessel displacement). At 1.5 µs, the microbubble appears to be spheroidal in shape, and its center had moved away from the upper vessel wall by 13 µm. Later at 2.4 µs, the microbubble collapsed again and translated even further from the upper vessel wall, reaching a final translation distance of 17 µm (Figure 3.2b).

Figure 3.1c displays the dynamics of a microbubble with $L/R_{\max}$ = 0.5, the smallest among the three cases. In this case, the interaction between the microbubble and the vessel wall was strong, as indicated by the flattening of the microbubble during its expansion and substantial deformation of the nearest vessel wall. At 0.6 µs, the microbubble had expanded and flattened against the upper vessel wall, and the upper vessel wall was distended. The subsequent collapse of the microbubble at 1.8 µs coincided with invagination of the upper vessel wall. The vessel wall continued to move inward even when the microbubble re-expanded at 2.7 µs. At 3.6 µs, the vessel invagination reached 12 µm, accompanied by translation of the microbubble center by 22 µm (Figure 3.2c). Similar to the case shown in Figure 3.1b, vessel wall displacements were observed only on the upper vessel wall while the lower vessel wall remained stationary.

The examples from Figure 3.1 demonstrate characteristic behaviors as observed in this study of microbubbles in microvessels; *viz.*: (1) the extent of microbubble translation was related to the standoff distance; (2) final translation was directed away from the nearest vessel wall; and (3) microbubble translation was accompanied by deformation of the nearest vessel wall toward the lumen.

A common feature of these examples is that the vessel diameters were relatively large, with $D/2R_{\max}$ = 2.4, 5.2 or 3.7, respectively (Figure 3.1). Microvessels with $D/2R_{\max} > 2$ are considered here as being relatively large microvessels, in which most microbubbles at small standoff distances only caused displacements of the nearest vessel wall with no visible effect on the opposite side of the vessel. Overall, there were 41 image sequences recorded with a microbubble in a relatively large microvessel. Figure 3.3 displays the maximum microbubble translation distance as a function of $L/R_{\max}$ as measured from the 41 cases. The initial vessel diameters were in the range of 30–80 μm.

Among these cases, 23 involved translation away from the nearest vessel wall. In the other 18 cases, the microbubble remained stationary to within limits of uncertainty (as the measurement uncertainty was estimated to range from 1–3 μm, the vessel wall or the microbubble can be considered to be 'stationary' when the absolute value of its maximum displacement was less than 2 μm). No net translation of a microbubble was observed toward the nearest vessel wall. Furthermore, the data suggest that microbubble translation depended on $L/R_{\max}$.

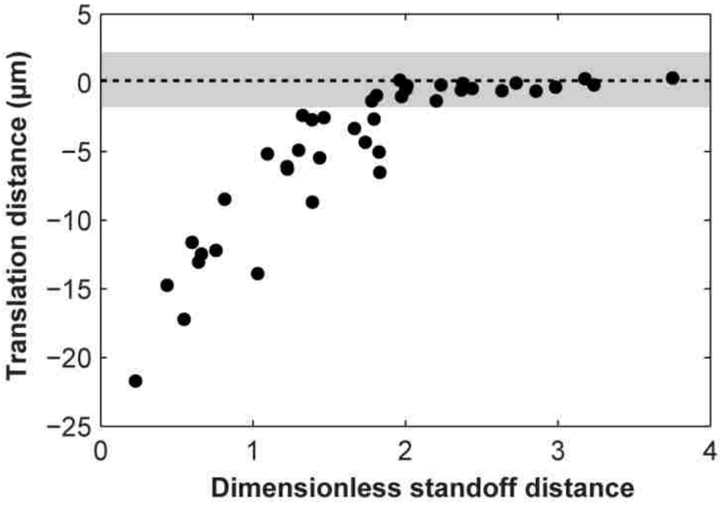

Figure 3.3 Plot of the maximum microbubble translation distance with respect to the dimensionless standoff distance $L/R_{\max}$ for relatively large microvessels ($D/2R_{\max} > 2$). Data points falling within the shaded region (± 2 μm) represent microbubbles that were considered to be stationary, with translation distances less than the resolution provided by measurements.

At high dimensionless standoff distances ($L/R_{\max} > 2$), microbubbles remained stationary; at low dimensionless standoff distances ($L/R_{\max} < 2$), microbubbles translated away from the nearest vessel wall, with the absolute translation distances increasing at smaller standoff distances. This threshold behavior should be considered qualitative only in the sense that errors of L and R_{max} can affect the value of the threshold.

In contrast to cases with relatively large microvessels, in cases with relatively small microvessels ($D/2R_{\max} < 2$), most microbubbles induced displacements of both the near and far vessel walls in the imaging plane. Such interactions were recorded in 39 cases with the initial vessel diameters ranging from 10–45 μm. The measured maximum translation distances were typically smaller than those observed in relatively large vessels

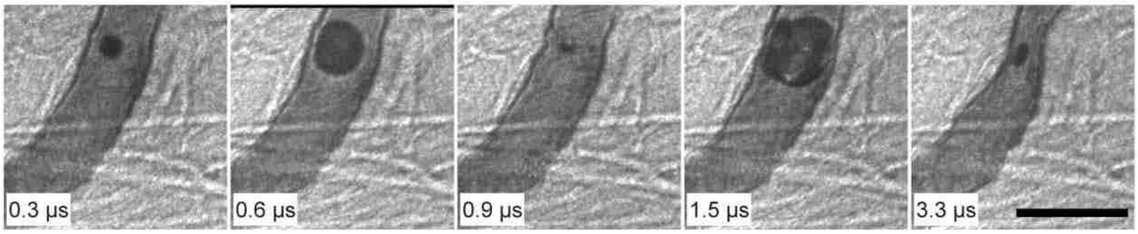

Figure 3.4 Microbubble translation in a relatively small microvessel. D = 28 μm, $D/2R_{\max}$ = 0.9, $L/R_{\max}$ = 0.6 and PNP = 1.5 MPa. The scale bar represents 10 μm.

at comparable standoff distances, though no measurable translation toward the nearest vessel was observed.

Figure 3.4 shows an image sequence of a microbubble in a relatively small microvessel with $D/2R_{\max} = 0.9$. For this case, $L/R_{\max} = 0.6$ (the left vessel wall is nearest). Both sides of the vessel experienced distention and invagination during microbubble expansion and collapse. In the last frame, both sides of the vessel became invaginated by about 8 μm, implying that the vessel may be distorted into an hourglass shape in 3-D space. During this interaction, the microbubble center translated away from the left vessel wall by a maximum of only 3 μm, which is much smaller than translations experienced by comparable microbubbles in relatively large microvessels (see Figure 3.3 at $L/R_{\max} = 0.6$).

3.3.2 Microjetting

In total, 19 high-speed image sequences were selected for analyzing microjetting (among them, 7 were also selected for translation analysis). For jetting, each selected sequence satisfied two criteria: (1) just as for the translation analysis, the recorded interaction involved a microvessel and an isolated or dominant microbubble; and (2) the direction of the microjet was clearly identifiable. These observations show that the direction of microjets was consistent with the translation direction: both were directed away from the vessel wall initially closest to the microbubble. Characteristic microjets are shown in Figure 3.5.

Figure 3.5a shows the formation of a microjet in a microbubble with $L/R_{\max} = 0.4$ relative to the left vessel wall. The microbubble expanded against the left vessel wall (0.3 and 0.6 μs), and then contracted (0.9 μs). It re-expanded at 1.2 μs and its center had moved by about 4 μm away from the left vessel wall. During further re-expansion, a microjet penetrated through the interior of the microbubble (1.8 μs). The direction of the microjet was away from the left vessel wall, as determined by the shape of the microbubble and also by the observation that the width of the microjet was widest near the left vessel wall. The length of the (identifiable) microjet was about 38 μm, which is smaller than the vessel diameter. Consequently, the microjet does not appear to impact the vessel wall. Additionally, if we assume that the microjet started to form at 0.9 μs, an average speed of 42 m/s can be estimated between 0.9 and 1.8 μs. This estimate is probably a lower bound, as the microjet may have started to form later at the end of collapse or early in the rebound (Blake & Gibson, 1987).

Figure 3.5b shows a microjet in a microbubble with $L/R_{\max} = 0.3$, relative to the left-side vessel wall. Similar to Figure 3.5a, the microbubble of interest (marked by the arrow) expanded and flattened against the left vessel wall, deforming to almost a hemispherical shape (0.6 µs). In the third frame (0.9 µs), the microbubble had collapsed and translated away from the left side vessel wall by 6 µm; also, the left-side vessel wall became invaginated by 3 µm (this invagination remained even when the microbubble re-expanded at 1.2 µs). In the last frame (1.8 µs), the re-expanding microbubble contacted both sides of the vessel wall, and a microjet had penetrated the microbubble in the direction away from the left vessel wall. The length of the microjet was about 22 µm, and the average speed of the microjet is estimated to be 24 m/s. In this case, the microjet was directed away from the left vessel wall and had a length similar to the vessel diameter; consequently, the jet may have impinged directly on the opposite vessel wall. Note that slight bending of the jet toward the lower position of the vessel wall was observed, which may have been caused by the presence of the small microbubble visible in the first two frames, or by the geometry of the vessel wall next to the microbubble.

The characteristic features of the 19 observed jets can be summarized as follows: (1) during the initial expansion phase, the microbubble appears to contact the vessel wall at one site, flattening somewhat against it; (2) the microjet, which may start to form during the collapse or re-expansion phase of the microbubble, is clearly visible during the re-

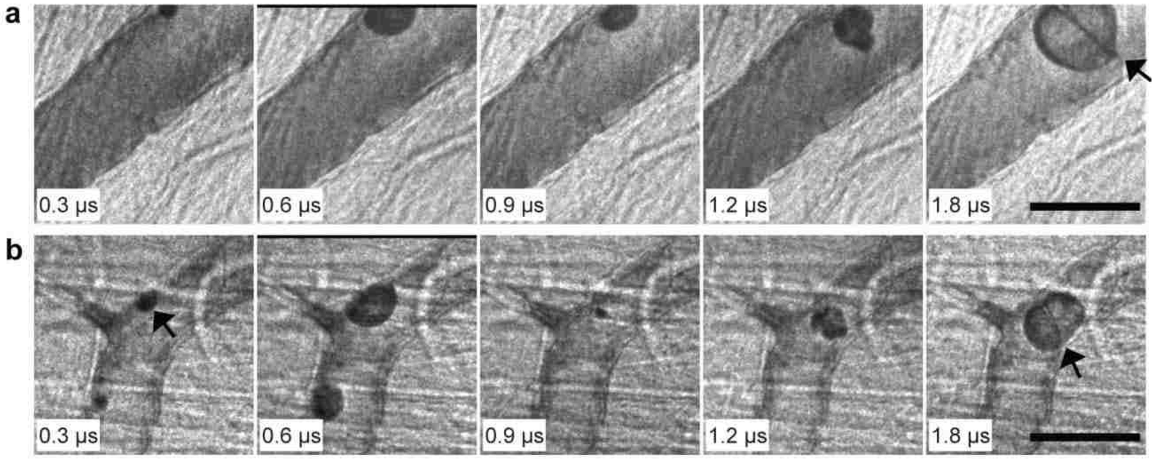

Figure 3.5 Microjets formed in microvessels. (a) D = 48 µm, $L/R_{\max}$ = 0.4 and PNP = 3 MPa. (b) D = 30 µm, $L/R_{\max}$ = 0.3 and PNP = 1.5 MPa. In the last frame for each case, the microjet pointed out by an arrow. The arrow in the first frame of b indicates the microbubble of interest. The scale bar in each sequence represents 10 µm.

expansion phase and is directed away from the contact site; and (3) $L/R_{\max} < 1$ in all of the cases. In this work, leakage of dye out of the microvessels was not observed before, during or after high-speed imaging.

3.4 Discussion

The results presented in this study – observations of microbubble translation and jetting *away* from the nearest boundary – are limited to vessels in *ex-vivo* rat mesenteries. These vessels are surrounded principally by a thin membrane comprised by structural proteins, and thus differ from tissues such as muscle or the parenchyma of solid organs, in which there is a more fully 3D tissue architecture and there exist extravascular interstitial spaces. It was established earlier that the mesentery is sufficiently thick to 'capture' ~80% of microbubble induced viscous dissipation (see Section 2.4.1.1), and is a reasonable if imperfect model of more fully 3-D tissues. Furthermore, mechanically, the mesentery, as with other real tissues, exhibits nonlinear strain stiffening (Fung, 1993), and thus mechanical effects observed in the mesenteric vessels are likely more representative of vessels in more fully 3D biological tissues than are the synthetic materials that have been studied in the past.

The direction of bubble translation or jetting has been studied by many researchers. These studies showed that near a boundary the direction of bubble translation and jetting depends on the mechanical properties of the boundary. For a bubble near a compliant boundary (as in the present case), the boundary can be deformed by the expansion of the bubble. This deformation stores elastic energy, which can be released as the bubble collapses. This type of bubble-boundary interaction can create a pressure gradient that drives flow away from the boundary; if this gradient is large enough, translation and jetting away from the boundary can occur (Blake & Gibson, 1987; Brujan *et al.*, 2001a, 2001b; Shima *et al.*, 1989). Moreover, when the bubble collapses, a low-pressure region is developed between the collapsing bubble and the boundary, which pulls the boundary to move inward. The inward movement of the boundary pushes flow away from the boundary, which may also contribute to translation and jetting away from the boundary. For example, Shima *et al*. (Shima *et al.*, 1989) studied the migration of spark-induced bubbles near various viscoelastic composite surfaces and found that bubbles always migrated away from very flexible surfaces. Brujan *et al*. (Brujan *et al.*, 2001b) observed laser-induced cavitation bubbles; for the least-stiff gel boundaries they considered, bubble translation and jetting were also directed away from the boundary.

In addition to the mechanical properties of a nearby boundary, microbubble translation and jetting also depend on the proximity of the boundary. As demonstrated by Figure 3.1, for relatively large microvessels (that is $D/2R_{\max} > 2$), the extent of microbubble translation increased with decreasing standoff distance $L/R_{\max}$. At standoff distances exceeding ~2, no measurable translation was observed. A similar dependency of bubble translation on $L/R_{\max}$ was reported by Kodama and Tomita (Kodama & Tomita, 2000), who investigated the translation of laser-generated bubbles at different standoff distances from a flat gelatin surface as a model of *in vivo* bubble dynamics near human tissue. This similarity suggests that relatively large microvessels may behave like flat boundaries with respect to microbubble/vessel interactions. For relatively small microvessels, microbubble translation tended to be reduced as illustrated by Figure 3.4, which may be due partially to the influence of the non-planar vessel geometry. Furthermore, microjets were observed only for $L/R_{\max} < 1$, suggesting that strong interactions between microbubbles and vessel walls were necessary for the formation of clearly visible microjets. Of 51 data sets that satisfied the condition $L/R_{\max} < 1$, 19 showed clear signs of jetting. There may have been other cases where jet structures were not visible because they were out of the image plane.

These results have implications for microbubble-mediated molecular imaging and drug and gene delivery, which rely on the proximity of microbubbles to vessel walls. For example, the study of microbubble adhesion is typically done in flow chambers, where the effect of flow on adhesion can be quantified (Schmidt *et al.*, 2008; Zhao *et al.*, 2004). The present results suggest that the compliance of the vessels should also be considered. Observed bubble translations away from the nearby vessel wall imply that the direct coupling between vessels and microbubbles will act in opposition to adhesion forces. In addition, the finding that microjets were always directed *away* from the nearest vessel wall suggests that microjet impingement may not be the dominant mechanism by which microbubbles increase the permeability of microvessels whose diameters exceed microjet lengths. However, in smaller microvessels, whose diameters were smaller than microjet lengths, vascular rupture by microjetting may occur, as the microjets directed away from the nearest vessel wall may impact the opposite vessel wall. Figure 3.6 demonstrates that a liquid jet may contribute to the rupture of smaller microvessels. At frame 1.6 μs, a liquid jet appears to be formed inside the microbubble. It directed away from the left vessel wall and toward the right vessel wall, appearing to impact the right vessel wall. At frame 4 μs, the microbubble deformed to a mushroom-shaped form with its stem stretching through the vessel wall. In the last frame, the collapsed microbubble (arrow) was observed in the interstitial space outside the vessel wall

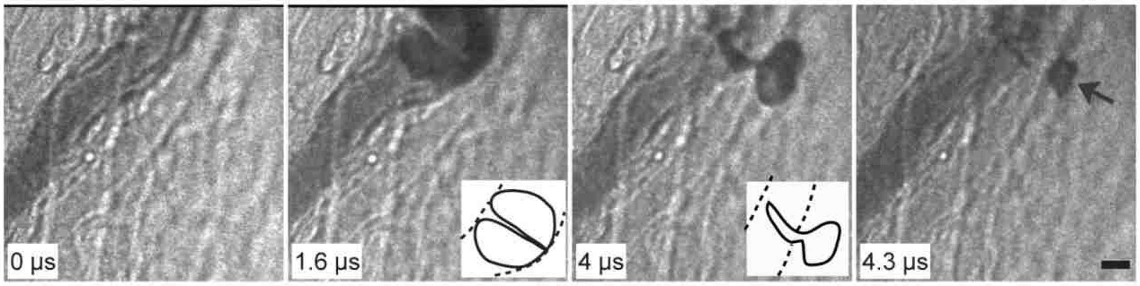

Figure 3.6 Vascular rupture involving a liquid jet. PNP = 4 MPa. Vessel diameter = 15 μm. Sketches of the bubble at 1.6 μs and 4 μs are marked with the microbubble in solid lines and microvessel in dashed lines.

3.5 Summary

The transient dynamics of individual microbubbles in microvessels of the *ex vivo* rat mesentery insonated by single ultrasound pulses were recorded using real-time, ultra-high speed photomicrography. The image sequences show that interactions between ultrasound-activated microbubbles and microvessels led to microbubble translation *away* from the nearest vessel wall. They also demonstrate the formation of microjets directed away from the nearest vessel wall. These observations appear to be characteristic of a strong coupling between ultrasound-driven microbubbles and compliant microvessels.

Chapter 4

Blood Vessel Deformation on Microsecond Time Scales by Ultrasound Cavitation[2]

4.1 Introduction

Recent observations of microbubbles near lipid membranes (Marmottant & Hilgenfeldt, 2003), biological cells (Prentice *et al.*, 2005; Van Wamel *et al.*, 2004) or viscoelastic gels (Brujan *et al.*, 2001a; Delacrétaz *et al.*, 1997) indicate that a nearby compliant boundary can be deformed by 'pushing' and 'pulling" forces associated with volumetric bubble oscillations. Although significant in demonstrating how microbubbles and viscoelastic materials interact, these previous studies were performed *in vitro* and do not directly address the clinical environment in which microbubbles are injected into blood vessels to provide imaging contrast for some types of diagnostic ultrasound studies, or to try to achieve therapeutic effects. In addition to possessing unknown viscoelastic properties, blood vessels also impose a volumetric confinement on bubble oscillations. Constrained within blood vessels, microbubbles excited by ultrasound not only can rupture the vessel (Miller *et al.*, 2008), but also can affect the vascular endothelium; there is hope that the latter effect can be exploited to modify vessel permeability to enhance local drug or gene delivery (Ferrara *et al.*, 2007; Marmottant & Hilgenfeldt, 2003; Shen *et al.*, 2008).

---

[2] Based on: Chen, H., Kreider, W., Brayman, A. A., Bailey, M. R., & Matula, T. J. (2011). Blood vessel deformations on microsecond time scales by ultrasonic cavitation. *Physical Review Letters*, 106(3), 034301.

Accordingly, numerical simulations (Freund, 2008; Miao *et al.*, 2008; Qin *et al.*, 2009; Qin & Ferrara, 2006; Ye & Bull, 2006) and experiments (Caskey *et al.*, 2007; Van Leeuwen *et al.*, 1993; Zhong *et al.*, 2001) have sought to elucidate how bubbles and vessels interact. In this chapter, ultra-high speed microphotography techniques were used to directly observe the transient interactions between ultrasound-activated microbubbles and microvessels within *ex vivo* tissue, with a focus on the deformation of the microvessels induced by the cavitation microbubbles.

4.2 Methods

4.2.1 Animal Tissue Preparation

The same animal preparation protocol as described in Section 2.2 was used here. Microvessels with diameters of 8 μm or less were classified as capillaries; arterioles and venules were distinguished by the flow direction and vessel branching and collecting (Kobayashi et al. 2002). In this study, microvessels with diameters ranged from 10 to 100 μm were selected, therefore they were either venules or arterioles.

4.2.2 Ultra-high Speed Imaging

The same ultra-high speed photomicography technique as in Section 2.3 was used here.

4.2.3 Image Analysis

The same methods as introduced in Section 2.4 were used to measure the initial vessel diameter D and the maximum equivalent microbubble radius $R_{\max}$. In this study, the deformation of the vessel wall induced by the cavitation microbubbles was of specific interest. To quantify the vessel wall displacements, the radial displacements of the vessel wall at the point closest to the microbubble center were measured using MATLAB. First, an axial line determining the orientation of the vessel's axis was defined by user selection. Second, a point was selected by the user to define the center of the microbubble. Then a line was drawn through the center of the microbubble and perpendicular to the vessel to define the radial direction of the vessel. Third, aided by the radial direction guideline, the user identified the point on the vessel wall that intersected with the guideline. Last, the displacements of this point in each frame relative to its initial positions were measured to quantify the deformation of the vessel wall. Movement toward the vessel lumen was defined as negative.

4.3 Results

The confinement imposed by vessels and surrounding tissue did not prevent bubbles from undergoing large volumetric oscillations that included inertial collapses. In turn, vessels deformed on the same microsecond time scale as microbubble oscillations. In most cases involving either venules or arterioles, the extent of vessel-wall invagination was observed to be greater than the corresponding distention. This behavior is illustrated by the image sequence presented in Figure 4.1, in which microbubbles respond to a 6.4 MPa PNP pulse, leading to distention (middle) and invagination (right) of the upper vessel wall.

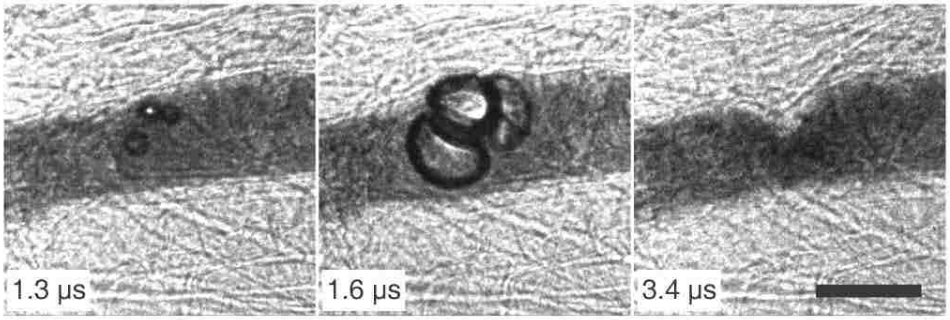

Figure 4.1 Characteristics of observed bubble-vessel interactions. A group of bubbles distends the vessel wall (middle); subsequent invagination (right) appears localized and markedly larger than the distention. The scale bar represents 50 μm.

Different types of bubble-vessel interactions were observed, as depicted in Figure 4.2. Each interaction is characterized by three images that show respectively the vessel at its initial state, at maximum distention, and at maximum observed invagination. In Figure 4.2a, the microbubble filled the vessel and contacted with both sides of the vessel wall; the subsequent invagination appeared to be circumferentially symmetric. In Figure 4.2b, the microbubble contacted with one side of the vessel wall during expansion, and the vessel distention and invagination were localized to a specific region of the vessel wall nearest the microbubble. In sequences shown in Figures 4.2c and 4.2d, invagination is apparent even though the microbubbles did not contact the vessel walls. In sequence c, both sides of the vessel wall invaginated, while in sequence d localized invagination was observed on the vessel wall nearest the microbubble.

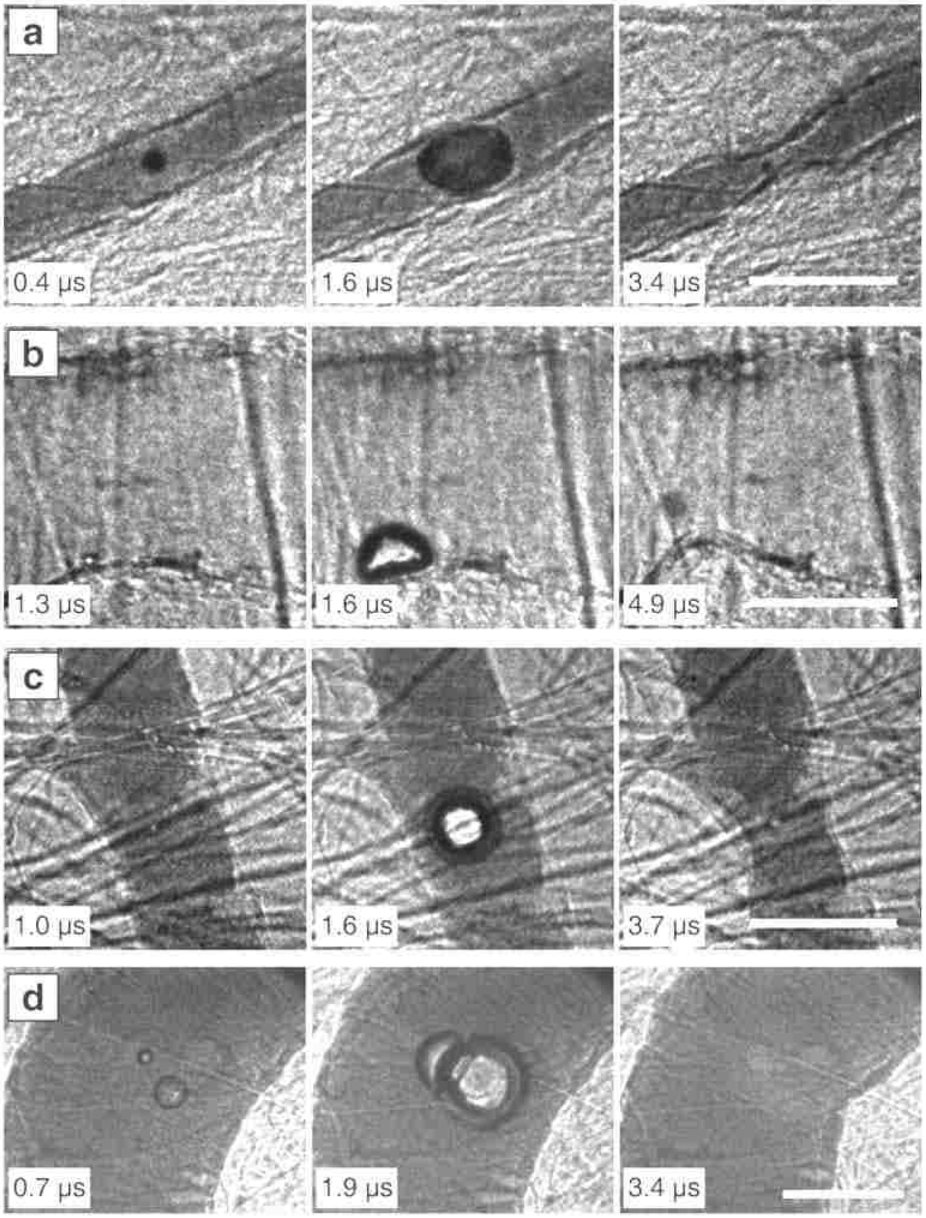

Figure 4.2 Image sequences to illustrate types of vessel invagination. In (a) and (b), localized vessel invagination was observed when the bubble contacted the vessel wall. In (c) and (d), the bubble did not contact the vessel wall, but still induced local vessel invagination. (a) PNP = 1.5 MPa; vessel diameter = 22 µm. (b) PNP = 4.0 MPa; vessel diameter = 71 µm. (c) PNP = 0.9 MPa; vessel diameter = 42 µm. (d) PNP = 7.2 MPa; vessel diameter = 100 µm. The scale bars represent 50 µm.

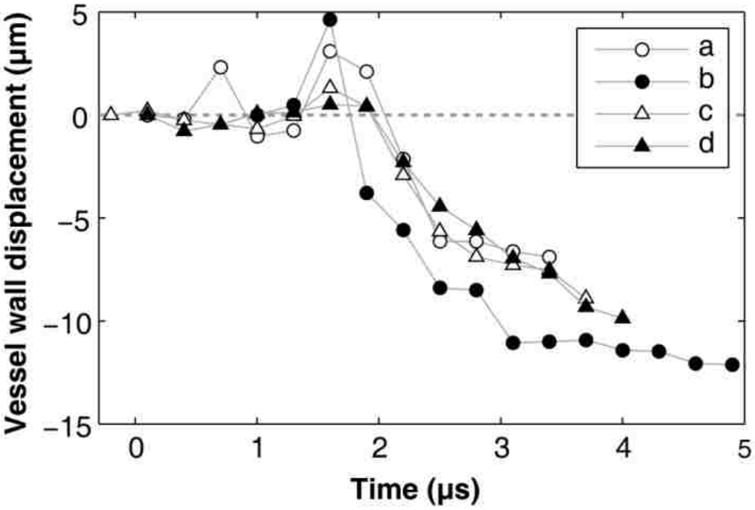

Figure 4.3 Measurements of radial displacements of the vessel wall at the point closest to the bubble for Figure 4.2a–d. Each marker denotes a measurement from a single image frame. Deflections toward the lumen were defined to be negative. For each of these sequences, vessel invagination exceeded distention by a significant margin. The observed invaginations occurred after bubbles collapsed (at about 2 μs in the plot) and persisted even after bubbles rebounded.

To quantify the observed vessel displacements from Figure 4.2, radial displacements of the point on the vessel wall closest to the center of the bubble were measured, and the results are plotted in Figure 4.3. In each of these cases, distention was small relative to invagination. Moreover, vessel walls behaved similarly in that the average inward wall speed was around 9 m/s over the time range from 1.5–2.5 μs. In addition, vessels achieved their maximum invaginations after the ultrasound pulse had passed and bubble motions had mostly ceased.

Although all of the previous examples just involved venules, similar invagination-dominated vessel responses were also observed in arterioles. Figure 4.4 shows a representative case of a microbubble in an arteriole exposed to a single ultrasound pulse

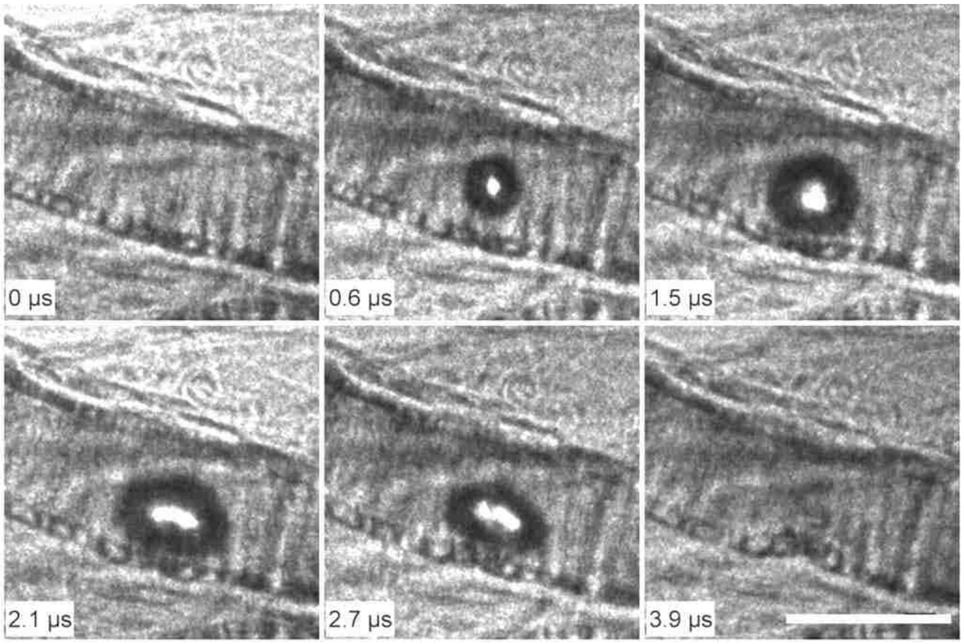

Figure 4.4 Representative high-speed image sequence to show the dynamic responses of an arteriole to a microbubble insonated at PNP 1.5 MPa. Vessel diameter = 35 μm; PNP = 1.5 MPa. The scale bar represents 50 μm.

with PNP = 1.5 MPa. The blood vessel has smooth muscle fibers wrapping around it as shown by the streaks crossing the vessel and small segments on the vessel wall. The microbubble expanded and almost touched the lower vessel wall at 2.1 μs. At this time, the lower vessel wall was distended by a maximum of 5 μm. Elongation of the microbubble was observed at 2.1 μs and 2.7 μs. The collapse of the bubble at 3.9 μs induced the invagination of the lower vessel wall by 7 μm, larger than the maximum distention.

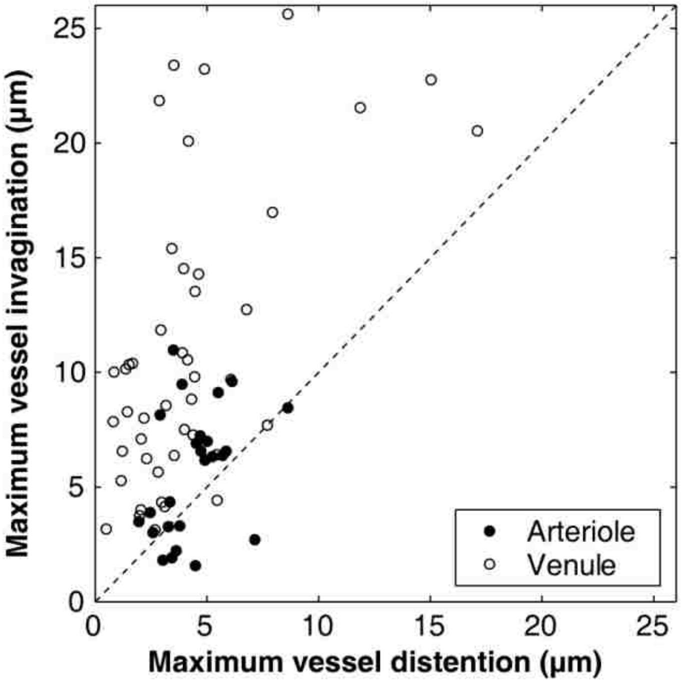

Figure 4.5 Comparison of maximum vessel invagination and distention. 45 cases involved venules, which were insonated with PNP ranged from 0.8–6.4 MPa. 25 data involved arterioles insonated only by an ultrasound pulse with PNP of 1.5 MPa.

To study vessel deformations, image sequences of bubble-vessel interactions were captured for a range of vessel sizes and pressure amplitudes. These observations specifically include cases in which an isolated or dominant target bubble could be identified, so that the interaction between that bubble and the surrounding vessel could be analyzed. In Figure 4.5, the resulting vessel deformation data are summarized, showing that invagination exceeded distention in 60 of 70 cases. Although the ratio of invagination to distention was not uniquely sensitive to pressure amplitude, larger vessel deformations did correlate with higher pressures. Based on the flow direction in the blood vessels, venules and arterioles were identified. For both venules and arterioles, invagination larger than distention was observed in most cases. However, arterioles account for 8 of the 10 observations in which invagination did not exceed distention. It seems reasonable to speculate that arterioles and venules have different stiffness, thereby affecting the interactions.

4.4 Discussion

Brujan (Brujan *et al.*, 2001a) notes that a compliant boundary can store energy when distended by an expanding bubble; as the bubble collapses, rebounding of the boundary creates a short-lived pressure gradient that tends to push flow away from the boundary. Note that as discussed in Chapter 3, if this gradient is large enough, microbubble translation and jetting away from the boundary can occur. Consistent with a pressure gradient and flow directed away from a flat boundary, it is instructive to now consider a streamline that begins far away, runs along the boundary, and enters the gap between the bubble and the boundary. As the boundary rebounds and the bubble collapses, flow along this streamline converges toward the bubble and the pressure in the gap would be lower than the equilibrium pressure far away. In this way, the rebound of a compliant boundary can lead not only to jets directed away, but also implies the imposition of a negative pressure in the gap between the bubble and the boundary, which would tend to create invagination-type deformation. This negative pressure may be higher than the positive pressure applied on the vessel wall during bubble expansion, which leads to vessel distention. Therefore, the biased vessel displacement was observed. Accordingly, observations of microbubble translation and jetting away from the nearest vessel wall and the prominence of vessel invagination appear to be linked behaviors.

Compare the timing of the bubble motions with the vessel response, it is evident that vessel deformations lagged the incident acoustic pressures and the corresponding bubble responses. Indeed, the maximum invaginations occurred after bubble motions had largely stopped (especially in sequences (a) and (c) of Figure 4.2). The time dependence of vessel deformations demonstrates that vessels and surrounding tissues exhibited both viscous and elastic properties.

4.5 Summary

Transient interactions among ultrasound, microbubbles, and microvessels were studied using ultra-high speed photomicrography. Vessel distention (motion outward against the surrounding tissue), and vessel invagination (motion inward toward the lumen) were observed. Contrary to current paradigms, invagination exceeded distention in most cases involving venules and arterioles, this was especially true for venules. These observations provide insight into the mechanics of bubble-vessel interactions, which appear to depend qualitatively upon the mechanical properties of biological tissues.

Chapter 5

Correlation of Microbubble Cavitation Induced Microvessel Deformation and Vascular Bioeffects[3]

5.1 Introduction

When microbubbles are excited by ultrasound, they undergo volumetric oscillations. The characteristic echoes produced by their oscillations have facilitated the development of contrast-enhanced ultrasound imaging techniques. Meanwhile, their oscillations introduce a potential for cavitation bioeffects on the nearby blood vessels (AIUM, 2000; Miller, 2007; Miller *et al.*, 2008; Miller & Brayman, 1997; Shohet & Grayburn, 2006).

Animal studies of bioeffects induced by ultrasound-activated microbubbles have demonstrated that microbubbless can cause immediate rupture of the microvessels in which these microbubbles are located (Ay *et al.*, 2001; Miller & Gies, 1998; Miller & Quddus, 2000). Among those studies, microscopic observations have been performed to directly observe microbubble-induced damage to individual microvessels. The first direct observation was reported by Skyba *et al.* (Skyba *et al.*, 1998). Using intravital microscopy of rat spinotrapezius muscles, they found that at MI > 0.4, microbubble destruction caused

---

[3] Based on: Chen, H., Brayman, A. A., Evan, A. P., & Matula, T. J. (In preparation.). Correlation of ultrasound-activated microbubble induced vessel deformation and vascular bioeffects. *Ultrasound in Medicine & Biology*.

Chen, H., Brayman, A. A., Bailey, M. R., & Matula, T. J. (2010). Blood vessel rupture by cavitation. *Urological Research*, 38(4), 321-326.

immediate rupture of capillaries with extravasation of red blood cells into the interstitial space. Later, rupture of microvessels larger than capillaries was demonstrated by Stieger *et al.* (Stieger *et al.*, 2007). They found the extravasation of a fluorescent dye from microvessels smaller than 55 μm in a chorioallantoic membrane model with ultrasound exposure corresponding to MI = 1.06. Apart from microvessel rupture, endothelial cell injury caused by ultrasound-activated microbubbles has also been reported. For example, Kobayashi *et al.* (Kobayashi *et al.*, 2002) examined endothelial cell injury directly in exteriorized rat mesenteries using propidium iodide, and found that microbubbles caused substantial endothelial cell injury at MI = 1.6, with the injury being observed more frequently in capillaries and venules than in arterioles and dominantly in venules. Besides these direct observation studies, microvessel damage induced by ultrasound-activated microbubbles has been found in many other investigations performed using tissues that are not suitable for direct observations, such as the heart, kidney and intestine (Aggeli *et al.*, 2009; Miller *et al.*, 2004; Miller & Gies, 1998; Tran *et al.*, 2009; Vancraeynest *et al.*, 2009; Wilbert, 2002). Although much has been done to study microbubble induced bioeffects, the fundamental physical mechanisms of how ultrasound-activated microbubbles induce microvessel damage still remain elusive.

Previous studies of freely collapsing, millimeter-sized bubbles near compliant boundaries suggested that deformation of the boundary induced by a nearby pulsating bubble is a potential mechanism for the damage of the compliant boundaries. One detailed study was performed by Brujan *et al.* (Brujan *et al.*, 2001b). Using high-speed imaging, they observed the dynamics of a laser-induced cavitation bubble near a flat polyacrylamide gel, and proposed that tensile-stress-induced uplifting of the boundary was one potential mechanism responsible for cavitation induced damage to biological tissues. In more confined vascular environment, Van Leeuwen *et al.* (Van Leeuwen *et al.*, 1993) recorded a laser-generated cavitation bubble in a dissected rabbit femoral artery by stroboscopic imaging technique, and found that expansion and collapse of the bubble induced dilation and invagination of the adjacent vessel wall, respectively. The subsequent histology studies found that damage to the artery was characterized by the abrasion of parts of the internal elastic lamina. They hypothesized that the vessel wall damage was due to the sequential insult of distention and invagination of the vessel.

Similarly, deformation of the blood vessels induced by a nearby pulsating microbubble has been proposed to be a mechanism for microvessel damage by ultrasound-activated microbubbles. Zhong *et al.* (Zhong *et al.*, 2001) observed microbubble interaction with a 200-μm diameter hollow fiber in a shock-wave field with PNP = 19 MPa, and found that rupture of the fiber was associated with significant dilation of the fiber by large microbubble expansion. Based on this study, it was proposed that vessel dilation caused by the expansion of a microbubble beyond the diameter of the vessels is a potential mechanism that may lead to microvessel damage by microbubbles in ultrasound field, although the hollow fiber used in this study had different mechanical properties from actual microvessels, and shockwaves are characteristically different from ultrasound pulses. Later, through direct observation of microbubbles in actual microvessels of the rat cecum insonated by ultrasound pulses with 1 MHz frequency and peak negative pressure of either 0.8 MPa or 2 MPa, Caskey *et al.* (Caskey *et al.*, 2007) confirmed that, microbubbles excited by ultrasound pulses could induce vessel dilation. However, this study used streak and strobe imaging, which did not fully capture the transient dynamics of the microbubbles and microvessels. Moreover, the correlation of the observed vessel dilation and vascular bioeffects was not explored.

As discussed in Chapter 4, microbubble expansion and collapse were found to induce the distention and invagination of the microvessels, with vessel invagination typically exceeding distention in venules and arterioles. The aim of the study presented in this chapter was to assess the association of the observed vessel dynamics and possible vascular bioeffects, to provide insight into the mechanisms of microvessel damage by ultrasound-activated microbubbles.

5.2 Methods

5.2.1 Animal Tissue Preparation

Animal tissue preparation follows the methods described in Section 2.2.

5.2.2 Ultra-high Speed Imaging

The same ultra-high speed photomicography technique as described in Section 2.3 was used, with the difference that longer inter-frame times were used in this study. As shown previously (Figure 2.6), after the ultrasound pulse was sent from the transducer to the tissue sample, it was reflected from the optical objective lens back into the tissue sample.

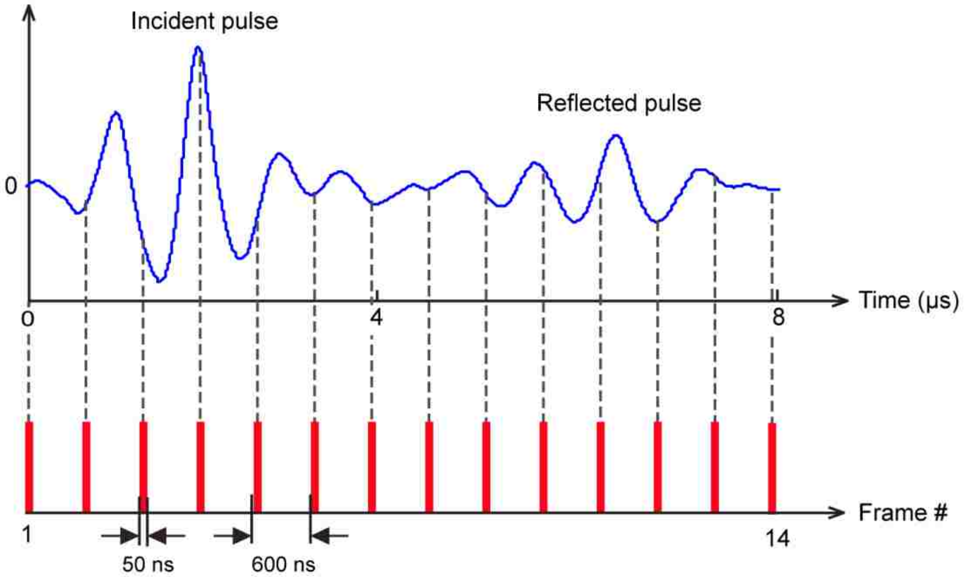

Figure 5.1 Illustration of system timing. The upper panel represents the incident and reflected ultrasound waves. The lower panel shows the timing setup of the ultra-high speed camera.

The time delay of the reflected wave was about 4.3 μs, and the total length of the ultrasound pulse including both the incident and reflected pulses was about 8 μs. In this study, the guiding hypothesis was that there would exist a correlation between the dynamics of bubble-vessel interactions and the resulting vascular bioeffects. The effect of the reflected ultrasound pulse on the bubble-vessel interactions was considered by taking the images using an inter-frame time of 600 ns, unless otherwise specified. Therefore, the entire recording time was about 8 μs, which spans insonation of the tissue sample by both the incident and reflected ultrasound pulses (Figure 5.1).

5.2.3 Image Analysis

The initial vessel diameter D was measured as described in Section 2.4. The vessel wall displacements were measured as described in Section 4.2.3. At the recorded maximum expansion, $R_{\max}$ was calculated using $R_{\max} = \sqrt{A/\pi}$, where A was the cross-section areas of the microbubble measured using IMAGEJ (NIH, http://rsb.info.nih.gov/ij/). Previously, images with isolated microbubbles were selected for analysis, and $R_{\max}$ was measured by assuming the microbubbles to be prolate spheroids (Section 2.4). Here, cases with microbubble clusters containing several microbubbles were also included for analysis. The shape of the microbubble clusters were irregular, thus the method based on the cross-section area was used.

5.2.4 Vascular Bioeffects Assessment

In contrast to previous studies, in the present studies vascular bioeffects were examined after the high-speed images were captured. Obvious microvascular rupture was indicated by the observations of microbubble extravasation from the microvessels. For damage that was not obviously visible, histology and transmission electron microscopy (TEM) studies were performed. These methods are described below. A targeted microvessel was exposed to the ultrasound pulse only once at the location of a microbubble, so that only one image sequence with a microbubble present was captured for each selected targeted microvessel. To reduce the chance that a targeted microvessel might be insonated more than once, any two targeted microvessels were at least 1.5 mm apart, in consideration of the FWHM transaxial diameter of the ultrasound beam.

To prepare the tissue sample for histology or TEM analysis, a home-made tissue holder (a circular shape annulus with a diameter of 1.5 cm and an O-ring (see Figure 5.2)) was used to capture a piece of the mesentery containing the targeted microvessel. Color images of the captured tissue sample were captured, and landmarks (bifurcations, fat cells, etc.) near the targeted microvessel were used later to facilitate the identification of the targeted microvessel. One example of how the color images were used to locate the targeted microvessel is illustrated by Figure 5.2. The tissue sample was captured by a tissue holder with an O-ring (image shown on the upper left corner). Two black fiducial marks on the tissue define the ROI at the macroscopic level. The mosaic images in the center were taken using low magnification microscopy to better define the ROI. The images on the right were recorded using the same optical setup as the high-speed imaging but with a CCD camera. By comparing the images on the right with the corresponding high-speed images, the location where the acoustically excited microbubble had been up could be identified. Reference points were selected and their distances to the ROI were used to determine precisely the location of the ROI for histology and TEM studies.

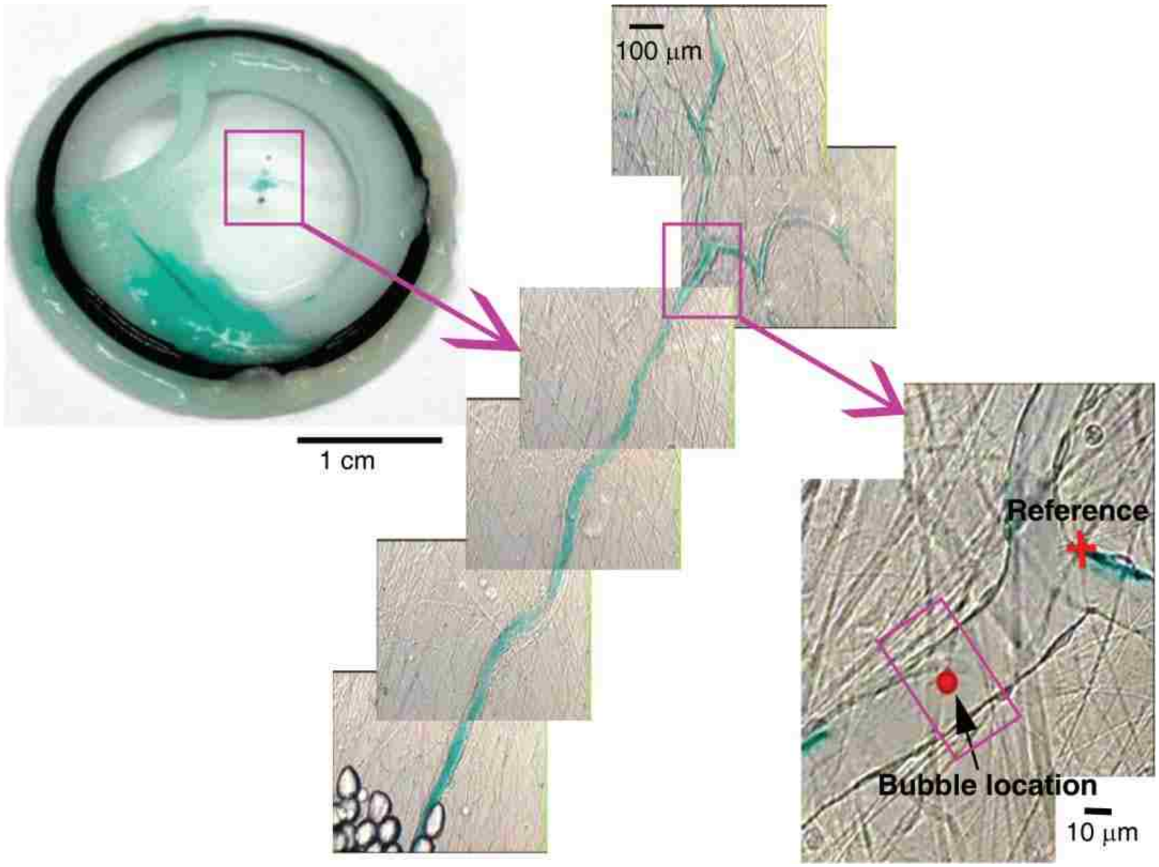

Figure 5.2 Illustration of the image registration method used to locate precisely the region of interest (ROI) for histology or TEM studies.

For histology analysis, each tissue sample was fixed by 4% parafomaldehyde solution. The fixed tissue was embedded in glycol methacrylate through a series of deformalinization, dehydration and dealcoholization. Due to the need for accurate and precise sectioning from specific regions of the sample, the sample was left in the tissue holder until just before it was embedded. After the embedding mixture polymerized and cooled, the block was placed under a stereo microscope to carefully re-mark fiducial landmarks, as noted in the recorded color images, on the outside of the block. These markers were used as reference points during sectioning to help identify the targeted microvessel. Sections were cut at 4-µm increments through the region on the targeted microvessel that had interacted with the microbubble recorded in the high-speed image sequence. These sections were subsequently stained with Lee's methylene blue and examined by a light microscope.

To confirm the histology results and also examine the vascular structure at a sub-cellular level, tissue samples were also used for TEM analysis. Each tissue sample was first fixed in a Karnovsky's fixative. After washing with cacodylate-sucrose buffer, it was post fixed in osmium tetroxide, washed with deionized water, stained with uranyl acetate and then rinsed several times with water. After dehydrated through a graded series of alcohols and propylene oxide, the sample was infiltrated with resin and polymerized overnight. The targeted microvessel was identified with the help of the recorded color images. Sections as thin as 100 nm were cut at 10-µm steps through the region on the targeted microvessel that had interacted with the recorded microbubble. Subsequently, these sections were mounted on grids and stained with uranyl acetate and lead citrate. Finally, they were examined using a transmission electron microscope (JEM 1200EX II; JEOL, Tokyo, Japan).

For both histology and TEM analyses, control sections were obtained from either the targeted microvessels on sections away from the region that had interacted with the recorded microbubble, or microvessels out of the ultrasound treated region. In addition, both the histology and TEM results were interpreted by Dr. Andrew P. Evan in Indiana

University School of Medicine, who has more than 25 years' experience in studying tissue damage by lithotripsy pulses.

5.3 Results

In the *ex vivo* rat mesentery, microvessel damage was found to be associated with two different characteristic types of vessel responses to the cavitation microbubbles: (1) in large microvessels, whose initial diameters D were larger or comparable to the maximum equivalent diameters of microbubbles $2R_{\max}$, vessel response was dominated by invagination; (2) in small microvessels with D much smaller than $2R_{\max}$, both vessel invagination and distention were significant. Here the terms 'large microvessels' and 'small microvessels' were operationally defined to facilitate comparison between these two characteristic responses of the microvessels. In the following, the correlations between vessel responses and vascular damage are presented for small and large microvessels, respectively.

5.3.1 Relatively Large Microvessels

In the study presented in Chapter 4, it was found that in 60 out of 70 cases with isolated microbubbles in microvessels of a wide range of diameters (10–100 μm) insonated by single ultrasound pulses with a broad range of PNP (0.8–7.2 MPa), vessel invagination exceeding distention was typically observed. $D/2R_{\max}$ of the microvessels in these 70 cases was within the range of 0.8–6.0, indicating that D was comparable to or larger than $2R_{\max}$. Therefore they are all considered here to be large microvessels. In the present work, the ultra-high speed images revealed similar vessel responses in large microvessels. The histology and TEM studies showed that this invagination-dominated response could be associated with vascular damage, which was characterized by the separation of part of the endothelium from the vessel wall.

Figure 5.3 presents one image sequence of microbubble interaction with a venule. The vessel diameter D = 35 μm and the ultrasound pulse PNP = 4 MPa. Figure 5.3a shows that before the reflected ultrasound pulse arrived at the tissue at ~4 μs, two microbubbles was observed to expand, collapse, re-expand and finally to re-collapse. Coalesce of these two microbubbles were observed in the frames captured from 1.8 μs to 3 μs. At 1.8 μs, the microbubbles were at the recorded maximum expansion state with $R_{\max}$ = 17 μm; the vessel wall was pushed by the expanding microbubbles to move slightly outward, reaching the maximum distention of 3 μm (Figure 5.3b). The collapse of the coalesced microbubbles led to the invagination of the vessel (3.6 μs). When the reflected pulse arrived (4–8 μs), another cycle of microbubble expansion and collapse was observed and the vessel remained invaginated. The vessel reached its maximum invagination at the end of the recorded image sequence (7.8 μs), which was 10 μm (Figure 5.3b). In this case, the vessel was considered to be a large microvessel, as the ratio $D/2R_{\max} = 1$. The vessel distention was not obvious; however, invagination was significant. Therefore, the vessel response was dominated by invagination.

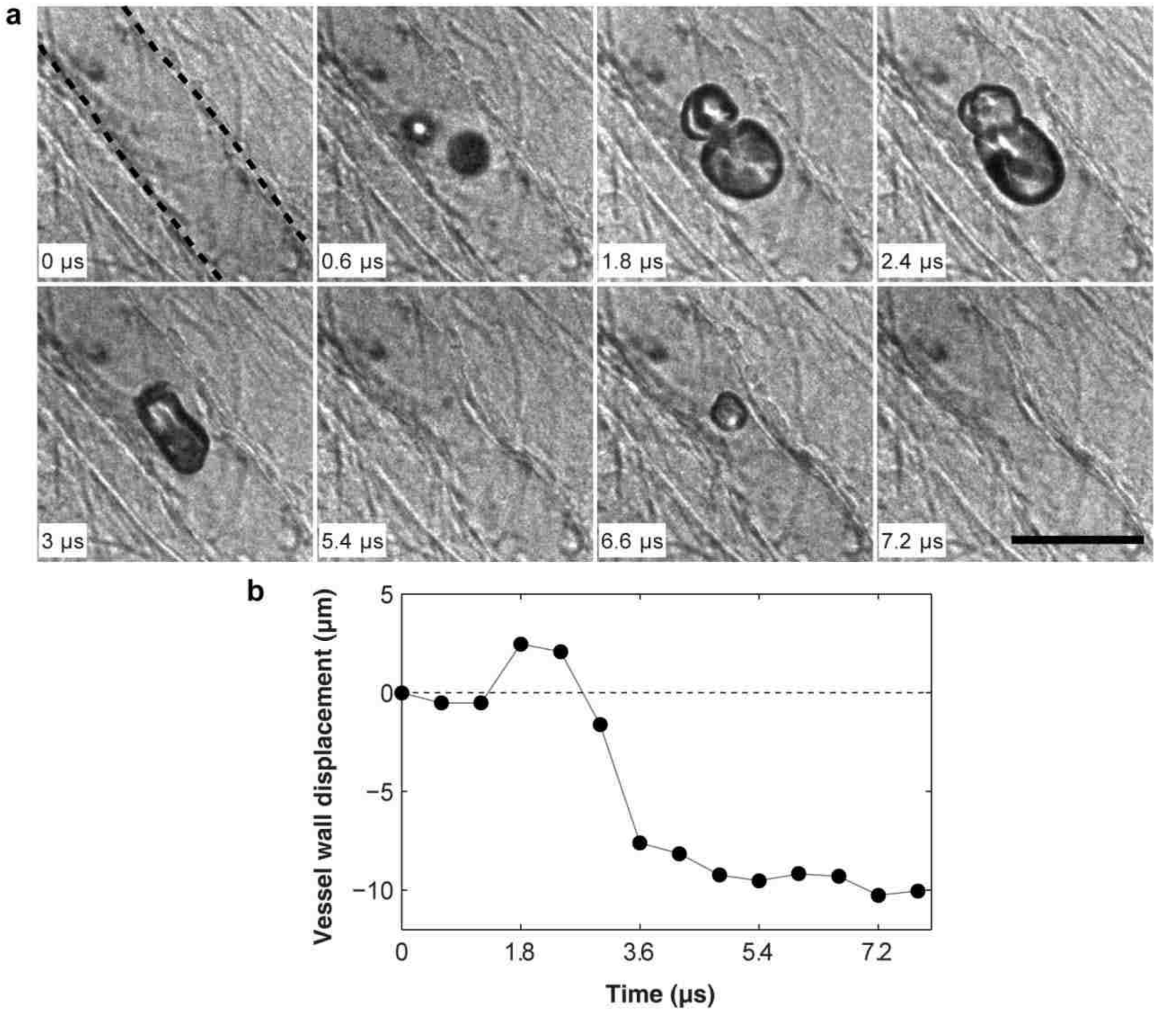

Figure 5.3 Microbubble interaction with a large microvessel. (a) Selected frames from an image sequence which recorded the dynamics of microbubbles in a venule of diameter 35 µm insonated by PNP = 1.5 MPa. The initial location of the vessel wall was highlighted by the dash lines in the first frame. The scale bar represents 50 µm. (b) The displacements of the vessel wall measured at the point on the vessel wall that has the maximum displacement.

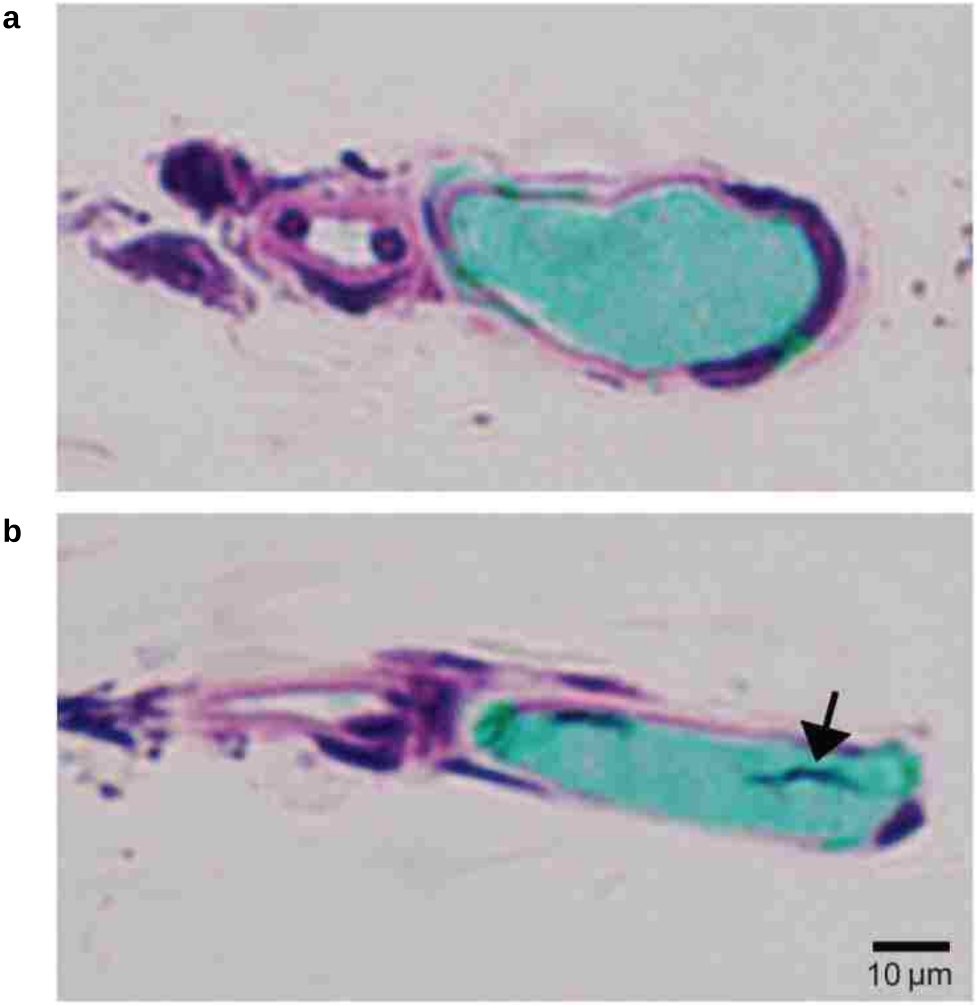

Figure 5.4 Histology results associated with the recorded image sequence shown in Figure 5.3. (a) A vessel section out of the interaction region, showing the vessel section was intact. (b) A vessel section from region that interacted with the recorded microbubbles. The arrow points to dark materials inside the vessel lumen, suggesting that the endothelium was torn away from the vessel wall.

Histology results corresponding to the recorded high-speed image sequence in Figure 5.3 are presented in Figure 5.4. The histology section obtained from the targeted microvessel but out of the bubble-vessel interaction region shows an intact microvessel (Figure 5.4a). Similar intact vessel structure was also found in control sections obtained from vessels not treated by the ultrasound pulses. The green color material inside the vessel is the India ink. Figure 5.4b presents a section from the vessel segment that interacted with the microbubbles, which shows that there was dark material inside the vessel lumen (arrow), suggesting that part of the endothelium was torn away from the vessel wall. The observed endothelial injury corresponded directly to the observed predominant inward vessel movement recorded by the high-speed images. Note that no leakage of the perfused microbubbles or ink is evident.

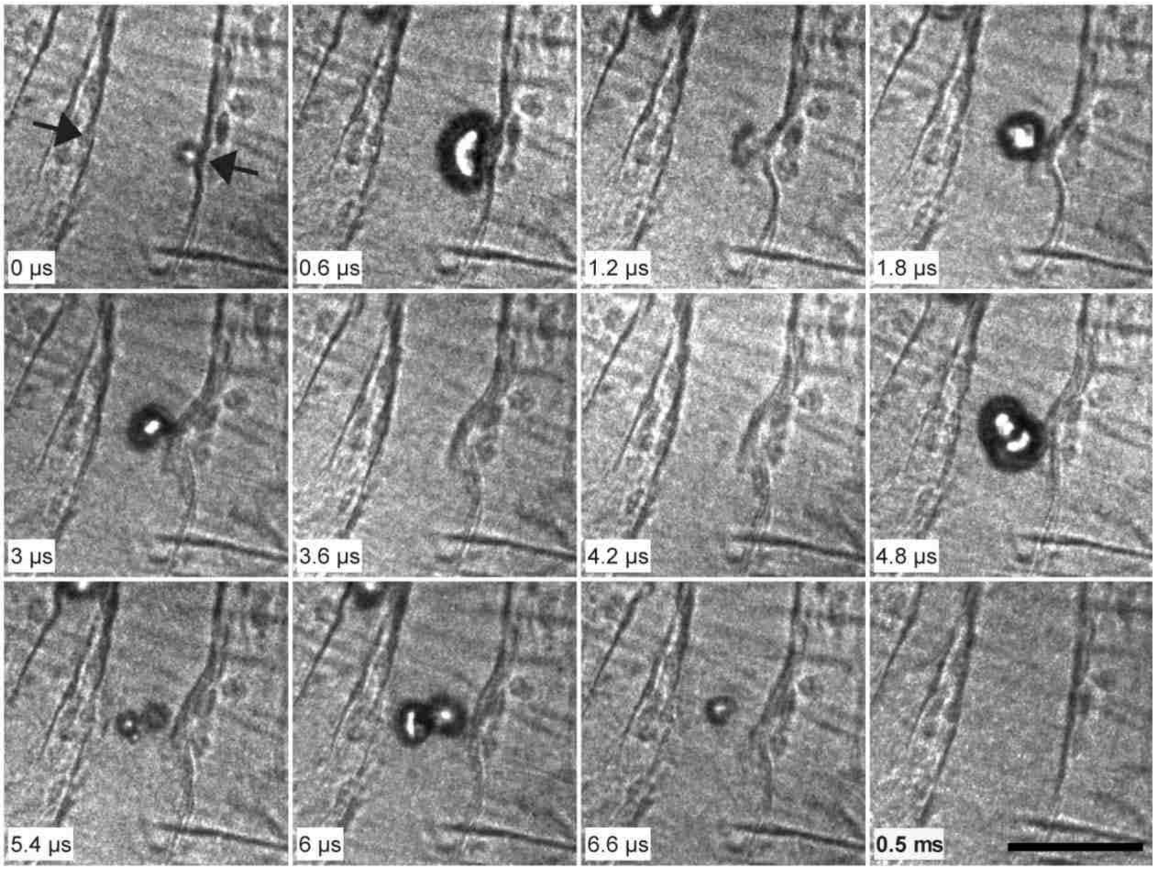

Figure 5.5 Image sequence demonstrating invagination-dominated response of a large microvessel to a cavitation microbubble. D = 40 µm; PNP = 4 MPa. The two arrows in the first frame point out the locations of the two sides of the vessel wall. The scale bar represents 50 µm.

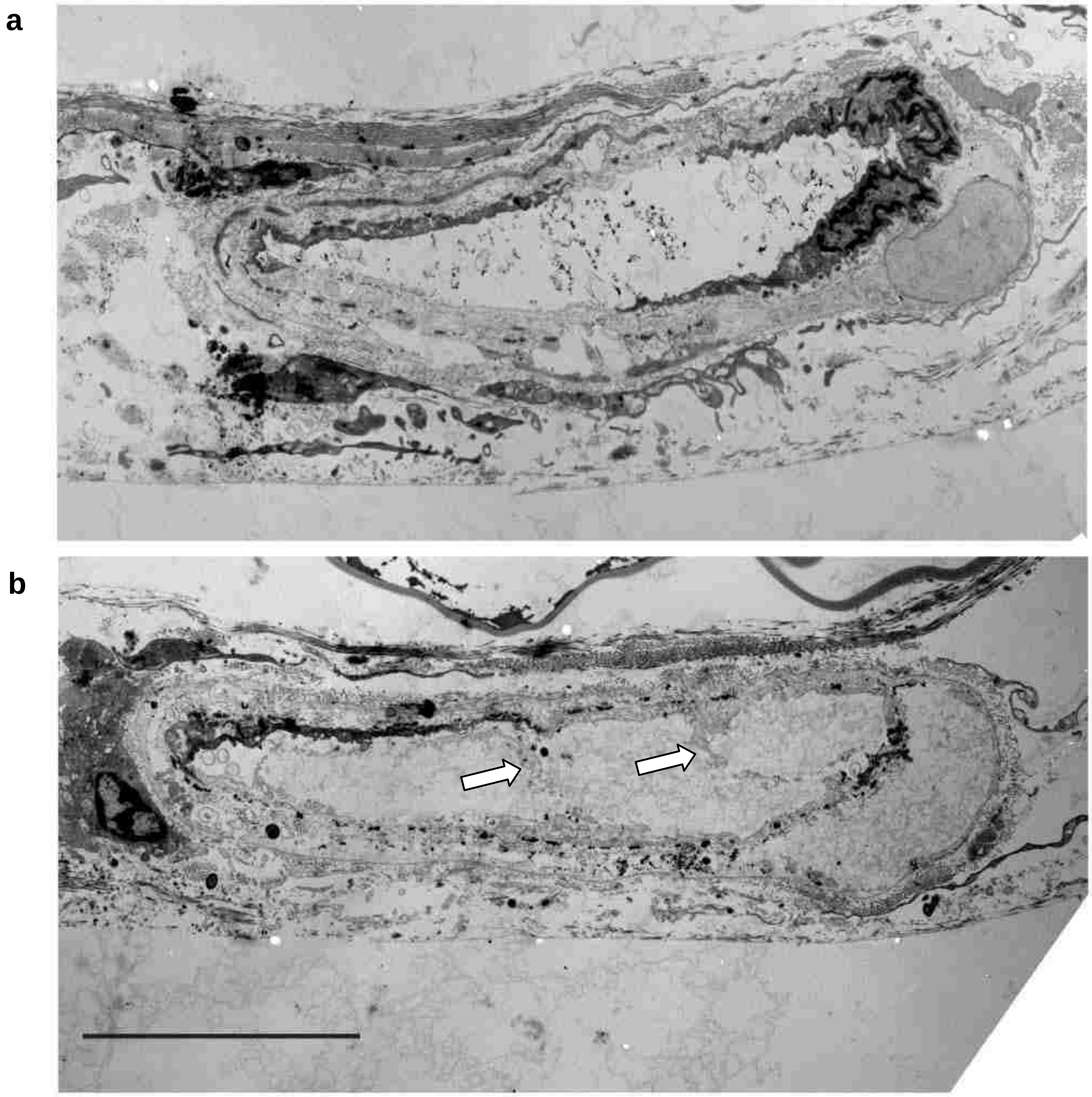

Figure 5.6 TEM results associated with the image sequence shown in Figure 5.5. (a) Control section obtained out of the region that interacted with the microbubble. (b) Section obtained within the region that interacted with the microbubble. The arrows point to locations where damage was obvious. The scale bar represents 10 µm.

Figure 5.5 shows an example of a microbubble interaction with a venule insonated by the ultrasound pulse with PNP = 4 MPa, and the corresponding TEM results are shown in Figure 5.6. This is also a large microvessel case, as $D/2R_{\max} = 3.1$ with D = 40 μm and $2R_{\max}$ = 13 μm as measured from the frame recorded at 0.6 μs. At 0.6 μs, the microbubble expanded and deformed to an approximately hemispherical shape, accompanied by slight distention of the adjacent vessel by 2 μm. The collapse of the microbubble at 1.2 μs was followed by significant inward movement of the vessel wall. Note that similar to the previous example, strong vessel invagination was induced during insonation by the incident wave. The vessel remained invaginated in the following frames (1.8–7.2 μs). The maximum vessel invagination was about 12 μm, which was almost six-fold greater than the maximum distention. At 0.5 ms, a long time after the ultrasound pulse ended, the invaginated vessel appears to have nearly recovered to its initial state, indicating an elastic deformation of the vessel. Note that similar to the case shown in Figure 5.3, fast vessel wall displacements happened during incident pulse insonation (before 4.3 μs); the vessel only moved slightly when exposed to the reflected pulse.

Figure 5.6a shows the TEM image of a control section obtained from a region distant to the microbubble-microvessel interaction region. It shows the structure of an intact vessel. The black particles inside the vessel lumen are green India ink, which appears to have relatively high affinity for electron-dense TEM stain. Figure 5.6b shows a section captured within the region in which vessel deformation was observed. Endothelial cell injury is observed in this section, as indicated by the split of the internal plasma membrane from the vessel wall. This vascular damage pattern is consistent with the histology results shown in Figure 5.4.

In total, seven venules were selected for histology analysis after the high-speed images were captured. Two of them including the example shown in Figure 5.3 presented similar vascular damage as shown in Figure 5.4b. Three venules were selected for TEM analysis after the high-speed images were captured, and two of them showed similar vascular damage as in Figure 5.6b. The damage was observed in several sequential sections, not just one section.

The microvessels involved in the previous two examples were venules. To further explore the microbubble-induced bioeffects to large microvessels, an arteriole of 70 µm in diameter was selected as the targeted microvessel. The arteriole was treated repeatedly by ultrasound pulses with PNP = 7.2 MPa at the presence of microbubbles 20 times at the same region of interest, in order to find out whether the vascular damage pattern would be consistent with previous findings when multiple pulses and a much higher acoustic pressure were used. Each time an ultrasound pulse was sent out, a high-speed image sequence was captured. As the flash lamp required about 2 min for recharging, there was a delay of at least 2 minutes between consecutive ultrasound pulses. Multiple microbubbles appeared up in the captured high-speed images, and obvious vessel deformation was observed in 5 of them when the microbubbles were close to the vessel wall. In these 5 image sequences, invagination larger than distention was observed (images are not shown). In other cases, the microbubbles were close to the center of the vessel lumen and

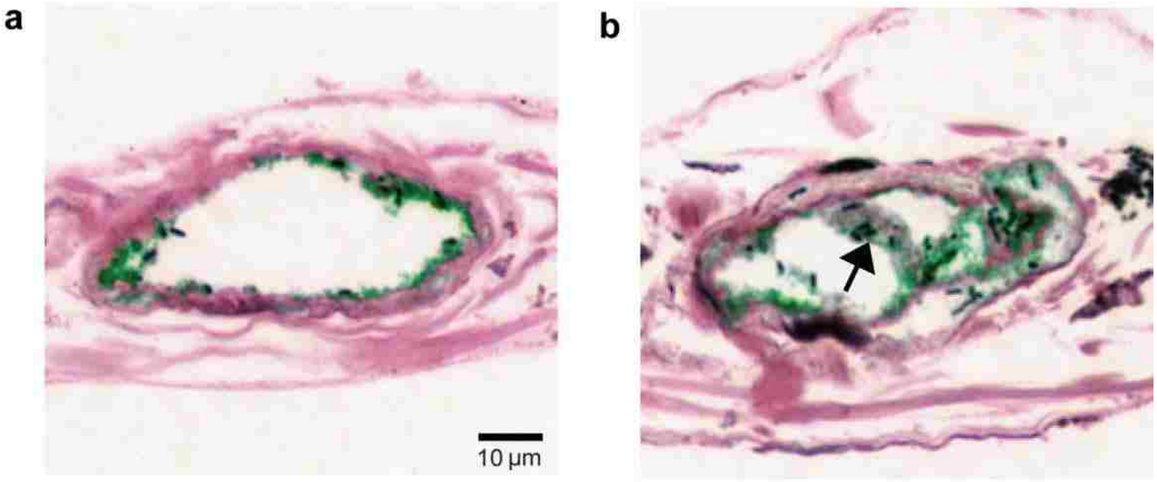

Figure 5.7 Vascular bioeffects found in an arteriole of 70 µm in diameter after exposure to 20 ultrasound pulses with PNP=7.2 MPa with microbubbles presented in the vasculature. (a) Section comes from an untreated region. The green India ink perfused into the vessel appears to have dyed the vessel lining. (b) Section comes from a treated region. It shows that parts of the vessel lining are separated from the rest of the vessel wall. Arrow points to a region of obvious damage.

no obvious vessel deformation was observed. Figure 5.7a shows one histology section from an untreated region as a control; Figure 5.7b shows one section from the treated region. The image of the control section shows a layer lining the interior of the vessel that was dyed green by the India ink. Parts of this green layer are separated from the rest of the vessel wall in Figure 5.7b, suggesting that the lining was physically pulled away from the vessel wall. This vascular damage pattern agreed with that observed in venules (Figures 5.4 and 5.6), although more dramatical vascular damage was observed with repeated treatment at the higher pressure level.

5.3.2 Relatively Small Microvessels

Although most of the microvessels studied were considered to be large microvessels, a few small microvessel cases were studied, in which microvessel distention was significant. In these small microvessel cases, relatively large vessel distention was followed by obvious vessel invagination, but in contrast to the large microvessels the extent of invagination was smaller than distention. Microvessel rupture as indicated by the extravasation of microbubbles was observed. It seems reasonable to conclude that under this condition the structure of the microvessels had been disrupted sufficiently that holes may be formed.

Figure 5.8a shows a single microbubble in a capillary with $D = 7$ μm. Two arrows in the first frame point out the locations of the two sides of the vessel wall. A microbubble appeared visible at 0.3 μs. At 1.2 μs, it expanded against both sides of the vessel wall, reaching the recorded maximum expansion. $R_{\max}$ was about 22 μm, corresponding $D/2R_{\max} = 0.2$, much smaller than 1, thus this vessel was considered to be a small microvessel. The maximum expansion of the microbubble was associated with the maximum distention of vessel with the lower side vessel wall distended by ~8 μm. The microbubble collapsed at 1.5 μs, followed by vessel invagination with the lower side vessel wall moved inward by about 4 μm at the location indicated by the arrow. Although the measured invagination was smaller than the distention, significant vessel deformation was observed associated with vessel invagination, as indicated by the distorted shape of the vessel (see the inset in frame 1.5 μs). The vessel remained invaginated after 1.5 μs (see the frames captured at 1.8 and 3.6 µs). At 1 ms, the vessel recovered, but the vessel diameter measured at the same location as in frame 0 µs was 9 µm, which was larger than its initial diameter (7 µm). The observation that the vessel diameter was even larger than its initial state suggested that plastic deformation of the vessel occurred, implying that the vessel has been damaged. Perfusion of microbubbles was maintained throughout the experiment. After this high-speed image sequence was captured, extravasation of the perfused microbubbles from the lower side of the capillary was observed under the microscope. Figure 5.8b shows an image of the extravasated microbubbles below the capillary recorded using the video camera about two minutes after the high-speed images were captured. It confirmed that the vessel wall was ruptured, and also suggested that the main leakage site was at the lower side vessel wall, where significant vessel distention and invagination were observed in the recorded high-speed images.

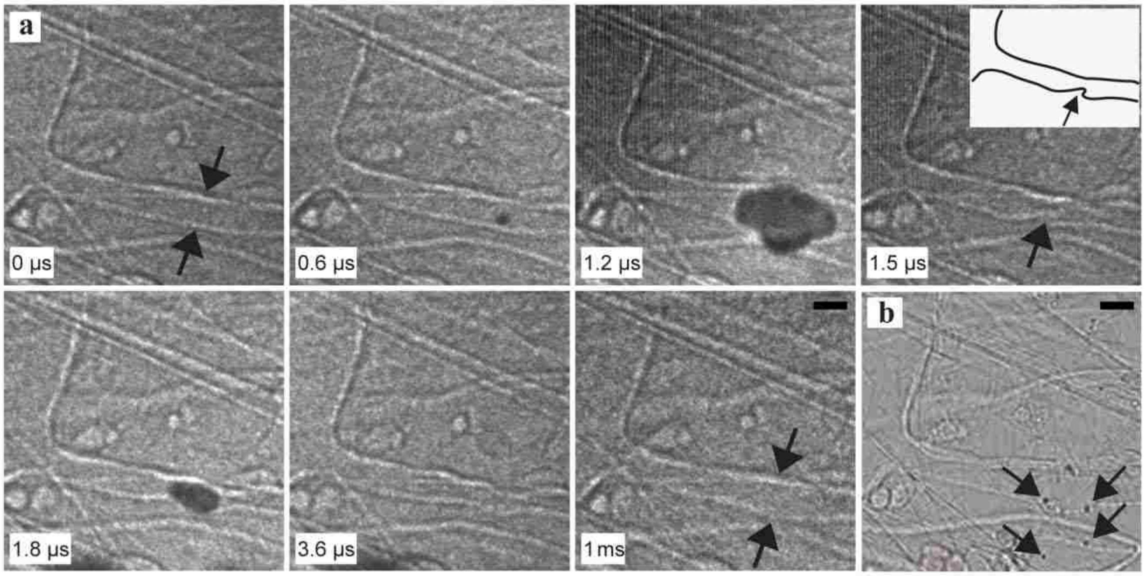

Figure 5.8 (a) Image sequence of a microbubble interaction with a capillary. Two sides of the vessel wall before and after ultrasound exposure are pointed out by the arrows in the frame captured at 0 µs and 1 ms. In frame 1.8 µs, the arrow points to the location that had the most significant deformation, and the inset illustrates the shape of the distorted vessel wall. (b) An image captured 2 minutes after the high-speed images were captured, showing microbubbles (arrows) extravasated from the capillary. Scale bars represent 10 µm.

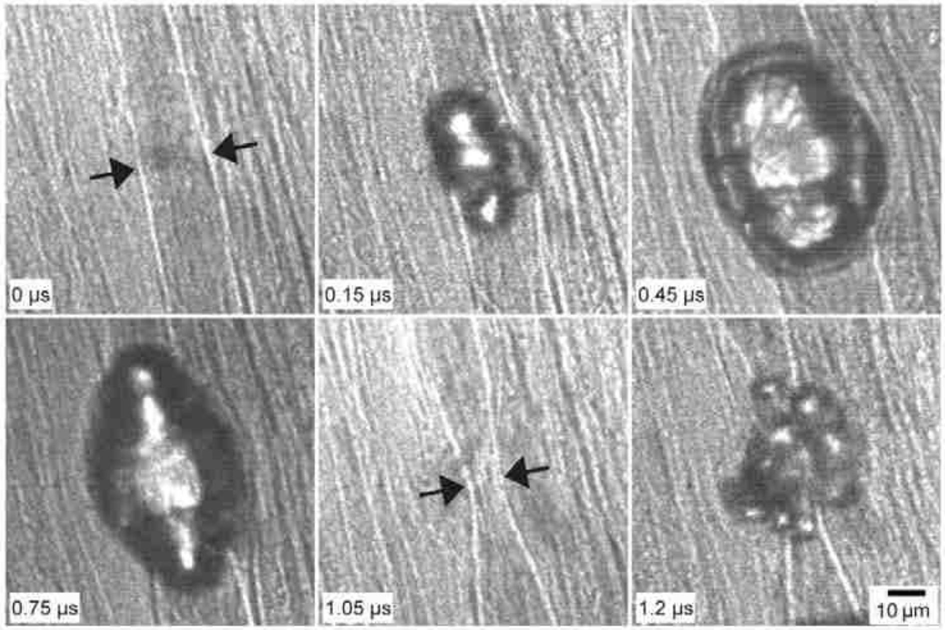

Figure 5.9 Rupture of a small microvessel by a cluster of microbubbles, followed by vessel distention and invagination. D = 17 μm; PNP = 7.2 MPa. The arrows point to the two sides of the vessel wall. The bubble fragments outside the vessel at 1.2 μs indicate that the vessel had been ruptured.

The second case is shown in Figure 5.9, recorded the interaction of multiple microbubbles with a venule of D = 17 μm insonated by an ultrasound pulse with PNP = 7.2 MPa. The inter-frame time for this specific case was set to 150 ns. Both sides of the vessel wall were highlighted manually using Matlab to make it easier for the reader to identify. The highlighting operation was done only to this image sequence as the fibers surrounding the microvessel can easily be confused with the vessel walls. A cluster of microbubbles was visible in the microvessel at 0.15 μs. At 0.45 μs, they expanded against the vessel wall and reached the maximum recorded expansion with $R_{\max}$ = 26 μm, and each side of the vessel wall achieved a maximum distention of ~14 μm. The bubble cluster then contracted (0.75 μs) and collapsed (1.05 μs). At 1.05 μs, microbubble collapse was accompanied by almost symmetrical vessel invagination, with each side of the vessel wall moved inward by about 5 μm relative to its initial position. In frame 1.2 μs, several re-expanding bubble fragments have clearly been extravasated from the vessel, indicating that the vessel was ruptured.

5.4 Discussion

Microbubble-induced deformation of the microvessels in *ex vivo* rat mesenteries, and the corresponding vascular bioeffects were studied in this work. Damage of large microvessels was associated with the predominantly inward vessel wall movements as found in histology and TEM analyses. Damage was characterized by the separation of part of the endothelium from the vessel wall. In a limited number of studies including small microvessels, damage was associated with vessel rupture following significant vessel distention and invagination.

5.4.1 Damage of Large Microvessels

A previous study of laser-induced cavitation bubbles near a compliant boundary by Brujan *et al.* (Brujan *et al.*, 2001b) showed that an expanding bubble pushed against the boundary causing indentation on the boundary, and the collapse of the bubble could develop a low-pressure region between the collapsing bubble and the boundary, leading to the uplifting of the boundary. The tensile-stress induced uplifting of the boundary was considered as one potential mechanism responsible for cavitation induced damage of biological tissues.

Similarly, the present study demonstrated that microvessels were pushed outward during microbubble expansion, and were pulled inward during microbubble collapse, with the inward movement typically exceeding the outward movement. The associated damage of large microvessels was characterized by the separation of the endothelium from the rest of the vessel wall, which cannot be explained by vessel dilation alone which pushes the vessel wall against the surrounding tissue. It is consistent with damage caused by tensile stresses at the vessel walls that lead to vessel invagination. Therefore, the present observations are consistent with the concept that invagination plays a dominant role in causing damage to large microvessels.

The damage pattern observed in large microvessels was consistent with several previous reports. Stieger *et al.* (Stieger *et al.*, 2007) reported the separation of endothelial layer from underlying pericytes in TEM images of chorioallantoic membrane tissue after being treated by ultrasound at a center frequency of 1 MHz and PNP of 2.3 MPa, applied in 10-cycle pulses at a pulse repetition frequency of 500 Hz for 5 seconds. Zachary *et al.* (Zachary *et al.*, 2006) performed histology studies of microbubble-induced bioeffects to auricular artery at PNP = 9.5 MPa (MI = 4.4) for a treatment period of 30 min and found vascular damage with similar characteristics: the tunica intima was lifted off of the internal elastic lamina.

5.4.2 Damage of Small Microvessels

Based on the study of Zhong *et al.* (Zhong *et al.*, 2001), vessel distention generated by the expansion of a microbubble beyond the diameter of the vessel has been proposed as an important mechanism for microvessel damage. Using a simplified model, Zhong *et al.* predicted that the energy carried by the expanding bubble at the moment of contacting the vessel wall would be higher in a small vessel than in a large one, and would be higher at a higher PNP than a lower one as $R_{\max}$ increases when PNP increases. In the present work, it was a consistent observation that in a capillary (Figure 5.8) or under very high pressure conditions (Figure 5.9), the expanding microbubble could induce significant vessel distention. However, vessel invagination following distention was not observed by Zhong *et al.* The reason may be that the hollow fibers they used as vessel phantom had different mechanical properties as those of the microvessels.

Although it involved a laser-induced cavitation bubble, vessel distention followed by invagination has been observed in a dissected rabbit femoral artery (Van Leeuwen *et al.*, 1993). It was found that the bubble expanded to a size much larger than the vessel diameter, reaching a maximum dilation ratio (expanded vessel diameter/initial vessel diameter) of 1.5, which was followed by slight invagination (deduced from the recorded images, the invagination ratio defined by invaginated vessel diameter/initial vessel diameter was 0.9) associated with the collapse of the bubble. Subsequent histological analysis found abrasion of the internal elastic lamina, which according to the authors cannot be explained by dilation alone, because balloon dilation in the femoral artery of the rabbit with dilation ratios up to 2.0 did not cause any abrasion of the internal elastic lamina. They hypothesize that the abrasion is due to the sequential insult of dilation and invagination. In the present study of microbubbles in small microvessels, similar vessel dynamics were observed, with the difference that microvessel invagination induced by microbubble collapse was more significant. The invagination ratio was about 0.4 for the two cases shown in Figure 5.8 and 5.9. Moreover, based on the shape of the vessel wall, it appears that localized high strain on the vessel wall may be associated with vessel invagination. Accordingly, it is here proposed that in small microvessels, vessel distention becomes more significant than in large ones, but vessel invagination also contributes to the vascular damage.

5.5 Summary

The interactions of microbubbles with microvessels was observed using ultra-high speed photomicrography, and the correlation of the observed interactions and resulting vascular bioeffects was demonstrated by either histology and TEM analyses or the extravasation of microbubbles. Endothelial cell damage revealed by the histology and TEM analyses was associated with the invagination-dominated vessel response in large microvessels, whose diameters were larger than those of the maximally expanded microbubbles. In small microvessels, where the microbubbles expanded to much larger sizes than the initial vessel diameters, vessel rupture indicated by microbubble extravasation was observed when significant vessel distention followed by invagination was observed. While the prevailing paradigm proposes that microbubbles damage vessels by distending them, the present studies suggest strongly that vessel invagination is a mechanism by which acoustically activated microbubble-induced vascular damage arises, and may be the dominant mechanism for the damage of large microvessels.

The finding that microbubbles could cause vascular damage supports the idea of using microbubbles to increase vascular permeability, as the microbubbles could weaken the barrier to the passage of medications through or into the endothelial cells. It also suggests that for the safe applications of microbubbles this damaging effect should be avoided. Systematic studies of the parameter dependence of this vascular damage mechanism are needed in the future. In addition, notice that in the histology and TEM images, the vessels were partially collapsed. To better preserve the vessels, perfusion fixation can be used in the future to fix the tissue immediately after the high-speed images were taken.

Chapter 6

Relaxation of Microvessels Deformed by Microbubbles

6.1 Introduction

The expanding applications of microbubbles in both diagnostic and therapeutic ultrasound have led to an increasing interest in both experimental and modeling studies of microbubble dynamics in blood vessels. On the experimental studies side, a better understanding of the experimental results requires knowledge of the mechanical properties of the microvessels. On the modeling side, although several models have been developed to solve the complex coupled dynamic problem of microbubble interaction with microvessels, most of the models considered only the stiffness of the microvessels, with the vessel simplified as, for example, rigid tubes (Oguz & Prosperetti, 1998; Sassaroli & Hynynen, 2004), elastic deformable tubes (Miao *et al.*, 2008; Miao & Gracewski, 2008; Qin *et al.*, 2006; Sassaroli & Hynynen, 2005; Ye & Bull, 2006), or two rigid parallel plates (Cui *et al.*, 2006). Using a simplified geometry for the couple bubble-vessel system, Freund (Freund, 2008) developed a model that considered both the elasticity and viscosity of the vessels connected with surrounding tissue, and concluded that viscosity played a significant role in bubble dynamics. For the development of better models, information about the viscoelastic properties of the microvessels is needed. The primary motivation of the study presented in this chapter was to estimate the mechanical parameters of the microvessels in the rat mesentery to provide insight into the experimental results and references for the modeling.

Most biological tissues, among which vascular tissue is included, exhibit a time-dependent stress-strain behavior that is characteristic of viscoelastic materials. In contrast to the relatively abundant data on the mechanical properties of larger vessels (arteries and veins), there are few studies on the viscoelastic properties of microvessels. These latter have been performed mainly to investigate the static pressure-diameter relationships of microvessels, resulting in a reasonable understanding of the purely elastic properties of microvessels. Examples include the Young's modulus of arterioles in frog mesentery, which was reported to be 60 kPa , and the Young's moduli of capillaries and venules in cat mesentery, which were reported to be 10 kPa and 32 kPa, respectively (Swayne *et al.*, 1989). Although the viscous properties have been well recognized, relative little effort has been devoted to elucidate the time-dependent viscoelastic properties. The scarcity of such studies most likely stems from the difficulty of applying conventional techniques, due to mainly their small sizes and hard-to-access nature.

The conventional approach to probe the viscoelastic properties of materials is to measure material motion caused by an external loading that consists of a stress-relaxation or creep test. Soft tissues are often discussed in the framework of the linear theory of viscoelasticity relating stress and strain on the basis of the Voigt, Maxwell, or Kelvin models, which consist of elastic springs and viscous dashpots. Based on these models, the characteristic relaxation time constants of the tested processes can be derived as indicator of the time-dependent viscoelastic properties of the tissues. Static excitation, quasi-static (<10 Hz) force, and ultrasound have been used as external stimulation to study bulk tissue viscoelastic properties, and the lowest time constant reported was at millisecond time scales (Girnyk *et al.*, 2006).

In this chapter, a microbubble-based method was developed to assess the viscoelastic properties of microvessels in the *ex vivo* rat mesentery. In Chapter 4, it was found that microbubbles excited by short ultrasound pulses can induce sudden deformation of the adjacent vessel wall on microsecond temporal scales, which suggests that ultrasound-activated microbubbles may be used as motors to drive the microvessels to deform. Here, the relaxation time courses of the deformed microvessels induced by the microbubbles were recorded. The recorded vessel relaxation processes were analyzed in terms of a Voigt model, consisting of a spring connected in parallel with a dashpot. The relaxation time constants were derived based on this model. The time constants can be used to infer the ratios of elasticity to viscosity of the microvessels connected with surround tissue.

6.2 Methods

6.2.1 Animal Tissue Preparation

Animal tissue preparation followed the methods described in Section 2.2. Venules were selected for this study, as they were easier to be deformed by the microbubbles than arterioles, and easier to find in the prepared tissue samples than capillaries. Note that a syringe pump was used to control the perfusion of the microbubbles into the microvessels. The speed of the pump could be varied to change the flow speed inside the vessels.

6.2.2 Ultra-high Speed Imaging

The same experimental setup and ultra-high speed imaging methods described in Section 2.3 were used here, with the only change being in the camera timing. In each experiment, after a targeted microvessel was selected, the ultra-high speed camera was triggered to capture images of the microvessel before, during and after the single ultrasound pulse exposure with the presence of the microbubbles in the vasculature. The camera could potentially capture 14 frames at each trigger event; however, due to malfunction, 2 frames were not available at the time when this study was performed, therefore only 12 frames were captured each time. The 12 frames were typically set up as follows: frame 1 was captured before the ultrasound pulse arrived at the tissue sample to record the microvessel at its initial state; frames 2–3 were captured during ultrasound exposure; frames 4–11 were captured after ultrasound exposure to record the recovery process of the deformed microvessels, and frame 12 was obtained at a long delay time with the intention of capturing the microvessel after it had recovered to its initial state or nearly so. An example of the camera timing setup is illustrated in Figure 6.1. Note that extensive studies of the bubble-vessel interaction dynamics during ultrasound exposure were performed before as reported in Chapters 4–5, which was not the focus of the present study. Thus, only 2 or 3 frames were captured during ultrasound exposure to provide reference information about the dynamics of the microbubbles and microvessels during insonation.

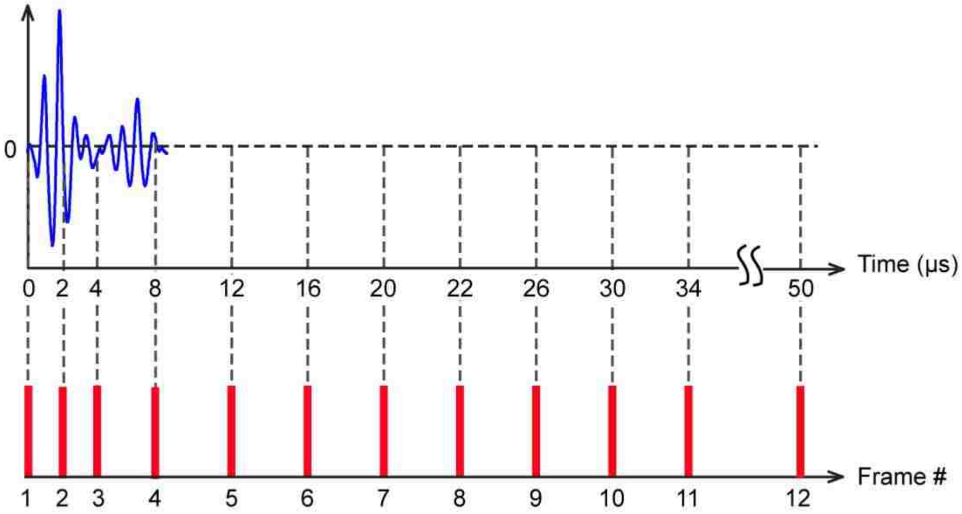

Figure 6.1 Illustration of the system timing. The upper panel represents the ultrasound wave. The lower panel shows the timing for the ultra-high speed camera.

6.2.3 Image Analysis

As noted previously, there was jitter among the recorded image frames. To reduce the measurement uncertainty associated with the camera jitter, the vessel wall displacements were quantified by the diameter changes of the microvessels at the location that had the maximum displacements in reference to their initial diameters. Each relaxation process was considered to start from the time point t_0, when the recorded vessel displacements reached their maximum value $D_{\max}$. It was considered to end when the vessel displacements were close to zero.

6.2.4 Estimation of the Relaxation Time Constants

The recorded image sequences that satisfied the following two criteria were selected for estimation of the relaxation time constants: (1) $D_{\max} > 3$ μm, which was about the upper limit of the measurement uncertainty; and (2) there were more than three frames recorded during the vessel relaxation process.

As a first approximation, the microvessels connected with surrounding tissue were represented by a standard Voigt model consisting of an elastic spring and a viscous dashpot in parallel (Figure 6.2).

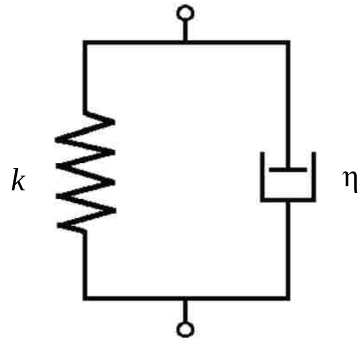

Figure 6.2 Schematic representation of a Voigt model.

The governing equation for this model during the relaxation process is

$$D = D_{\max} \exp[-(t - t_0)/\tau], \quad 6.1$$

$$\tau = \eta / k, \quad 6.2$$

where D is the vessel displacement, t_0 is the time point when the recorded vessel displacements reach their maximum value $D_{\max}$, τ is the relaxation time constant, k is the elastic constant, and η is the viscous coefficient. The time constant was given by the ratio of the viscous coefficient to the spring constant. This time constant was determined by fitting the experimental data with a single time constant exponential decay using a program based on Matlab's built-in FMINSEARCH function, which performs an unconstrained nonlinear minimization of the sum of squared residuals with respect to the various parameters. Student's t-test was used to determine whether there is a significant statistical difference ($P < 0.05$) in the time constants among different groups.

6.3 Results

Figure 6.3a shows the dynamics of a relatively small microvessel with an initial diameter of 30 µm. Frame 1 recorded the vessel at its initial state, before the arrival of the ultrasound pulse. Frame 2 shows a microbubble oscillating in the microvessel, which was accompanied by the invagination of both sides of the vessel wall. At 11 µs, when the vibrating microbubble and ultrasound field were absent, almost axial-symmetrical vessel invagination was recorded and the vessel displacements reached its recorded maximum $D_{\max}$. The recovery of the invaginated vessel is shown in the representative frames captured at 20 and 48 µs. At 48 µs, both sides of the vessel wall had returned to nearly their initial positions.

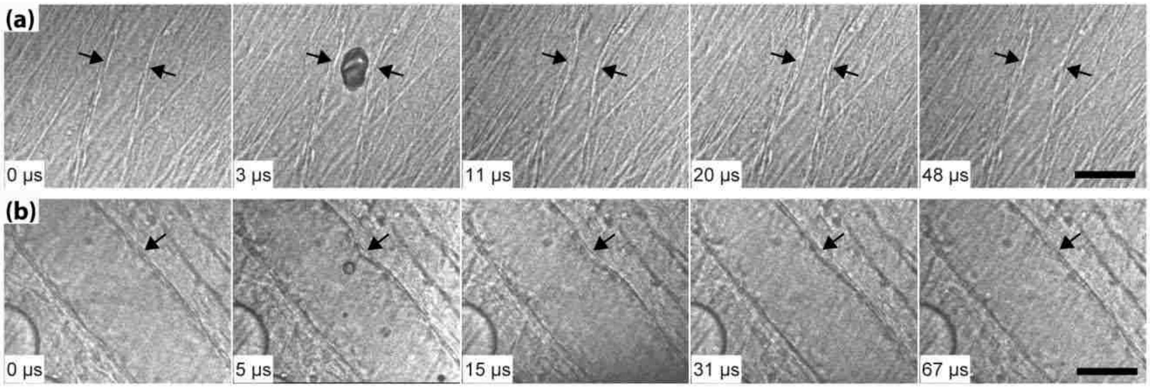

Figure 6.3 Representative image sequences to show the invagination and recovery of the microvessels. (a) Vessel diameter = 30 µm; PNP = 1.5 MPa. (b) Vessel diameter = 76 µm; PNP = 2.8 MPa. Scale bars represent 50 µm. The arrows point out the locations of the vessel wall.

Figure 6.3b shows the dynamics of a relatively large microvessel with a diameter of 76 µm. A microbubble (arrow) was visible near the vessel wall in frame 2 captured during ultrasound exposure, and localized vessel invagination was observed on the right side vessel wall. The displacement reached its recorded maximum at 15 µs. The relaxation process of the vessel wall is shown in representative frames 4 and 5. In this case, the vessel dynamics were similar to those shown in Figure 6.3a, with the difference being that in this relatively large microvessel, significant vessel deformations were only observed on one side of the vessel.

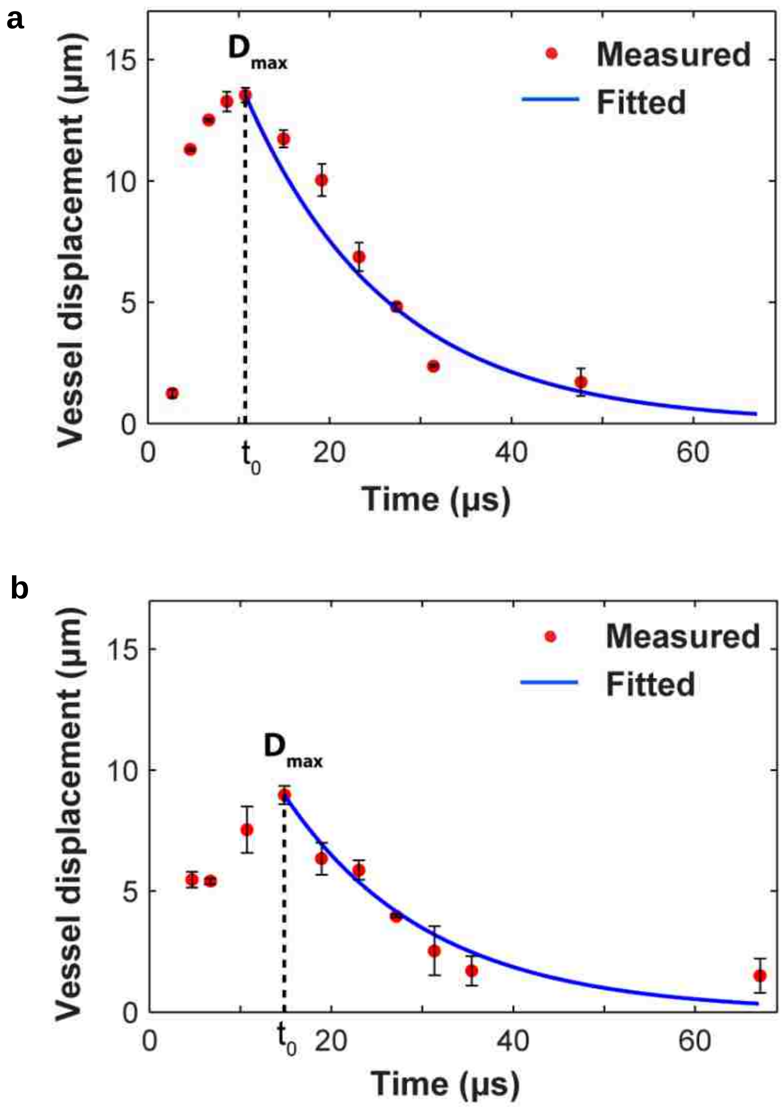

Figure 6.4 Vessel wall displacements as a function of time, corresponding to the image sequences shown in Figures 6.3a and 6.3b, respectively. The solid curve is the best fit to the data using the Voigt model. The error bars are standard errors of the measurements.

Figure 6.4 gives the displacements of the microvessels recorded in Figure 6.3. The time t_0, when the displacement reached its maximum $D_{\max}$, is marked by the dashed line. For the small microvessel case (Figure 6.4a), t_0 = 11 μs and $D_{\max}$ = 14 μm; for the large microvessel case (Figure 6.4b), t_0 = 15 μs and $D_{\max}$ = 9 μm. Lower estimations of the average speed of vessel deformation using $D_{\max} / t_o$ gave 1.3 m/s and 0.6 m/s for the two cases, respectively. The relaxation processes were fitted to the Voigt model. For both cases, the time constant was τ =15 μs, and the correlation coefficients of the fits were R = 0.96 and 0.97, respectively. This small time constant indicates a higher rate of changes in displacements and smaller viscous force relative to elastic restoring force.

A summary of the obtained data is shown in Figure 6.5. It shows that the estimated time constants (including the two shown in Figure 6.3) ranged from 3 to 24 μs. Moreover, almost all the correlation coefficients R of the Voigt model to the experimental data were larger than 0.8. Generally, a correlation greater than 0.8 is described as strong, whereas a correlation less than 0.5 is described as weak (Roberts & Roberts, 2011). Therefore, there were strong correlations between the experimental data and the Voigt model, suggesting that the simple Voigt model is sufficient to describe the experimental results.

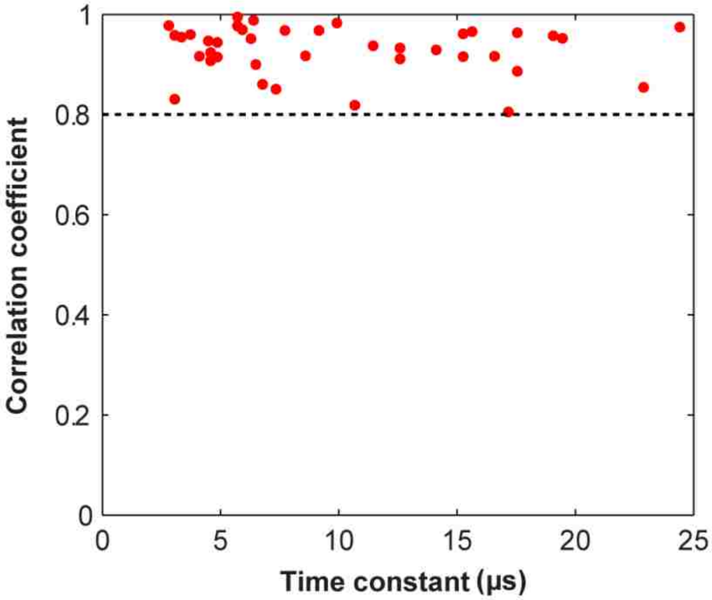

Figure 6.5 Summary of the measured correlation coefficient and time constants for 38 data.

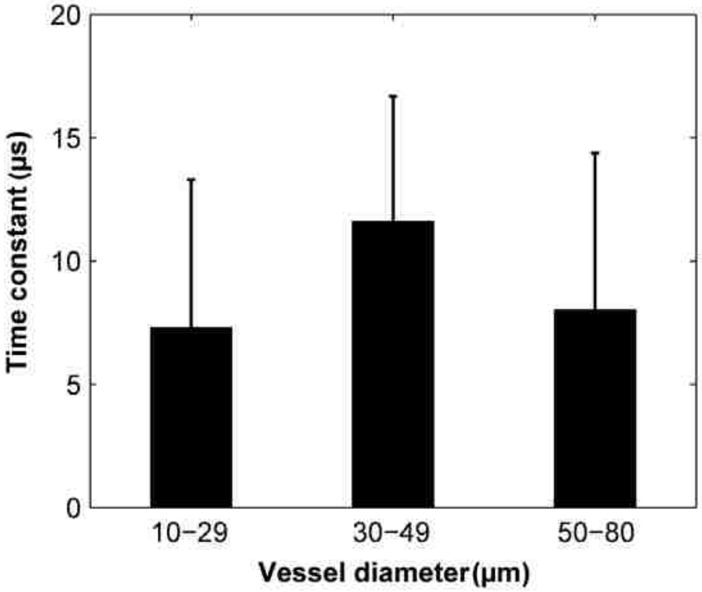

Figure 6.6 Relaxation time constants estimated for microvessels with different diameters. The error bars are standard errors of the measurements.

Figure 6.6 shows the time constants with respect to the vessel initial diameters for the same data set shown in Figure 6.5. The data were divided to three groups based on the initial vessel diameters: 10–29, 30–49, and 50–80 μm. The mean of each group was shown in this figure with the error bar stands for the standard deviation. For the three groups, the means of τ were 7, 12 and 8 μs, respectively. Within the accuracy of our measurements, the time constants of the three groups are not significantly different, suggesting that the mechanical properties of these microvessels may be similar. The scatter of the τ might be mainly caused by the variation in vessel and surrounding tissue structures within each group and the limited image frames captured during vessel relaxation.

Previous studies of the static elastic properties of microvessels found that the microvessels become stiffer and the effective Young's modulus increases as the strain increases (Caro *et al.*, 1978). In the present study, the microbubbles were injected into the microvessels under the control of a syringe pump. By changing the syringe pump speeds, the perfusion pressure changes, thereby the extent of vessel distention was changed. Figure 6.7 gives an example of the measured vessel diameters as a function of the syringe pump speeds. The vessel diameter measured at 90 ml/h was arbitrarily used to normalize the measured vessel diameters. The vessel was extended 15% more when the pump speed increased from 10 to 50 ml/h. The data presented here demonstrated the trend that the vessel was extended more at higher pump speeds. Note that Figure 6.7 is just one example to qualitatively show the effect of the syringe pump speeds on the extend of vessel distention.

To find out the effect of the syringe pump speeds on the relaxation time constants, two different pump speeds were tested. All the data presented previously were acquired when the syringe pump speed was set to 50 ml/h. More experiment was carried out with the pump speed set to 10 ml/h. A summary of the measured relaxation time constants corresponding to the two pump speeds for vessels with initial diameters within the range of 20–40 μm is presented in Figure 6.7b. This figure shows that there is a reduction in the time constant when the pump speed increases. The mean of τ at the low pump speed was 26 μs, and at the high pump speed was 10 μs. Moreover, they are statistically different from each other, suggesting that τ depends on the syringe pump speeds.

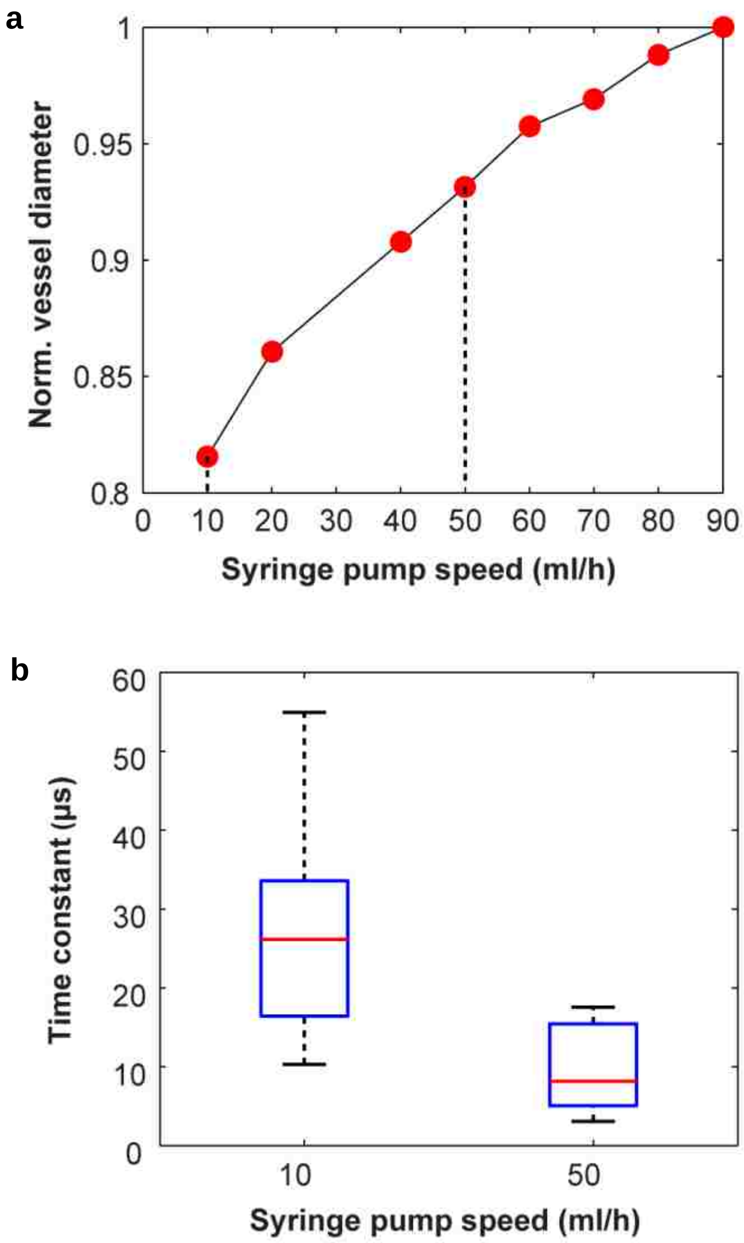

Figure 6.7 (a) An example of the measured vessel diameters with respect to the syringe pump speeds. The vessel diameter measured at 90 ml/h was arbitrarily used to normalize the measured vessel diameters. (b) Time constants estimated for vessels with initial diameters within the range of 20–40 µm with perfusion speeds of 10 or 50 ml/h, respectively.

6.4 Discussion

6.4.1 Scales of the Relaxation Time Constants

We used ultrasound-activated microbubbles to induce displacements of the venules in the *ex vivo* rat mesentery, and derived the relaxation time constants of the venules to be at the order of microseconds. Although there are differences among venules, arterioles, and capillaries in the vessel composition and structure, their static elastic modulus are in the same order. The reported Young's modulus of the three types of microvessels in the mesentery were all at the scale of 10 kPa (Swayne *et al.*, 1989). Accordingly, it was expected that the relaxation time constants for capillaries and arteries would be of a time scale similar to that of the venules. Meanwhile, when the pump speed decreased from 50 to 10 ml/h, the mean of τ increased by a factor of ~3. Previous studies on the arterioles of the frog mesentery have indicated that when measured at a diameter of 15% above resting diameter at zero transmural pressure the incremental Young's modulus was 60 kPa, and it rose to 120 kPa at 45% distention. Accordingly, the changes in the measured τ at different pump speeds may be explained by the variation in the effective Young's modulus with the strain on the vessel. However, the time scales of τ remained to be at microseconds. It needs to stress that as the estimation of τ depends on the vessel types and the experimental techniques, the results obtained in the present study are probably accurate to an order of magnitude approximation.

The time scales of τ estimated in this study were several orders of magnitude lower than previous measurements of bulk tissues, despite differences in measurement methods, the types of tissue measured, and different viscoelastic models used to describe data. The method developed here differs from previous ones mainly in that the microvessels were deformed on a microsecond time scale by the cavitation microbubbles, while in all previous measurements of the relaxation time constants, the tissue movements were at time scales several orders of magnitude longer than that. Only in shear wave measurements at megahertz frequency did the tissue reach the deformation rates of these microbubble-excited microvessels, although the tissue displacements by the shear waves are expected to be significantly different from the vessel deformation by the microbubbles. Moreover, tissue properties were measured indirectly based on the shear wave dynamics. Nevertheless, these shear wave measurements provide some references in analyzing the problem of concern here. Deduced via the small fast deformations of dissipating megahertz ultrasonic shear waves in bulk tissues, the viscosity and elasticity of cardiac muscles were reported to have orders of magnitude of 0.1 $Pa \cdot s$ and 100 kPa, respectively (Madsen *et al.*, 1983). Accordingly, by dividing the viscosity by the elasticity, the relaxation time constant of the muscles at megahertz deformation rates is estimated to be on the order of microseconds. Although the bulk mechanical properties of muscles are doubtlessly different from the microvessels in the rat mesentery, the available data from muscles suggest that at megahertz frequencies the relaxation time constants could reach a microsecond time scale. Previous studies indicated that tissue elasticity may not be frequency dependent, but there was strong evidence that the tissue viscosity decreased as frequency increased. It was reported that the viscosity of venules at megahertz frequencies was orders of magnitude lower than those reported at very low or zero frequency (Phan-

Thien *et al.*, 2000). Therefore, I propose that the microsecond-level time constants were mainly associated with the reduction of tissue viscosity at megahertz deformation rates.

Direct knowledge of viscosity and elasticity would be ideal, but current knowledge of tissue parameters is so poor that the ratio itself can help constrain possible values. These values can provide important input to the modeling studies in selecting the parameters. For example, if we assume the elasticity of the microvessels in the rat mesentery at megahertz deformation rates remains at the same order of magnitude as measured in static state, the elasticity of these microvessels would be at the scale of 10 kPa. Then the microsecond relaxation time constants suggested that the viscosity coefficient of the microvessels was at the order of 0.01 $Pa \cdot s$.

6.4.2 Implications of the Findings

The relaxation time constants provide the ratio between the viscosity coefficient and elastic constant. Although it does not characterize quantitatively the values of the elasticity and viscosity, it can be used in conjunction with the experimental results reported in the previous chapters for a better understanding of the microbubble dynamics in microvessels.

In Chapter 4, it was presented that microbubble oscillation induced vessel wall displacements on microsecond time scales. This indicates that during the very rapid collapse of the microbubbles, the vessel moved at almost the same time scale as the forced microbubble oscillation. The flexible vessel with surrounding tissue can extract energy from the fluid motion that may be dissipated within the tissue or returned to the fluid motion sometime later, depending on the characteristic times of the tissue motion (Blake

& Gibson, 1987). The very short time scales determined in this study suggest that the energy stored in the tissue during the expansion phase of the microbubbles can be 'injected' back into the liquid during microbubble collapse. Otherwise, if the time constant were larger, say at a millisecond time scale, one would not expect the microvessels to respond as quickly as observed. Under the latter condition, to compensate for the volume changes of the microbubbles during collapse, the flow would move toward the collapsing microbubble at high velocity while the vessel walls would move slightly. To extend this analysis further, the primary damage to the vessel would then arise as a consequence of the viscous interactions of the blood with the endothelium, rather than of strains in the vessel walls. This hypothetical scenario is not consistent with observations presented in Chapter 5, which demonstrated that microvessel damage was associated with vessel deformation.

6.4.3 Limitations of This Work

Whereas the study of the mesenteric microvessels *ex vivo* permits some physiological conditions to be maintained experimentally, there were several limitations of this work.

It is known that the Young's modulus of a soft tissue depends on the stress in the tissue. This points out an important variable that should be controlled; that is, the level of static strains applied to the prepared tissue samples. The extent of how much the tissue was stretched when applying the tissue holders was not controlled. But, during the experiment care was taken not to stretch the tissue more than appeared to be the case *in situ* while applying the clamping devices.

Clearly, this work was performed on *ex vivo* tissue samples. Another potentially important variable that was not investigated is the effect of cell death and autolysis that inevitably occurred in the time between specimen harvesting and measurements. Hence, longitudinal studies are needed to establish the time window, if any, during which the mechanical properties of specimens approximate those of tissues *in vivo*. Meanwhile, the relaxation time constants may vary at high strains because of vessel damage. The $D_{\max}$ measured from the data presented in this work ranged from 3–24 μm, and there was no pronounced influence of $D_{\max}$ on τ, suggesting that the extent of vessel displacements, of concern to this study, did not lead to changes of τ.

Furthermore, the tissue was modeled as a 1-D spring-dashpot system. This is a relatively unsophisticated model for the vessels and surrounding tissue. Extending the 1-D model to 3-D model would be a non-trivial task. That understood, this simple approximate model is clearly a reasonable start for investigating vessel viscoelasticity, especially considering the strong fit of this model to the experimental data.

In addition to the above limitations, the fact that all the experimental studies of microvessels need to use a microscope limited the study to nearly transparent tissues. The mechanical properties of microvessels in other tissues, say muscles, may be different from the microvessels in rat mesenteries. The data obtained from this study added to a base set of biomechanical data on microvessels in the rat mesentery and provided a reference state for comparison to other tissues.

6.5 Summary

The relaxation time courses of microvessels deformed by ultrasound-activated microbubble were recorded. A Voigt model of tissue (parallel spring and dashpot) was used to fit the relaxation processes. The relaxation time constants τ was derived based on this model. The Voigt model fit the data well. The estimated τ ranged from 3 to 24 μs. No significant difference was found in τ for microvessels with diameters within the range of 10–80 μm. However, statistically significant variations were shown to occur by changing the speeds of the syringe pump that were used to perfuse the microvessels. The estimates of τ determined here are probably accurate to an order of magnitude approximation. Moreover, these studies are specific to mesenteric venules with flow maintained by a syringe pump. The blood in the vessels has been fully replaced by saline. Nevertheless, the measured time constants provide constraints to possible values for the elasticity and viscosity of this tissue.

Chapter 7

Principle Conclusions and Future Directions

7.1 Principle Conclusions

A significant challenge in using microbubbles in medical ultrasound is the lack of knowledge about how the microbubbles behave in blood vessels when exposed to ultrasound and how their interactions with ultrasound cause vascular bioeffects. The motivation of this thesis work was to provide fundamental understanding to these questions. The specific objectives of this work were to: (1) set up an experimental system for the real-time observations of microbubbles in actual microvessels when insonated; (2) reveal the dynamics of microbubbles in the constrained vascular environment; (3) investigate deformation of the microvessels by the cavitation microbubbles; (4) explore the association of bubble-vessel interaction dynamics and vascular bioeffects; (5) estimate the viscoelastic properties of the microvessels. These specific objectives have been accomplished in the studies presented in Chapters 2–6.

In Chapter 2, a high-speed photomicrography system synchronized with an acoustic system was set up to image microbubbles in microvessels when exposed to ultrasound. Ultra-high speed imaging systems have been used to study ultrasound-activated microbubble dynamics for decades, but most of the studies were performed *in vitro* using tubes or gel phantoms to mimic microvessels. Pioneering work in the observations of microbubble interaction with microvessels was reported by Caskey *et al.*

(Caskey *et al.*, 2007). The major limitation of that work involved the use of strobe imaging, which cannot record microbubble dynamics in real time. Another limitation was that the microvessels were not clearly visible in their recorded images. The main contributions of the work presented in Chapter 2 of this thesis are: (1) an animal tissue model using *ex vivo* rat mesentery was established, whose good optical transparency made it possible to see the microvessels clearly in the recorded images; (2) techniques for administration of microbubbles into the microvessels of the animal tissue model were developed; (3) an apparatus was development to hold the tissue sample for optical imaging and acoustic exposure; and (4) an illumination system was built up to generate enough light throughput so that the images could be captured at a 50-ns exposure time.

In Chapter 3, the microbubble dynamics in the microvessels of the *ex vivo* rat mesentery insonated by single ultrasound pulses were recorded using the ultra-high speed photomicrography system. Previous work proposed that ultrasound-activated microbubbles would translate and produce fluid jets, both being directed toward the vessel wall, and that the impact of the microjets on the vessel wall could lead to enhanced vascular permeability and/or vascular damage. However, the high-speed image sequences obtained during the conduct of the present studies showed microbubble translation and jetting in the direction away from the nearest vessel wall. The main contributions of the work presented in Chapter 3 are: (1) for the first time, the formation of liquid jets in microvessels was clearly recorded, which confirmed that microjets could be formed in the constrained vascular environment; and (2) the microbubble translation and jetting was found in the direction away from the nearest vessel wall, which challenges the conventional wisdom that the jets would direct toward the tissue.

In Chapter 4, microvessel deformation induced by the ultrasound-activated microbubbles was revealed. The recorded images revealed that when microbubbles collapse, the inward fluid flow pulled the surrounding vessel wall inward, causing vessel invagination; the extent of vessel invagination exceeded the corresponding distention in most cases involving arterioles and venules. The corresponding strains associated with invagination also appear to be much higher. The main contributions of the work presented in Chapter 4 are: (1) the vessel dynamics under various pressure amplitudes, vessel sizes, and stand-off distances between the microbubble and the vessel wall were revealed for the first time; (2) a microbubble-induced vessel response in acoustic field, vessel invagination, was newly discovered; and (3) vessel invagination was found can be the dominate vessel response to cavitation microbubbles.

In Chapter 5, an association between the observed vessel deformation and vascular bioeffects was found. The interactions of microbubbles with microvessels were observed using high-speed photomicrography, and the resulting vascular bioeffects was examined by either histology or TEM analyses or indicated directly by the extravasation of the microbubbles. It was found that endothelial cell damage was associated with the invagination-dominated vessel deformation in relative large microvessels. Vessel rupture was observed in capillaries or at high pressure levels, when significant vessel distention followed by invagination was observed. The main contributions of the work presented in

Chapter 5 are: (1) an image registration method was developed to precisely locate the targeted microvessels in histology and TEM studies; (2) the correlation of the recorded dynamics of bubble-vessel interactions and potential vascular bioeffects was found; and (3) while the current paradigm proposes that microbubbles damage vessels by distending them, vessel invagination may be an important and newly-discovered mechanism for the vascular damage, and may even be the dominant mechanism for the damage of relative large microvessels.

In Chapter 6, a microbubble-based method was devised to estimate the viscoelastic properties of the microvessels in the *ex vivo* rat mesentery. In the study presented in Chapter 4, it was found that microbubbles excited by short ultrasound pulses can induce sudden invagination of the adjacent vessel, which remained invaginated even when the microbubbles and the ultrasound field were absent. Inspired by these findings, the relaxation time courses of the deformed microvessels were recorded and analyzed in terms of a Voigt model, consisting of a spring connected in parallel with a dashpot. The relaxation time constant, defined by the ratio of elasticity to viscosity of the microvessels with surrounding tissue, was estimated to be on a time scale of microseconds. The main contributions of the work presented in Chapter 6 are: (1) a novel technique for estimating microvessel viscoelastic properties was introduced; (2) the data obtained from this study added to a base set of biomechanical data on microvessels in the rat mesentery and provided a reference state for comparison to other tissues; and (3) the information about the mechanical properties of the microvessels provides important input to modeling studies attempting to simulate the interactions of microbubbles and microvessels.

7.2 Future Directions

The optical imaging system and the animal preparation methods will be useful for the continuing development of techniques for direct optical observations of microbubble dynamics in microvessels. The new findings introduced in this thesis may motivate researchers to consider the dynamics of the microbubbles and the microvessels when designing techniques for the applications of microbubbles. The experimental results may also provide references to modelers for developing better models to simulate the behavior of microbubbles in the vascular environment. Several future directions are discussed as follows.

7.2.1 Optimization of the Ultra-high Speed Imaging System

The ultra-high speed imaging system set up in this study is a powerful tool for direct observations of microbubble dynamics in actual microvessels. In the future, it could be optimized for yielding better results. For example, in the present setup, the ultrasound transducer is located at the vertical direction, directly above the microscope objective. With the transducer at this direction, the alignment of the transducer, the objective, the optical fiber for illumination and the tissue sample is relative easy to perform. However, one major limitation is that the ultrasound pulses sent out from the transducer are reflected by the objective top surface, reaching the region of interest on the tissue again.

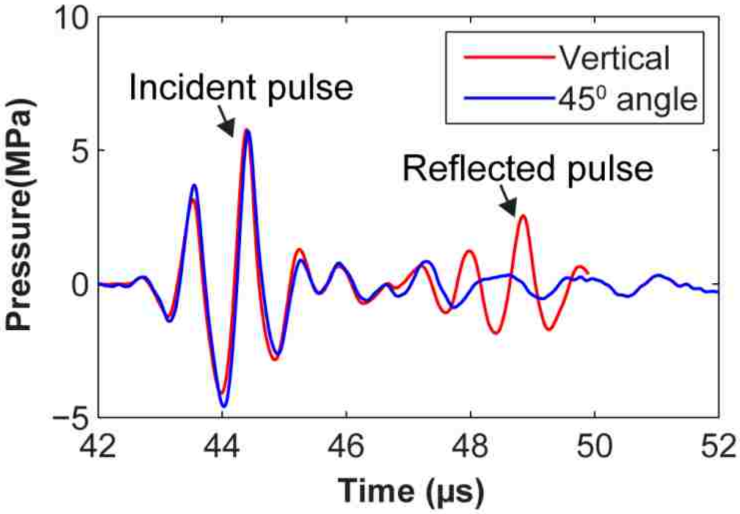

Figure 7.1 Comparison of pressure waveform measured at the location of the tissue sample (the tissue was removed) with the transducer located at the vertical direction (red) or a 45 degree angle (blue). When the transducer was at 45 degree angle, the reflected pulse is absent in the recorded waveform. Their difference in the incident pulse is within the measurement uncertainty.

To get rid of the reflected pulses, one method is to change the transducer from vertical direction to a 45 degree angle. A preliminary study has proved that by changing the angle of the transducer the reflected pulses can be directed away from the region of interest on the tissue, as demonstrated by Figure 7.1. Techniques need to be developed in the future to precisely align the system with the transducer at an angle.

One main challenge in setting up the optical system is that due to the small depth of field of the 40× objective (see Table 7.1), any small movements of the tissue can lead to the recorded images out of the imaging plane. The depth of field of an objective can be estimated using

$$d = \frac{\lambda_0 n}{NA^2} + \frac{n}{M \times NA} e \qquad 7.1$$

where d represents the depth of field, λ is the wavelength of illuminating light, n is the refractive index of the medium between the sample and the objective front lens element, and NA equals the objective numerical aperture. The variable e is the smallest distance that can be resolved by a detector that is placed in the image plane of the microscope objective, whose lateral magnification is M. Therefore, to increase the depth of field, we can use an objective with a lower magnification, as an objective with a lower magnification normally has a lower NA (see Table 7.1). Another benefit of using a lower magnification objective is that the size of the field of view increases, so lower light intensity is needed for high-speed imaging at the same shutter speed. But the tradeoff is that the resolution will decrease. In the present setup, a 40× objective was used to prioritize image resolution. Note that the pixel resolution of the camera was determined to be 6.3 pixels/µm for the 40× objective (see section 2.3.4), corresponding to about 150 nm/pixel, which is above the diffraction limit of the 40× objective. Therefore, the system resolution is limited by the objective. To balance the depth of field, size of the field of view, and the resolution, it is worth to try a 20× objective in the future.

Table 7.1 Parameters of microscope objectives

Magnification	Numerical aperture	Working distance (μm)	Resolving power (μm)	Depth of focus (μm)
10×	0.3	2.00	0.92	3.06
20×	0.5	2.00	0.55	1.10
40×	0.8	2.00	0.34	0.43

7.2.2 Estimation of Vessel Wall and Surrounding Tissue Displacements

The microbubble oscillation could induce the displacements of the vessel wall and the surrounding tissue. Collaborating with Dr. John C. Kucewicz in our lab, some preliminary studies have been performed to estimate bubble-induced displacements of the tissue using a standard two-dimensional cross-correlation method. With this technique, an image frame is divided into small, overlapping sub-regions. The cross-correlation function is evaluated between each sub-region, measuring approximately 10 μm × 10 μm, of the current and previous images to locate a region of corresponding size in the current image that is maximally correlated with the sub-region in the previous image. The location of the current sub-region relative to the location of the previous sub-region is used as an estimate of the local displacement. The cross-correlation function around the local maxima is fit to a second-order surface to achieve sub-pixel displacement resolution. The upper panel of Figure 7.2a are 3 frames selected from a high-speed image sequence. From frame 1 to 2, three bubbles expanded and the vessel wall was distended. The associated relative radial displacement of the surrounding tissue is shown in Figure 7.2b. Displacements are

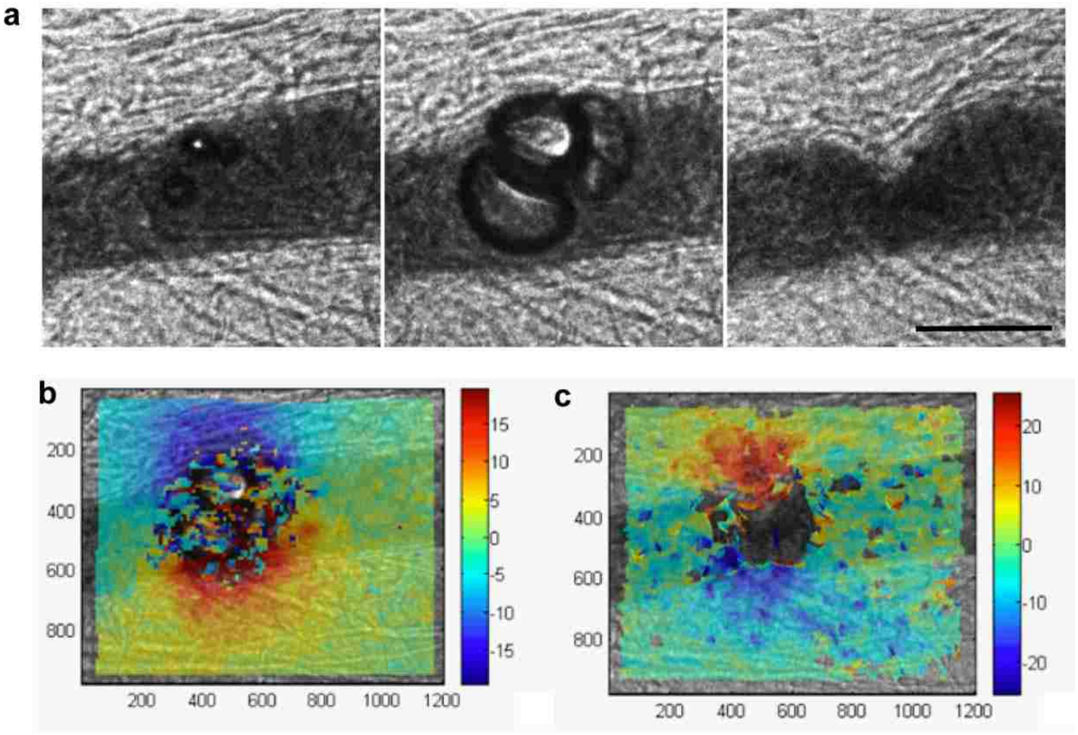

Figure 7.2 (a) Three frames selected from a representative image sequence. (b) Tissue motion associated with the distention of the vessel in the 2nd frame. Blue and red correspond to displacement away from the microbubbles. (b) Tissue motion associated with the invagination of the vessel in the 3rd frame. Blue and red correspond to displacements toward the microbubbles. Displacements are given in pixels.

overlayed on the high-speed image. The blue and red color regions around the bubbles indicate that the tissue moves away from the bubbles (which themselves could not be analyzed). Frame 3 in Figure 7.2a shows that the expanded bubbles collapsed and vessel was invaginated. The relative displacement of the surrounding tissue from frame 1 to 3 is shown in Figure 7.2c. The blue and red colors indicate that the surrounding tissue is displaced toward the bubble. The maximum displacement of the surrounding tissue is about 3.2 μm. The zone of influence of a bubble can be quantified. In this case it is about 40 μm.

One challenge in estimating tissue displacements is that the microbubble oscillation can cause tissue motion out of the image plane. To solve this problem, the depth of field of the microscope objective can be increased by using a lower magnification objective, as discussed in Section 7.2.1.

Beside the challenge due to tissue motion, another challenge is that as there are limited numbers of recorded image frames, the tissue displacements can be too large to be detected by the cross-correlation method. To solve this problem, we can use ultrasound pulses with lower pressure levels to generate smaller tissue movements, or reduce the inter-frame time to increase the similarity between sequential frames.

7.2.3 Ultra-high Speed Imaging of Targeted Microbubbles

In Chapter 3, it was found that a compliant vessel may weaken the adhesion of targeted microbubbles to the vessel walls during insonation. For targeted microbubbles, the close proximity of the microbubbles and the vessel walls lead to potential interactions between them, which may in turn dislodge the targeted microbubbles, limiting their potential usefulness in molecular imaging. One interesting future direction is to assess the microbubble adherence strength, defined by the minimum force needed to dislodge an adherent microbubble.

Some preliminary studies have demonstrated the feasibility of this study. Commercial targeted microbubbles were injected into the prepared animal tissue model, and time was allowed for the microbubbles to attach to the vessel walls. Figure 7.3a and Figure 7.3b show selected frames from two high-speed image sequences that recorded the oscillation of adherent microbubbles exposed to the same ~2 μs ultrasound pulses used in the previous studies with PNP = 0.8 and 1.5 MPa, respectively. Asymmetric oscillations of the microbubbles were observed in both cases. After insonation by the ultrasound pulse with PNP = 0.8 MPa, the microbubble remained adherent to the vessel wall (Figure 7.3a); however, at PNP = 1.5 MPa, the microbubble detached from the vessel wall, accompanied by the deformation of the nearest vessel wall (Figure 7.3b). These preliminary data suggested that the pressure threshold for dislodging adherent targeted microbubbles in the microvessels is between 0.8 and 1.5 MPa. To quantify the adherence strength, the experiment results need to be analyzed in combination with a theoretical analysis of the forces acting on the microbubbles during insonation.

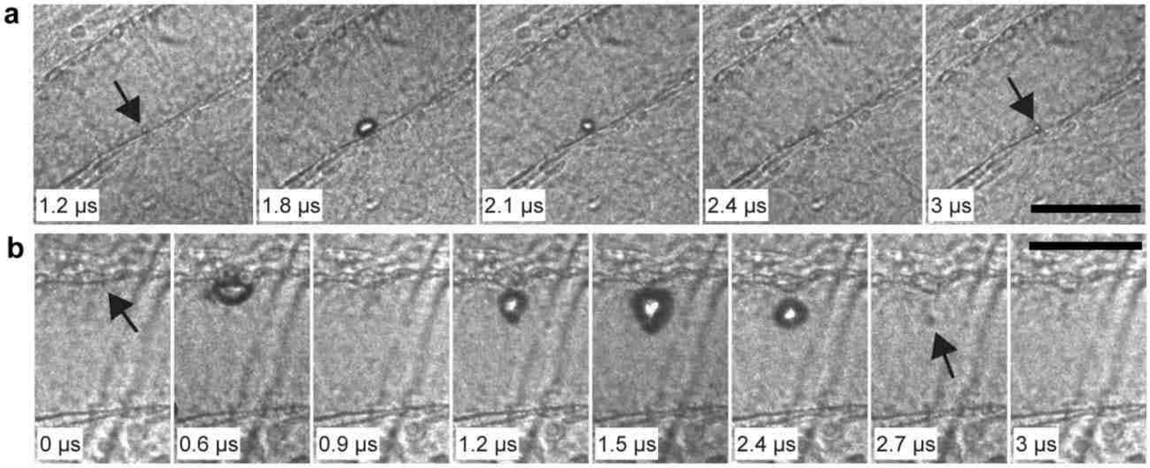

Figure 7.3 Dynamics of adherent microbubbles in microvessels. (a) PNP = 0.8 MPa. The vessel diameter = 50 μm. (b) PNP = 1.5 MPa. The vessel diameter = 58 μm. The arrows point to the targeted microbubbles. The scale bars represent 50 μm.

7.2.4 Ultra-high Speed Imaging of Microbubbles in a Shockwave Field

Acute injury to the kidney occurs in the clinical application of shock wave lithotripsy (SWL). The primary feature of SWL-induced tissue injury is the rupture of blood vessels, with small vessels particularly susceptible to injury (Evan *et al.*, 1998). Cavitation is thought to play a prominent role in SWL induced vascular rupture (Evan *et al.*, 2002). To provide insight into the mechanism of vascular rupture, the interaction of cavitation bubbles with blood vessels, under the excitation of shockwaves, can be directly observed using the ultra-high speed imaging techniques described in Chapter 2. Ultrasound contrast agent microbubbles can be used as cavitation nuclei.

In a preliminary study, an electromagnetic shockwave source (Storz Duolith) was coupled into the system. The pressure waveform measured at the focus of the shockwave generator using the FOPH is shown in Figure 7.4. We can see that different from the ultrasound pulse, the shockwave pulse has a short, high-amplitude positive pressure, followed by a long negative tail. It is this negative tail that can lead to large expansion of bubbles. Figure 7.5 shows two frames selected from a high-speed image sequence recording the cavitation dynamics in a 60 μm vessel insonated by a shockwave pulse with PNP = 7 MPa. The first frame captured the microbubble at the recorded maximum expansion. The lengths of the bubble in the axial and radial directions are about 80 and 60 μm, respectively. This large expansion led to the distention of the nearest vessel wall. The large bubble expansion was followed by rapid bubble collapse, causing vessel invagination. Rupture of the vessel wall was observed as indicated by the extravasation of a bubble fragment, as shown in the second frame. The observed bubble-vessel interaction dynamics are similar to what was found with ultrasound pulses. In the future, more studies are needed to look at their interactions in more detail to find out the mechanisms for vascular damage in shockwave fields.

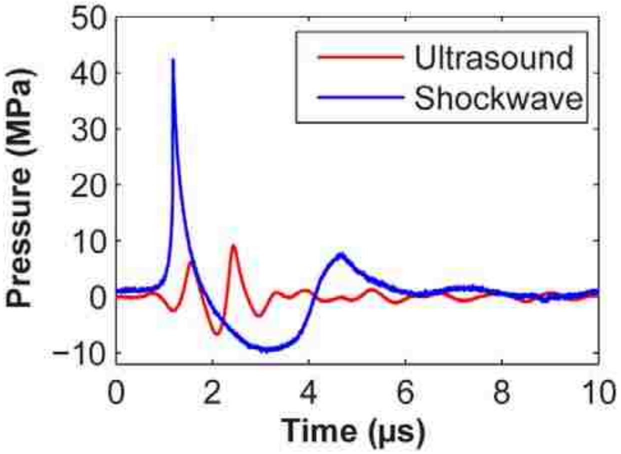

Figure 7.4 Comparison of pressure waveform measured at the focus of an ultrasound transducer or a shockwave generator.

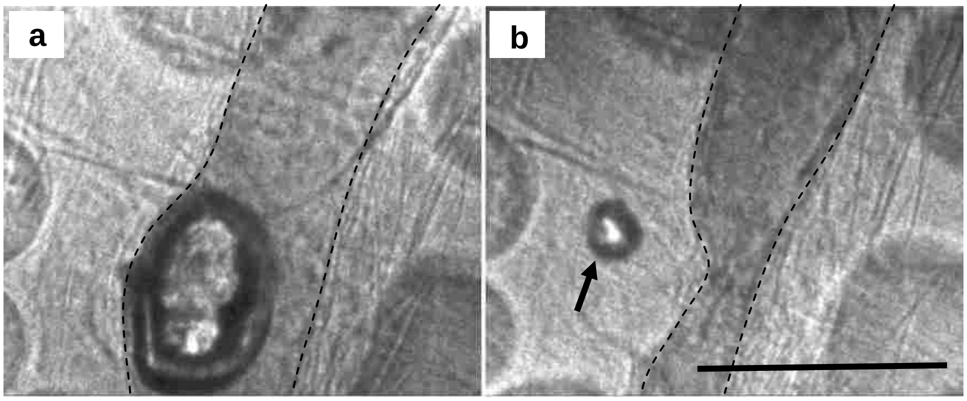

Figure 7.5 Representative frames to show cavitation bubble dynamics in a 60 μm microvessel under the insonation of a shockwave pulse with PNP of 7 MPa. (a) Bubble expansion caused obvious distention of the left side vessel wall. (b) Bubble collapse caused obvious invagination of the left side vessel wall with bubble fragment extravasation from the vessel (arrow). The dash lines highlight the locations of the vessel walls. The scale bar represents 50 μm.

7.2.5 Ultra-high Speed Imaging of Microbubbles *in vivo*

While the *ex vivo* rat mesenteries were demonstrated to work well in this thesis work, future work can be done to use *in vivo* rat mesenteries to overcome the limitations existing in the *ex vivo* model (see Section 2.5) and also to assessment whether the *ex vivo* tissue observations are reproducible in a living model. A major challenge to the *in vivo* experiments involves vascular access that will not occlude the flow of blood into the mesentery while permitting the introduction of microbubbles. To solve this problem, a method allowing localized perfusion of the microbubbles can be used. As illustrated by Figure 7.6, a flexible tube can be inserted into a side branch of the mesenteric artery by a retrograde approach and secured by a suture. Microbubbles can then be injected through this cannula into the mesenteric artery and perfuse to the region of interest. Compared with systemic perfusion, this method may allow better control of where the perfused microbubbles are delivered in the tissue.

In an *in vivo* study, in the hypothetical case in which RBCs were not involved in the bubble-vessel interactions, one would expect that the microbubbles and microvessels would behave in a fashion similar to that observed in the *ex vivo* situation. However, *in vivo*, the microbubbles can be in close proximity to the RBCs, as demonstrated by Figure 7.7. The RBCs near the microbubbles may change the dynamics of the bubble-vessel interactions.

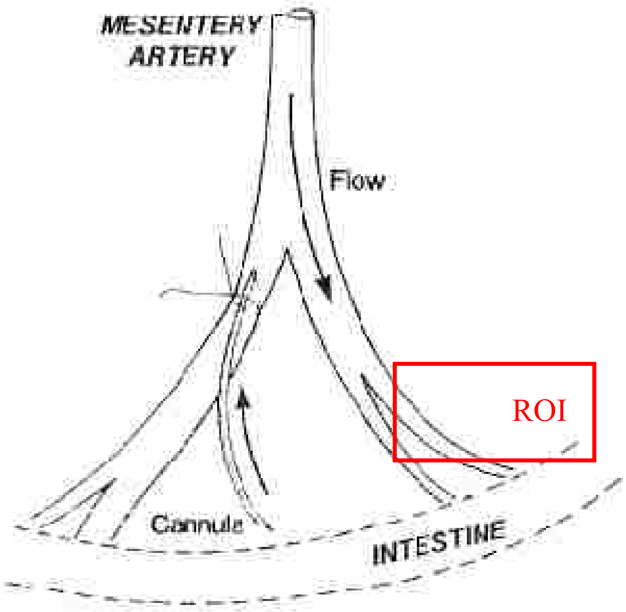

Figure 7.6 Mesentery artery cannulation for the injection of microbubbles to a region of interest (ROI). The arrow indicates the direction of the flow. The region of interest is marked by the rectangle shape. This illustration was modified based on (Feinstein *et al.*, 1984).

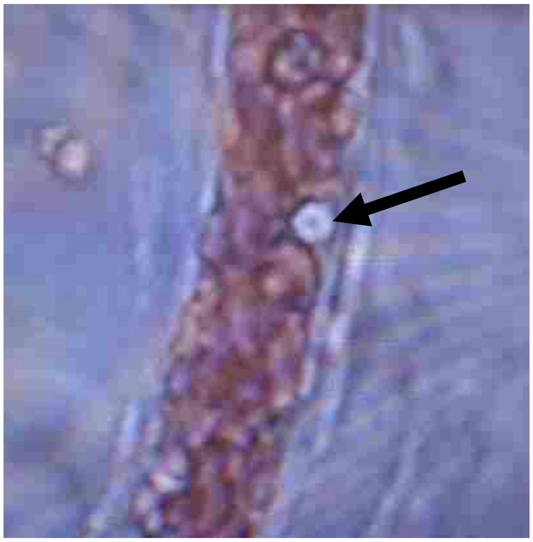

Figure 7.7 Image of a microbubble in a microvessel *in vivo*. The microbubble (white color sphere pointed out by the arrow) was surrounded by RBCs.

7.2.6 Modeling of Microbubble Interaction with Microvessels

The experimental results presented in this thesis have attracted the attention of several groups working on the modeling of the microbubble dynamics in blood vessels. Our collaborators, Dr. Mark Hamilton's group in the University of Texas at Austin, have developed a model for a pulsating microbubble positioned in a viscous, compressible liquid between parallel viscoelastic plates of finite thickness. In addition to the dynamics of the microbubble, they also model the motion of the tissue interface by numerically integrating an equation for the liquid velocity at the liquid tissue interface. Preliminary results from their group have shown qualitative agreement between the model and my experimental results, as demonstrated by Figure 7.8. After being excited by a 1 cycle sinusoidal pressure pulse, the microbubble translates away from the nearest vessel wall while forming a jet in the direction of translation. The simulation results agree with the experimental results in that: (1) invagination exceeds distention; (2) microbubble translates away from the nearest vessel wall; and (3) microjet is formed and directed away from the nearest vessel wall. The model will be improved in the future to generate quantitative agreement with the experimental results.

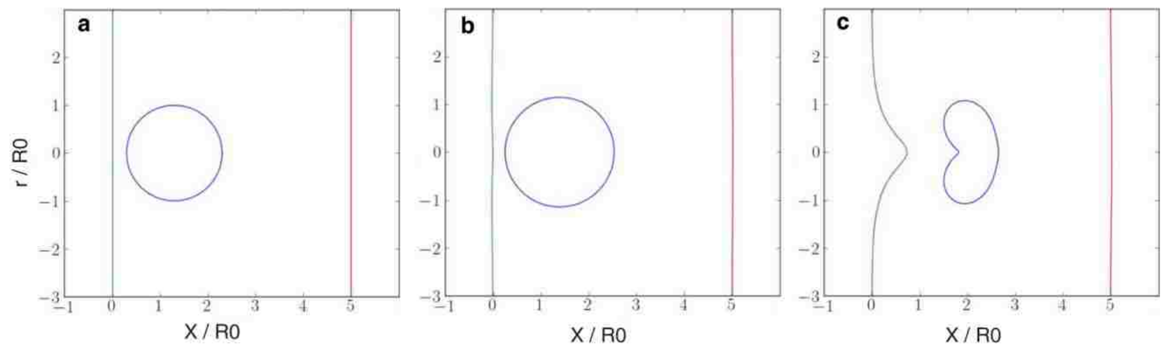

Figure 7.8 Simulated results of a 2 µm diameter gas bubble positioned between two 1 mm thick plates separated by 10 µm. The bubble was excited by a 0.08 MPa, 1 cycle sinusoidal pressure pulse. The green and red lines represent the surfaces of the plates nearest to the bubble. (a) Initial state. (b) Bubble expansion phase. There is no obvious vessel distention. (b) Bubble collapse phase. Significant vessel invagination is accompanied by bubble translation and jetting away from the nearest plate.

BIBLIOGRAPHY

Aggeli, C., Giannopoulos, G., Lampropoulos, K., Pitsavos, C., & Stefanadis, C. (2009). Adverse bioeffects of ultrasound contrast agents used in echocardiography: true safety issue or "much ado about nothing"? *Current Vascular Pharmacology, 7*(3), 338-346.

AIUM. (2000). Section 4--bioeffects in tissues with gas bodies. *Journal of Ultrasound in Medicine, 19*(2), 97-108, 154-168.

Allen, J. S., May, D. J., & Ferrara, K. W. (2002). Dynamics of therapeutic ultrasound contrast agents. *Ultrasound in Medicine and Biology, 28*(6), 805-816.

Ay, T., Havaux, X., Van Camp, G., Campanelli, B., Gisellu, G., Pasquet, A., Denef, J. F., Melin, J. A., & Vanoverschelde, J. L. (2001). Destruction of contrast microbubbles by ultrasound: effects on myocardial function, coronary perfusion pressure, and microvascular integrity. *Circulation, 104*(4), 461-466.

Benjamin, T. B., & Ellis, A. T. (1966). The collapse of cavitation bubbles and the pressures thereby produced against solid boundaries. *Philosophical Transactions of the Royal Society of London. Series A, Mathematical and Physical Sciences, 260*(1110), 221-240.

Blake, J. R., & Gibson, D. C. (1987). Cavitation bubbles near boundaries. *Annual Review of Fluid Mechanics, 19*, 99-123.

Bouakaz, A., Versluis, M., & de Jong, N. (2005). High-speed optical observations of contrast agent destruction. *Ultrasound in Medicine & Biology, 31*(3), 391-399.

Brujan, E. A., Nahen, K., Schmidt, P., & Vogel, A. (2001a). Dynamics of laser-induced cavitation bubbles near an elastic boundary. *Journal of Fluid Mechanics, 433*, 251-281.

Brujan, E. A., Nahen, K., Schmidt, P., & Vogel, A. (2001b). Dynamics of laser-induced cavitation bubbles near elastic boundaries: influence of the elastic modulus. *Journal of Fluid Mechanics, 433*, 283-314.

Calliada, F., Campani, R., Bottinelli, O., Bozzini, A., & Sommaruga, M. G. (1998). Ultrasound contrast agents - Basic principles. *European Journal of Radiology, 27*, S157-S160.

Caro, C. G., Pedley, T. J., Schroter, R. C., Seed, W. A., & Parker, K. H. (1978). *The Mechanics of the Circulation* Oxford University Press.

Carson, A. R., McTiernan, C. F., Lavery, L., Hodnick, A., Grata, M., Leng, X., Wang, J., Chen, X., Modzelewski, R. A., & Villanueva, F. S. (2011). Gene therapy of carcinoma using ultrasound-targeted microbubble destruction. *Ultrasound in Medicine & Biology, 37*(3), 393-402.

Caskey, C. F., Kruse, D. E., Dayton, P. A., Kitano, T. K., & Ferrara, K. W. (2006). Microbubble oscillation in tubes with diameters of 12, 25, and 195 microns. *Applied Physics Letters, 88*(3), 033902.

Caskey, C. F., Qin, S., Dayton, P. A., & Ferrara, K. W. (2009). Microbubble tunneling in gel phantoms. *Journal of the Acoustical Society of America, 125*(5), EL183-189.

Caskey, C. F., Qin, S., & Ferrara, K. W. (2009). Ultrasound mediated drug delivery: The effect of microbubbles on a gel boundary. *Conference Proceeding of the IEEE Engineering in Medicine and Biology Society, 1*, 134-136.

Caskey, C. F., Stieger, S. M., Qin, S., Dayton, P. A., & Ferrara, K. W. (2007). Direct observations of ultrasound microbubble contrast agent interaction with the microvessel wall. *Journal of the Acoustical Society of America, 122*, 1191-1200.

Chahine, G. L. (1977). Interaction between an oscillating bubble and a free-surface. *Journal of Fluids Engineering-Transactions of the ASME, 99*(4), 709-716.

Chin, C. T., Lancee, C., Borsboom, J., Mastik, F., Frijlink, M. E., de Jong, N., Versluis, M., & Lohse, D. (2003). Brandaris 128: A digital 25 million frames per second camera with 128 highly sensitive frames. *Review of Scientific Instruments, 74*(12), 5026-5034.

Chomas, J. E., Dayton, P. A., May, D., Allen, J., Klibanov, A., & Ferrara, K. (2000). Optical observation of contrast agent destruction. *Applied Physics Letters, 77*(7), 1056-1058.

Church, C. C. (1995). The effects of an elastic solid surface layer on the radial pulsations of gas bubbles. *Journal of the Acoustical Society of America, 97*(3), 1510-1521.

Cosgrove, D., & Harvey, C. (2009). Clinical uses of microbubbles in diagnosis and treatment. *Medical and Biological Engineering and Computing, 47*(8), 813-826.

Crouse, L. J., Cheirif, J., Hanly, D. E., Kisslo, J. A., Labovitz, A. J., Raichlen, J. S., Schutz, R. W., Shah, P. M., & Smith, M. D. (1993). Opacification and border delineation improvement in patients with suboptimal endocardial border definition in routine echocardiography: results of the phase-III Albunex multicenter Trial. *Journal of the American College of Cardiology, 22*(5), 1494-1500.

Crum, L. A. (1982, Oct. 27-29). *Acoustic Cavitation.* Paper presented at the Ultrasonics Symposium, San Diego, USA.

Cui, J. Y., Hamilton, M. F., Wilson, P. S., & Zabolotskaya, E. A. (2006). Bubble pulsations between parallel plates. *Journal of the Acoustical Society of America, 119*(4), 2067-2072.

Dayton, P. A., Klibanov, A. L., Brandenburger, G., & Ferrara, K. W. (1999). Acoustic radiation force in vivo: a mechanism to assist targeting of microbubbles. *Ultrasound in Medicine and Biology, 25*(8), 1195-1201.

Dayton, P. A., & Rychak, J. J. (2007). Molecular ultrasound imaging using microbubble contrast agents. *Frontiers in Bioscience, 12*, 5124-5142.

de Jong, N., Cornet, R., & Lancée, C. T. (1994). Higher harmonics of vibrating gas-filled microspheres. Part one: simulations. *Ultrasonics, 32*(6), 447-453.

de Jong, N., Frinking, P. J. A., Bouakaz, A., Goorden, M., Schourmans, T., Xu, J. P., & Mastik, F. (2000). Optical imaging of contrast agent microbubbles in an ultrasound field with a 100-MHz camera. *Ultrasound in Medicine & Biology, 26*(3), 487-492.

Delacrétaz, G., Walsh, J. T., & Asshauer, T. (1997). Dynamic polariscopic imaging of laser-induced strain in a tissue phantom. *Applied Physics Letters, 70*(26), 3510-3512.

Dindyal, S., & Kyriakides, C. (2011). Ultrasound microbubble contrast and current clinical applications. *Recent Patents on Cardiovascular Drug Discovery, 6*(1), 27-41.

Doinikov, A., & Bouakaz, A. (2011). Review of shell models for contrast agent microbubbles. *IEEE Transactions on Ultrasonics Ferroelectrics and Frequency Control 58*(5), 981-993.

Evan, A. P., Willis, L. R., Lingeman, J. E., & McAteer, J. A. (1998). Renal trauma and the risk of long-term complications in shock wave lithotripsy. *Nephron, 78*(1), 1-8.

Evan, A. P., Willis, L. R., McAteer, J. A., Bailey, M. R., Connors, B. A., Shao, Y., Lingeman, J. E., Williams, J. R. J. C., Fineberg, N. S., & Crum, L. A. (2002). Kidney Damage and Renal Functional Changes are Minimized by Waveform

Control that Suppresses Cavitation in Shock Wave Lithotripsy. *Journal of Urology, 168*, 1556-1562.

Evan, C. U., Evan, H., Mani, V., Terry, O. M., & Thomas, M. (2001). Local drug and gene delivery through microbubbles. *Progress in Cardiovascular Diseases, 44*(1), 45-54.

Feinstein, S. B., Cheirif, J., Tencate, F. J., Silverman, P. R., Heidenreich, P. A., Dick, C., Desir, R. M., Armstrong, W. F., Quinones, M. A., & Shah, P. M. (1990). Safety and efficacy of a new transpulmonary ultrasound contrast agent: initial multicenter clinical results. *Journal of the American College of Cardiology, 16*(2), 316-324.

Feinstein, S. B., Shah, P. M., Bing, R. J., Meerbaum, S., Corday, E., Chang, B. L., Santillan, G., & Fujibayashi, Y. (1984). Microbubble dynamics visualized in the intact capillary circulation. *Journal of the American College of Cardiology, 4*(3), 595-600.

Ferrara, K., Pollard, R., & Borden, M. (2007). Ultrasound microbubble contrast agents: Fundamentals and application to gene and drug delivery. *Annual Review of Biomedical Engineering, 9*, 415-447.

Ferrara, K. W. (2008). Driving delivery vehicles with ultrasound. *Advanced Drug Delivery Reviews, 60*(10), 1097-1102.

Fong, S. W., Klaseboer, E., Turangan, C. K., Khoo, B. C., & Hung, K. C. (2006). Numerical analysis of a gas bubble near bio-materials in an ultrasound field. *Ultrasound in Medicine & Biology, 32*(6), 925-942.

Freund, J. B. (2008). Suppression of shocked-bubble expansion due to tissue confinement with application to shock-wave lithotripsy. *Journal of the Acoustical Society of America, 123*(5), 2867-2874.

Fung, Y. C. (1993). *Biomechanics: Mechanical Properties of Living Tissues*. New York: Springer.

Gaehtgen, P., & Uekerman, U. (1971). Distensibility of mesenteric menous microvessels. *Pflugers Archiv-European Journal of Physiology, 330*(3), 206-216.

Gao, F. R., Xiong, C. H., & Xiong, Y. L. (2009). Constrained oscillation of a bubble subjected to shock wave in microvessel. *Progress in Natural Science, 19*(9), 1109-1117.

Garbin, V., Cojoc, D., Ferrari, E., Di Fabrizio, E., Overvelde, M. L. J., van der Meer, S. M., de Jong, N., Lohse, D., & Versluis, M. (2007). Changes in microbubble dynamics near a boundary revealed by combined optical micromanipulation and high-speed imaging. *Applied Physics Letters, 90*(11), 114103.

Gessner, R., & Dayton, P. A. (2010). Advances in molecular imaging with ultrasound. *Molecular Imaging, 9*(3), 117-127.

Gibson, D. C., & Blake, J. R. (1982). The growth and collapse of bubbles near deformable surfaces. *Applied Scientific Research, 38*(1), 215-224.

Girnyk, S., Barannik, A., Barannik, E., Tovstiak, V., Marusenko, A., & Volokhov, V. (2006). The estimation of elasticity and viscosity of soft tissues in vitro using the data of remote acoustic palpation. *Ultrasound in Medicine & Biology, 32*(2), 211-219.

Goldberg, B. B., Liu, J.-B., & Forsberg, F. (1994). Ultrasound contrast agents: A review. *Ultrasound in Medicine & Biology, 20*(4), 319-333.

Gramiak, R., & Shah, P. M. (1968). Echocardiography of the aortic root. *Investigative Radiology, 3*(5), 356-366.

Hernot, S., & Klibanov, A. L. (2008). Microbubbles in ultrasound-triggered drug and gene delivery. *Advanced Drug Delivery Reviews, 60*(10), 1153-1166.

Hu, Y. T., Qin, S. P., Hu, T., Ferrara, K. W., & Jiang, Q. (2005). Asymmetric oscillation of cavitation bubbles in a microvessel and its implications upon mechanisms of clinical vessel injury in shock-wave lithotripsy. *International Journal of Non-Linear Mechanics, 40*(2-3), 341-350.

Hwang, J. H., Tu, J., Brayman, A. A., Matula, T. J., & Crum, L. A. (2006). Correlation between inertial cavitation dose and endothelial cell damage in vivo. *Ultrasound in Medicine & Biology, 32*(10), 1611-1619.

Hynynen, K., McDannold, N., Martin, H., Jolesz, F. A., & Vykhodtseva, N. (2003). The threshold for brain damage in rabbits induced by bursts of ultrasound in the presence of an ultrasound contrast agent (Optison). *Ultrasound in Medicine & Biology, 29*(3), 473-481.

Johnsen, E., & Colonius, T. (2009). Numerical simulations of non-spherical bubble collapse. *Journal of Fluid Mechanics, 629*, 231-262.

Kaul, S. (2004). Microbubbles and ultrasound: a bird's eye view. *Transactions of the American Clinical and Climatological Association, 115*, 137-148.

Kaul, S. (2008). Myocardial contrast echocardiography: A 25-year retrospective. *Circulation, 118*(3), 291-308.

King, D. A., Malloy, M. J., Roberts, A. C., Haak, A., Yoder, C. C., & O'Brien, W. D., Jr. (2010). Determination of postexcitation thresholds for single ultrasound contrast agent microbubbles using double passive cavitation detection. *Journal of the Acoustical Society of America, 127*(6), 3449-3455.

Klibanov, A. (2007). Ultrasound molecular imaging with targeted microbubble contrast agents. *Journal of Nuclear Cardiology, 14*(6), 876-884.

Kobayashi, N., Yasu, T., Yamada, S., Kudo, N., Kuroki, M., Kawakami, M., Miyatake, K., & Saito, M. (2002). Endothelial cell injury in venule and capillary induced by contrast ultrasonography. *Ultrasound in Medicine & Biology, 28*(7), 949-956.

Kodama, T., & Tomita, Y. (2000). Cavitation bubble behavior and bubble-shock wave interaction near a gelatin surface as a study of in vivo bubble dynamics. *Applied Physics B-Lasers and Optics, 70*, 139-149.

Krehl, P., Engemann, S., Rembe, C., & Hofer, E. P. (1999). High-speed visualization, a powerful diagnostic tool for microactuators - retrospect and prospect. *Microsystem Technologies, 5*(3), 113-132.

Kundu, P. K., & Cohen, I. M. (2002). *Fluid Mechanics*. New York: Academic Press.

Kuribayashi, K., & Natori, M. (1999, October 17-20). *A high-magnification and high-speed system for the observation of microbubbles under ultrasound exposure.* Paper presented at the IEEE Ultrasonics Symposium, Nevada USA.

Lee, J. S. (2000). 1998 distinguished lecture: Biomechanics of the microcirculation, an integrative and therapeutic perspective. *Annals of Biomedical Engineering, 28*(1), 1-13.

Leighton, T. G. (1994). *The Acoustic Bubble*. San Diego: Academic Press.

Madsen, E. L., Sathoff, H. J., & Zagzebski, J. A. (1983). Ultrasonic shear wave properties of soft tissues and tissuelike materials. *The Journal of the Acoustical Society of America, 74*(5), 1346-1355.

Main, M. L., Goldman, J. H., & Grayburn, P. A. (2009). Ultrasound contrast agents: balancing safety versus efficacy. *Expert Opinion on Drug Safety, 8*(1), 49-56.

Marmottant, P., & Hilgenfeldt, S. (2003). Controlled vesicle deformation and lysis by single oscillating bubbles. *Nature, 423*(6936), 153-156.

Marmottant, P., van der Meer, S., Emmer, M., Versluis, M., de Jong, N., Hilgenfeldt, S., & Lohse, D. (2005). A model for large amplitude oscillations of coated bubbles accounting for buckling and rupture. *Journal of the Acoustical Society of America, 118*(6), 3499-3505.

Marmottant, P., Versluis, M., de Jong, N., Hilgenfeldt, S., & Lohse, D. (2006). High-speed imaging of an ultrasound-driven bubble in contact with a wall: “Narcissus” effect and resolved acoustic streaming. *Experiments in Fluids, 41*(2), 147-153.

Miao, H., Gracewski, S. M., & Dalecki, D. (2008). Ultrasonic excitation of a bubble inside a deformable tube: Implications for ultrasonically induced hemorrhage. *Journal of the Acoustical Society of America, 124*(4), 2374-2384.

Miao, H. Y., & Gracewski, S. M. (2008). Coupled FEM and BEM code for simulating acoustically excited bubbles near deformable structures. *Computational Mechanics, 42*(1), 95-106.

Miller, A. P., & Nanda, N. C. (2004). Contrast echocardiography: new agents. *Ultrasound in Medicine & Biology, 30*(4), 425-434.

Miller, D., Li, P., & Armstrong, W. F. (2004). The effect of time and of vasoactive drugs on capillary leakage induced during myocardial contrast echocardiography. *Echocardiography, 21*(2), 125-132.

Miller, D. L. (2007). Overview of experimental studies of biological effects of medical ultrasound caused by gas body activation and inertial cavitation. *Progress in Biophysics and Molecular Biology, 93*(1-3), 314-330.

Miller, D. L., Averkiou, M. A., Brayman, A. A., Everbach, E. C., Holland, C. K., Wible, J. H., & Wu, J. R. (2008). Bioeffects considerations for diagnostic ultrasound contrast agents. *Journal of Ultrasound in Medicine, 27*(4), 611-632.

Miller, D. L., & Gies, R. A. (1998). Gas-body-based contrast agent enhances vascular bioeffects of 1.09 MHz ultrasound on mouse intestine. *Ultrasound in Medicine & Biology, 24*(8), 1201-1208.

Miller, D. L., & Gies, R. A. (1999). Consequences of lithotripter shockwave interaction with gas body contrast agent in mouse intestine. *The Journal of Urology, 162*(2), 606-609.

Miller, D. L., & Quddus, J. (2000). Diagnostic ultrasound activation of contrast agent gas bodies induces capillary rupture in mice. *Proceedings of the National Academy of Sciences of the United States of America, 97*(18), 10179-10184.

Miller, M. W., & Brayman, A. A. (1997). Biological effects of ultrasound. The perceived safety of diagnostic ultrasound within the context of ultrasound biophysics: A personal perspective. *Echocardiography, 14*(6 Pt 1), 615-628.

Morgan, K. E., Allen, J. S., Dayton, P. A., Chomas, J. E., Klibaov, A. L., & Ferrara, K. W. (2000). Experimental and theoretical evaluation of microbubble behavior: effect of transmitted phase and bubble size. *IEEE Transactions on Ultrasonics Ferroelectrics and Frequency Control, 47*(6), 1494-1509.

Mulvana, H., Stride, E., Hajnal, J. V., & Eckersley, R. J. (2010). Temperature dependent behavior of ultrasound contrast agents. *Ultrasound in Medicine & Biology, 36*(6), 925-934.

Oguz, H. N., & Prosperetti, A. (1998). The natural frequency of oscillation of gas bubbles in tubes. *Journal of the Acoustical Society of America, 103*(6), 3301-3308.

Ohl, S. W., Klaseboer, E., & Khoo, B. C. (2009). The dynamics of a non-equilibrium bubble near bio-materials. *Physics in Medicine and Biology, 54*(20), 6313-6336.

Ophir, J., & Parker, K. J. (1989). Contrast agents in diagnostic ultrasound. *Ultrasound in Medicine & Biology, 15*(4), 319-333.

Ory, E., Yuan, H., Prosperetti, A., Popinet, S., & Zaleski, S. (2000). Growth and collapse of a vapor bubble in a narrow tube. *Physics of Fluids, 12*(6), 1268-1277.

Phan-Thien, N., Nasseri, S., & Bilston, L. E. (2000). Oscillatory squeezing flow of a biological material. *Rheologica Acta, 39*(4), 409-417.

Philipp, A., & Lauterborn, W. (1998). Cavitation erosion by single laser-produced bubbles. *Journal of Fluid Mechanics, 361*, 75-116.

Pichon, C., Kaddur, K., Midoux, P., Tranquart, F., & Bouakaz, A. (2008). Recent advances in gene delivery with ultrasound and microbubbles. *Journal of Experimental Nanoscience, 3*(1), 17-40.

Piscaglia, F., Lencioni, R., Sagrini, E., Pina, C. D., Cioni, D., Vidili, G., & Bolondi, L. (2010). Characterization of focal liver lesions with contrast-enhanced ultrasound. *Ultrasound in Medicine & Biology, 36*(4), 531-550.

Platts, D. G., & Fraser, J. F. (2011). Contrast echocardiography in critical care: echoes of the future? A review of the role of microsphere contrast echocardiography. *Critical Care and Resuscitation, 13*(1), 44-55.

Plesset, M. S., & Chapman, R. B. (1971). Collapse of an initially spherical vapour cavity in neighbourhood of a solid boundary. *Journal of Fluid Mechanics, 47*(May31), 283-290.

Postema, M., van Wamel, A., Lancée, C. T., & de Jong, N. (2004). Ultrasound-induced encapsulated microbubble phenomena. *Ultrasound in Medicine & Biology, 30*(6), 827-840.

Prentice, P., Cuschierp, A., Dholakia, K., Prausnitz, M., & Campbell, P. (2005). Membrane disruption by optically controlled microbubble cavitation. *Nature Physics, 1*(2), 107-110.

Pries, A. R., Ley, K., & Gaehtgens, P. (1986). Generalization of the Fahraeus Principle for Microvessel Networks. *American Journal of Physiology, 251*(6), H1324-H1332.

Pysz, M. A., Foygel, K., Panje, C. M., Needles, A., Tian, L., & Willmann, J. K. (2011). Assessment and monitoring tumor vascularity with contrast-enhanced ultrasound maximum intensity persistence imaging. *Investigative Radiology, 46*(3), 187-195.

Pysz, M. A., Gambhir, S. S., & Willmann, J. K. (2010). Molecular imaging: current status and emerging strategies. *Clinical Radiology, 65*(7), 500-516.

Qin, S. P., Caskey, C. F., & Ferrara, K. W. (2009). Ultrasound contrast microbubbles in imaging and therapy: physical principles and engineering. *Physics in Medicine and Biology, 54*(6), R27-R57.

Qin, S. P., & Ferrara, K. W. (2006). Acoustic response of compliable microvessels containing ultrasound contrast agents. *Physics in Medicine and Biology, 51*(20), 5065-5088.

Qin, S. P., Hu, Y. T., & Jiang, Q. (2006). Oscillatory interaction between bubbles and confining microvessels and its implications on clinical vascular injuries of shock-wave lithotripsy. *IEEE Transactions on Ultrasonics Ferroelectrics and Frequency Control, 53*(7), 1322-1329.

Rayleigh, L. (1917). On the pressure developed in a liquid during the collapse of a spherical cavity. *Philosophical Magazine, 34*(199-04), 94-98.

Roberts, F., & Roberts, D. (2011), from http://mathbits.com/mathbits/tisection/statistics2/correlation.htm

Robinson, P. B., Blake, J. R., Kodama, T., Shima, A., & Tomita, Y. (2001). Interaction of cavitation bubbles with a free surface. *Journal of Applied Physics, 89*(12), 8225-8237.

Rota, C., Raeman, C. H., Child, S. Z., & Dalecki, D. (2006). Detection of acoustic cavitation in the heart with microbubble contrast agents in vivo: a mechanism for ultrasound-induced arrhythmias. *Journal of the Acoustical Society of America, 120*(5 Pt 1), 2958-2964.

Sassaroli, E., & Hynynen, K. (2004). Forced linear oscillations of microbubbles in blood capillaries. *Journal of the Acoustical Society of America, 115*(6), 3235-3243.

Sassaroli, E., & Hynynen, K. (2005). Resonance frequency of microbubbles in small blood vessels: a numerical study. *Physics in Medicine and Biology, 50*(22), 5293-5305.

Sassaroli, E., & Hynynen, K. (2006). On the impact of vessel size on the threshold of bubble collapse. *Applied Physics Letters, 89*(12), 123901.

Schmidt, B. J., Sousa, I., van Beek, A. A., & Bohmer, M. R. (2008). Adhesion and ultrasound-induced delivery from monodisperse microbubbles in a parallel plate flow cell. *Journal of Controlled Release, 131*(1), 19-26.

Schneider, A., Johnson, L., Goodwin, M., Schelleman, A., & Bellomo, R. (2011). Bench-to-bedside review: Contrast enhanced ultrasonography - a promising technique to assess renal perfusion in the ICU. *Critical Care, 15*(3), 157.

Schutt, E. G., Klein, D. H., Mattrey, R. M., & Riess, J. G. (2003). Injectable microbubbles as contrast agents for diagnostic ultrasound imaging: the key role of perfluorochemicals. *Angewandte Chemie International Edition, 42*(28), 3218-3235.

Shen, Z. P., Brayman, A. A., Chen, L., & Miao, C. H. (2008). Ultrasound with microbubbles enhances gene expression of plasmid DNA in the liver via intraportal delivery. *Gene Therapy, 15*(16), 1147-1155.

Shima, A., Tomita, Y., Gibson, D. C., & Blake, J. R. (1989). The growth and collapse of cavitation bubbles near composite surfaces. *Journal of Fluid Mechanics, 203*, 199-214.

Shohet, R. V., & Grayburn, P. A. (2006). Potential bioeffects of ultrasonic destruction of microbubble contrast agents. *Journal of the American College of Cardiology, 47*(7), 1469-1470.

Skyba, D. M., Price, R. J., Linka, A. Z., Skalak, T. C., & Kaul, S. (1998). Direct in vivo visualization of intravascular destruction of microbubbles by ultrasound and its local effects on tissue. *Circulation, 98*(4), 290-293.

Soliman, O. I., De Jong, N., Van Der Zwaan, H. B., Galema, T. W., Vletter, W. B., Van Dalen, B. M., Schinkel, A. F., Ten Cate, F. J., & Geleijnse, M. L. (2010). Contrast echocardiography: mechanism of action, safety and clinical applications. *Minerva Cardioangiologica, 58*(3), 343-355.

Stieger, S. M., Caskey, C. F., Adamson, R. H., Qin, S., Curry, F.-R. E., Wisner, E. R., & Ferrara, K. W. (2007). Enhancement of vascular permeability with low-rrequency contrast-enhanced ultrasound in the chorioallantoic membrane model. *Radiology, 243*(1), 112-121.

Stride, E. P., & Coussios, C. C. (2010). Cavitation and contrast: the use of bubbles in ultrasound imaging and therapy. *Proceedings of the Institution of Mechanical Engineers Part H-Journal of Engineering in Medicine, 224*(H2), 171-191.

Swayne, G. T. G., Smaje, L. H., & Bergel, D. H. (1989). Distensibility of single capillaries and venules in the rat and frog mesentery. *International Journal of Microcirculation-Clinical and Experimental, 8*(1), 25-42.

ter Haar, G. (2009). Safety and bio-effects of ultrasound contrast agents. *Medical and Biological Engineering and Computing, 47*(8), 893-900.

Tran, T. A., Le Guennec, J. Y., Babuty, D., Bougnoux, P., Tranquart, F., & Bouakaz, A. (2009). On the mechanisms of ultrasound contrast agents-induced arrhythmias. *Ultrasound in Medicine & Biology, 35*(6), 1050-1056.

Tu, J., Hwang, J. H., Matula, T. J., Brayman, A. A., & Crum, L. A. (2006). Intravascular inertial cavitation activity detection and quantification in vivo with Optison. *Ultrasound in Medicine & Biology, 32*(10), 1601-1609.

Van Camp, G., Droogmans, S., & Cosyns, B. (2007). Bio-effects of ultrasound contrast agents in daily clinical practice: fact or fiction? *European Heart Journal, 28*(10), 1190-1192.

Van Leeuwen, T. G., Meertens, J. H., Velema, E., Post, M. J., & Borst, C. (1993). Intraluminal vapor bubble induced by excimer laser-pulse causes microsecond arterial dilation and invagination leading to extensive wall damage in the rabbit. *Circulation, 87*(4), 1258-1263.

Van Wamel, A., Bouakaz, A., Versluis, M., & De Jong, N. (2004). Micromanipulation of endothelial cells: Ultrasound-microbubble-cell interaction. *Ultrasound in Medicine & Biology, 30*(9), 1255-1258.

Vancraeynest, D., Havaux, X., Pasquet, A., Gerber, B., Beauloye, C., Rafter, P., Bertrand, L., & Vanoverschelde, J. L. (2009). Myocardial injury induced by ultrasound-targeted microbubble destruction: evidence for the contribution of myocardial ischemia. *Ultrasound in Medicine & Biology, 35*(4), 672-679.

Villanueva, F. S., & Wagner, W. R. (2008). Ultrasound molecular imaging of cardiovascular disease. *Nature Clinical Practice Cardiovascular Medicine, 5*, S26-S32.

Voigt, J. U. (2009). Ultrasound molecular imaging. *Methods, 48*(2), 92-97.

Wilbert, D. M. (2002). A comparative review of extracorporeal shock wave generation. *BJU International, 90*(5), 507-511.

Ye, T., & Bull, J. L. (2006). Microbubble expansion in a flexible tube. *Journal of Biomechanical Engineering, 128*(4), 554-563.

Yuan, H., Oguz, H. N., & Prosperetti, A. (1999). Growth and collapse of a vapor bubble in a small tube. *International Journal of Heat and Mass Transfer, 42*(19), 3643-3657.

Zachary, J. F., Blue, J. P., Miller, R. J., & O'Brien, W. D., Jr. (2006). Vascular lesions and s-thrombomodulin concentrations from auricular arteries of rabbits infused with microbubble contrast agent and exposed to pulsed ultrasound. *Ultrasound in Medicine & Biology, 32*(11), 1781-1791.

Zhao, S., Borden, M., Bloch, S. H., Kruse, D., Ferrara, K. W., & Dayton, P. A. (2004). Radiation-force assisted targeting facilitates ultrasonic molecular imaging. *Molecular Imaging, 3*(3), 135-148.

Zhao, S. K., Ferrara, K. W., & Dayton, P. A. (2005). Asymmetric oscillation of adherent targeted ultrasound contrast agents. *Applied Physics Letters, 87*(13), 134103-134103.

Zheng, H. R., Dayton, P. A., Caskey, C., Zhao, S. K., Qin, S. P., & Ferrara, K. W. (2007). Ultrasound-driven microbubble oscillation and translation within small phantom vessels. *Ultrasound in Medicine & Biology, 33*(12), 1978-1987.

Zhong, P., Zhou, Y. F., & Zhu, S. L. (2001). Dynamics of bubble oscillation in constrained media and mechanisms of vessel rupture in SWL. *Ultrasound in Medicine & Biology, 27*, 119-134.

Curriculum Vitae

Hong Chen

Education

2011	Ph.D.	Department of Bioengineering, University of Washington
2006	M.E.	Biomedical Engineering, Xi’an Jiaotong University
2003	B.E.	Biomedical Engineering, Xi’an Jiaotong University

Academic Awards

2011	UW Bioengineering outstanding teaching assistant award
2008	Best student paper award at the 2008 IEEE International Ultrasonics Symposium Beijing, China
2005	The R. W. B. Stephens Prize winner at the World Congress on Ultrasonics / Ultrasonics International (WCU/UI’05)

Journal Publications

H. Chen, W. Kreider, A. A. Brayman, M. R. Bailey, and T. J. Matula, "Blood vessel deformations on microsecond time scales by ultrasonic cavitation," *Phys Rev Lett,* vol. 106, p. 034301, **2011**

H. Chen, A. A. Brayman, M. R. Bailey, and T. J. Matula, "Blood vessel rupture by cavitation," *Urol. Res.,* vol. 38, pp. 321-326, **2010**.

H. Chen, X. J. Li, M. X. Wan, and S. P. Wang, "High-speed observation of cavitation bubble clouds near a tissue boundary in high-intensity focused ultrasound fields," *Ultrasonics,* vol. 49, pp. 289-292, **2009**.

H. Chen, X. Li, M. Wan, and S. Wang, "High-speed observation of cavitation bubble cloud structures in the focal region of a 1.2 MHz high-intensity focused ultrasound transducer," *Ultrason. Sonochem.*, vol. 14, pp. 291-297, **2007**.

H. Chen, X. J. Li, and M. X. Wan, "Spatial-temporal dynamics of cavitation bubble clouds in 1.2 MHz focused ultrasound field," *Ultrason. Sonochem.*, vol. 13, pp. 480-486, **2006**.

H. Chen, X. Li, and M. Wan, "The inception of cavitation bubble clouds induced by high-intensity focused ultrasound," *Ultrasonics*, vol. 44, pp. e427-e429, **2006**.

H. Chen, A. A. Brayman, and T. J. Matula, "Observations of translation and jetting of ultrasound-activated microbubble in mesenteric microvessels," *Ultrasound Med. Biol.* **(Under revision)**

H. Chen, A. A. Brayman, A. P. Evan, and T. J. Matula, "Correlation of ultrasound-activated microbubble induced vessel deformation and vascular bioeffects," *Ultrasound Med. Biol.* **(In preparation)**

H. Chen, A. A. Brayman, and T. J. Matula, "Relaxation of microvessels deformed by ultrasound-activated microbubble," *Appl. Phys. Lett.* **(In preparation)**

Proceeding Publications

H. Chen, A. A. Brayman, A. P. Evan, and T. J. Matula, "Mechanisms for microvascular damage induced by ultrasound-activated microbubbles," in *The International Society for Therapeutic Ultrasound Symposium*, New York, USA, **2011**.

H. Chen, A. A. Brayman, and T. J. Matula, “The peculiar interactions of microbubbles and microvessels,” in *Proceedings of 20th International Congress on Acoustics, ICA 2010*, Sydney, Australia, **2010**.

H. Chen, A. A. Brayman, A. P. Evan, and T. J. Matula, "Vascular damage by ultrasound-activated microbubble induced vessel invagination," in *IEEE Ultrasonics Symposium, IUS* **2010,** pp.678-681

H. Chen, A. A. Brayman, and T. J. Matula, "Imaging targeted microbubble interactions with microvessels," in *IEEE Ultrasonics Symposium, IUS* **2010,** pp. 1117-1120.

H. Chen, J. Kucewicz, W. Kreider, A. A.Brayman, M. R. Bailey, and T. J. Matula, "Observations of bubble-vessel interactions in ultrasound fields," in *IEEE Ultrasonics Symposium, IUS* **2009**, pp. 23-26.

W. Kreider, **C. Hong**, M. R. Bailey, A. A. Brayman, and T. J. Matula, "Potential mechanism for vessel invagination caused by bubble oscillations," in *IEEE Ultrasonics Symposium, IUS* **2009**, pp. 353-356.

H. Chen, A. A. Brayman, and T. J. Matula, "Microbubble dynamics in microvessels: Observations of microvessel dilation, invagination and rupture," in *IEEE Ultrasonics Symposium, IUS* **2008**, pp. 1163-1166.

L. A. Crum, M. R. Bailey, M. S. Canney, **H. Chen**, T. J. Matula, and C. McInnes, "Cinephotographic observations of particle removal from a surface by acoustic cavitation," in *The 155th Meeting of the Acoustical Society of America*, Paris, France, **2008**.

X. Li, **H. Chen**, and M. Wan, "The dynamics of cavitation bubble clouds in high-intensity focused ultrasound field observed by high-speed photography," in *Proc. SPIE* **2007,** p. *627922*.

Conference Abstracts:

H. Chen, C. Perez, A. A. Brayman, and T. J. Matula, "High speed imaging of shockwave-induced dynamics of cavitation bubbles and vessel wall," in *The 161th Meeting of the Acoustical Society of America,* Seattle, Washington, **2011**.

C. Perez, **H. Chen**, and T. J. Matula, " Calibration and characterization of an electromagnetic shockwave medical device, " in *The 161th Meeting of the Acoustical Society of America,* Seattle, Washington, **2011**.

H. Chen, A. A. Brayman, and T. J. Matula, "Visualizing bubble/vessel interactions," in *The Artimino Conference on Medical Ultrasound Technology*, Artimino, Florence, **2011**. **(Invited talk)**

H. Chen, A. A. Brayman, and T. J. Matula, " Correlating microvessel permeability directly with ultrasound-activated microbubble dynamics, " in *The 160th Meeting of the Acoustical Society of America,* Cancun, Mexico, **2010**. **(Invited talk)**

M. F. Hamilton. T.A. Hay, Y. A. Illinskii, E.A. Zabolostkaya, **H. Chen**, W. Kreider, M.R. Bailey, T.J. Matula, " Models for the dynamical interaction of bubbles and blood vessels," in *The 160th Meeting of the Acoustical Society of America,* Cancun, Mexico, **2010**. **(Invited talk)**

H. Chen, A. A. Brayman, Y.Wang, J.Hwang, A.P.Evan, W.Kreider, M.R.Bailey and T. J. Matula, "Correlation between direct observations of cavitation in blood vessels of exvivo tissues and associated vascular damage," in *The International Society for Therapeutic Ultrasound Symposium*, Tokyo, Japan, 2010.

W. Kreider, **H. Chen**, M.R. Bailey, A.A. Brayman, T.J. Matula, " Bubble-boundary interactions relevant to medical ultrasound," in *The 159th Meeting of the Acoustical Society of America,* Baltimore, Maryland, **2010**.

H. Chen, W. Kreider, M. Bailey, A. Brayman, and T. Matula, "Observations of microbubble translation near vessel walls," in *The 159th Meeting of the Acoustical Society of America,* Baltimore, Maryland, **2010**.

H. Chen, W. Kreider, J. C. Kucewicz, M. R. Bailey, A. A. Brayman, and T. J. Matula, "Quantitative measurements of microbubble interactions with surrounding vessels and tissues," in *The 158th Meeting of the Acoustical Society of America,* San Antonio, Texas, **2009**.

H. Chen, A. A. Brayman, M. R. Bailey, and T. J. Matula, "Direct observation of microbubble interactions with ex vivo microvessels " in *The 157th Meeting of the Acoustical Society of America*, Portland, Oregon, **2009**.

H. Chen, X. Li, and M. Wan, "High-speed observation of cavitation bubble clouds near a tissue surface in high-intensity focused ultrasound field," in *The World Congress on Ultrasonics-Ultrasonics International*, Beijing, China, **2005**.